

博士論文（要約）

Gas-phase molecular and cluster anions as microscopic  
model systems for solution chemistry

(溶液化学の微視的モデルとしての気相負イオンの研究)

中西隆造



## List of publications

1. Incorporation of ROH (R = CH<sub>3</sub>, C<sub>2</sub>H<sub>5</sub>, 2-C<sub>3</sub>H<sub>7</sub>) into (H<sub>2</sub>O)<sub>6</sub><sup>-</sup> : Substituent effect on the growth process of the hydrogen-bond network  
**Ryuzo Nakanishi** and Takashi Nagata  
*Journal of Physical Chemistry A* 118 7360-7366 (2014)
2. Hydrogen-bond network transformation in water-cluster anions induced by the complex formation with benzene  
**Ryuzo Nakanishi**, Takeshi Sato, Kiyoshi Yagi, and Takashi Nagata  
*Journal of Physical Chemistry Letters* 3 3571-3575 (2012)
3. Formation and Photodestruction of *dual dipole-bound* anion (H<sub>2</sub>O)<sub>6</sub>{e<sup>-</sup>}CH<sub>3</sub>NO<sub>2</sub>  
**Ryuzo Nakanishi** and Takashi Nagata  
*Journal of Chemical Physics* 130 224309 1-8 (2009)
4. Photoelectron spectroscopy of acetone cluster anions, [(CH<sub>3</sub>)<sub>2</sub>CO]<sub>n</sub><sup>-</sup> (n = 2, 5 – 15)  
**Ryuzo Nakanishi**, Azusa Muraoka, and Takashi Nagata  
*Chemical Physics Letters* 427 56-61 (2006)
5. Photodissociation of gas-phase I<sub>3</sub><sup>-</sup>: Comprehensive understanding of nonadiabatic dissociation dynamics  
**Ryuzo Nakanishi**, Naoya Saitou, Tomoyo Ohono, Satomi Kowashi, Satoshi Yabushita, and Takashi Nagata  
*Journal of Chemical Physics* 126 204311 1-17 (2007)

## Author contributions

The author performed all the experimental work in the listed publications. Quantum chemical studies in papers 1 and 4 were carried out together with co-author, but the author did not take part in the theoretical calculations in papers 2 and 5. All the experimental and theoretical data of each publication were analyzed and interpreted by the author in collaboration with the co-authors.



# Contents

<b>1 Introduction</b>	<b>1</b>
1.1 Background	2
1.1.1 Probing solution ion chemistry in the gas phase	2
1.1.2 Target anionic systems	3
1.2 Thesis overview: summary of systems studied	6
1.2.1 Incorporation reactions of water cluster anions	6
1.2.2 Electron trapping mechanism of acetone clusters	8
1.2.3 Photodissociation dynamics of gas-phase tri-iodide anion	9
References	10
<b>2 Incorporation of ROH (R = CH<sub>3</sub>, C<sub>2</sub>H<sub>5</sub>, 2-C<sub>3</sub>H<sub>7</sub>) into (H<sub>2</sub>O)<sub>6</sub> : Substituent effect on the growth process of the hydrogen-bond network</b>	<b>15</b>
2.1 Introduction	16
2.2 Experimental	17
2.3 Results and discussion	18
2.3.1 ROH uptake measurement	18
2.3.2 Photoelectron spectra	20
2.3.3 Incorporation mechanism	22
2.4 Conclusions	26
References	28
Supplemental material	30
S2.1 Computational details	32
S2.2 References	33
<b>3 Hydrogen-bond network transformation in water-cluster anions induced by the complex formation with benzene</b>	<b>35</b>
3.1 Introduction	36
3.2 Experimental	37
3.3 Results and discussion	37
3.4 Summary	43
References	45
Supplemental material	47
S3.1 Ar-mediated association process	47

S3.2 PES measurement of $\text{Bz}(\text{H}_2\text{O})_6^- \text{Ar}$ .....	49
S3.3 Computational details .....	49
S3.4 Optimized geometries .....	50
S3.5 References .....	54
<b>4 Formation and Photodestruction of dual dipole-bound anion <math>(\text{H}_2\text{O})_6\{e^-\}\text{CH}_3\text{NO}_2</math></b>	<b>55</b>
4.1 Introduction.....	56
4.2 Experimental .....	57
4.3 Results and discussion .....	60
4.3.1 Formation of “dual dipole-bound” anion $(\text{H}_2\text{O})_6\{e^-\}\text{CH}_3\text{NO}_2$ .....	60
4.3.2 Photostimulated conversion of $(\text{H}_2\text{O})_6\{e^-\}\text{NM}$ to valence anion .....	64
4.4 Summary.....	68
References.....	70
<b>5 Photoelectron spectroscopy of acetone cluster anions</b>	
<b><math>[(\text{CH}_3)_2\text{CO}]_n^-</math> (<math>n = 2, 5 - 15</math>)</b>	<b>73</b>
5.1 Introduction.....	74
5.2 Experimental .....	74
5.3 Results and discussion .....	75
5.3.1 Mass spectra .....	75
5.3.2 Photoelectron spectra.....	76
5.3.3 Photoelectron angular distributions .....	78
5.3.4 Structures of $(\text{Acn})_n^-$ .....	81
5.3.5 Qualitative evaluation of $\beta$ values .....	82
References.....	84
<b>6 Photodissociation of gas-phase <math>\text{I}_3^-</math>: Comprehensive understanding of nonadiabatic dissociation dynamics</b>	<b>85</b>
* <i>Only the abstract is provided in UTokyo Repository.</i>	
(博士論文の共著者の意向により第6章はABSTRACT以外除外)	
<b>Acknowledgements</b> .....	<b>87</b>

# **Chapter 1**

## **Introduction**

## 1.1 Background

### 1.1.1 Probing solution ion chemistry in the gas phase

Ions are ubiquitous constituents in nature and are engaged in a wide range of chemical processes. The remarkable aspects of ionic species originate from electrostatic interactions with their surrounding molecules, which generally dominate over interactions between neutral molecules and consequently render ionic species sensitive to external perturbations. In view of the fact that a majority of ionic processes occurs in solutions, where the solvents influence stability, structure, and reactivity of ionic species, detailed understanding of those influences is a critical issue to be addressed for elucidation of the underlying mechanisms in ionic processes

Gas-phase molecular and cluster ions have offered a unique opportunity to gain insights into molecular level picture of ionic processes in solutions. Investigations of bare molecular ions in the gas phase provide information on their intrinsic properties in the absence of the interference from solvents, allowing us to infer solvent effects from comparison with their corresponding properties in the solution phase. Cluster ions are charged aggregates of a limited number of atoms or molecules. Due to their finite many-body nature, cluster ions can be viewed as mesoscopic systems between the molecular and the bulk regimes, and present local environments in electrolyte solutions; one can construct a well-defined chemical system representing an ion of interest and its surroundings, thereby simplifying an ionic system under solvated conditions. In addition, cluster environments mediate a variety of cluster-specific phenomena, such as stabilizing and quenching reaction intermediates that are elusive in a bare state or bulk environments. Since gas-phase experimental techniques described below afford detailed information on structures and dynamics of cluster ions, one can microscopically understand the role of the surrounding molecules in ionic processes.<sup>1-4</sup>

From experimental perspective, the main virtue of gaseous ion studies lies in the combination of mass spectrometry and laser spectroscopy. Once formed in the gas phase, more specifically *in vacuo*, ions of interest can be readily isolated by standard mass spectrometric methods according to the mass to charge ratio, which provide us with the precise control over size and composition for the target ionic systems. The ions thus isolated can be interrogated by various laser spectroscopic techniques. For anionic species, photoelectron spectroscopy has proven to be a powerful tool to probe electronic structures of both the anions and the corresponding neutral species.<sup>5</sup> In particular, photoelectron imaging is the spectroscopic technique for simultaneous measurements of conventional energy-domain spectra and photoelectron angular distributions. The latter provide information on the symmetry of the molecular orbitals from which the photoelectrons originate.<sup>6,7</sup> Photodissociation spectroscopy in the visible and uv regions provides insights into excited states of the ionic species.<sup>8,9</sup> Vibrational spectroscopy with infrared photodissociation is widely used for sensitive probe for



geometric structures.<sup>10,11</sup> Another important advantage in gaseous ion studies is that they are amenable to modern theoretical calculations for fairly large sizes. Thus, abundant information on structures and dynamics can be obtained for a given ionic system from the interplay between experimental and theoretical investigations.

The work in this dissertation encompasses the efforts to probe anionic solution chemistry in the gas phase by exploiting the corresponding molecular and cluster anions with the aim of obtaining microscopic insight into the relevant structures and dynamics. The next section gives an introductory description of the anionic systems dealt with in this dissertation.

### 1.1.2 Target anionic systems

#### *Hydrated electron and water cluster anions*

When an aqueous solution is exposed to ionizing radiation, electrons are released from either solvents or solutes, and then stabilized by the interactions with surrounding water molecules to form the hydrated electron,  $e^-_{\text{aq}}$ . Since the first observation in 1962,<sup>12</sup>  $e^-_{\text{aq}}$  has captured considerable interest as a key intermediate in radiation chemistry<sup>13</sup> and biology<sup>14</sup> in aqueous solutions. At a more fundamental level,  $e^-_{\text{aq}}$  has been referred to as the simplest hydrated ion, presenting an intriguing system for studying electron-water interactions. In spite of a great deal of efforts to understand the structure and reactivity of  $e^-_{\text{aq}}$ , its fleeting nature has posed a challenge to elucidating the microscopic picture of  $e^-_{\text{aq}}$ .

Studies of the water cluster anions,  $(\text{H}_2\text{O})_n^-$ , in the gas phase have offered an alternative approach to understanding electron hydration in detail. The electronic and geometric properties of  $(\text{H}_2\text{O})_n^-$  have been the subject of numerous experimental<sup>15-42</sup> and theoretical<sup>43-48</sup> investigations. Photoelectron spectroscopic studies have revealed that there exist at least three distinct isomeric forms of  $(\text{H}_2\text{O})_n^-$ . They are distinguishable by their differing vertical electron detachment energies (VDEs), and usually labeled as I, II, and III in decreasing order of the respective VDEs.<sup>21-28</sup> Figure 1.1 displays the size-dependent VDEs of  $(\text{H}_2\text{O})_n^-$  plotted against the inverse of the cluster radius, which is approximately represented by  $n^{-1/3}$ .<sup>42</sup> The VDEs for isomer I, the most strongly electron binding species, scales linearly with  $n^{-1/3}$  and gives the extrapolated value of  $\sim 3.3$  eV in the limit of  $n \rightarrow \infty$ , which agrees well with the bulk VDEs of 3.3 – 3.6 eV measured by photoelectron spectroscopy of liquid microjets of the aqueous solutions.<sup>49-52</sup> Therefore, isomer I has been thought to be a legitimate candidate for the microscopic precursors of the bulk  $e^-_{\text{aq}}$ . As for isomers II and III, they have been attributed to metastable species formed via electron attachment to cold neutral water clusters. It has been suggested that the excess electron in isomer I in large sizes ( $n > 11$ ) resides in the interior of the water cluster, while that in the other isomers resides on the surface of the water cluster.<sup>41</sup> This picture of isomer I conforms to the generally accepted view about  $e^-_{\text{aq}}$ , in which the excess electron is

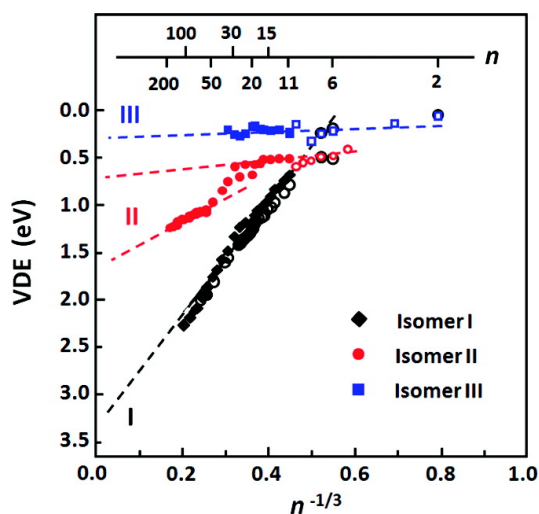


**Figure 1.1** Vertical detachment energies for the isomers of water cluster anions  $(\text{H}_2\text{O})_n^-$  as a function of  $n^{-1/3}$ . Reprint with permission from *Acc. Chem. Res.* 42, 2009, 769-777. Copyright 2009 American Chemical Society.

located in a cavity of the water network.<sup>53,54</sup>

At small sizes ( $n \leq 8$ ), however, there is a consensus that in all the isomeric forms the excess electron is bound to the surface of the water cluster in a specific arrangement of the hydrogen-bond network. The structures for these isomers have been addressed in depth by a series of vibrational predissociation spectroscopy combined with quantum chemical calculations.<sup>31-38</sup> For the  $(\text{H}_2\text{O})_6^-$  anions, which is most relevant to this dissertation, the structures of the two isomeric forms have been identified according to the vibrational spectral signatures. Figure 1.2 depicts the calculated structures of the  $(\text{H}_2\text{O})_6^-$  isomers. Type I isomer binds the excess electron with a single water molecule at a double hydrogen-bond acceptor (AA) site in the water network; both of the H atoms of the AA water point toward the diffuse electron cloud. In type II isomer, which has the lower electron binding energy, the excess electron is more delocalized and supported by several dangling H atoms of the water molecules at the different sites in the water network. These isomers are theoretically predicted to be close in energy<sup>46,47</sup> and generally observed to coexist in an ion beam of  $(\text{H}_2\text{O})_n^-$ ,<sup>32,33</sup> the distribution of the isomers changes depending on conditions of ion source. While the small  $(\text{H}_2\text{O})_n^-$  clusters with distinct hydrogen-bonding arrangement are obviously different from  $e^-_{\text{aq}}$ , the situation described above provides us with an opportunity to tackle an interesting question regarding the structural dynamics of the hydrogen-bond networks in water clusters: how the network structures rearrange upon incorporation of another molecule that can participate hydrogen bond and

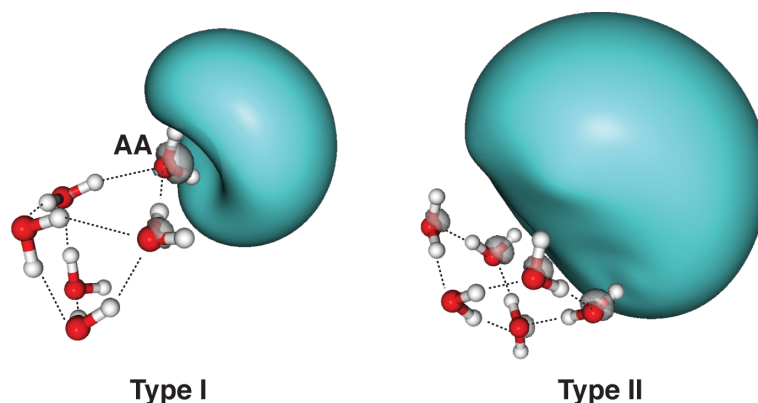


**Figure 1.2** Calculated structures of  $(\text{H}_2\text{O})_6^-$  isomers at the MP2/aug-cc-pVDZ+diff level. The notation AA indicates the electron-binding site in a double H-bond acceptor configuration. The blue shaded surfaces enclose 50% of the excess electron density.

whether or not the isomeric forms can interconvert without losing the excess electron during the incorporation processes. Hence, part of this dissertation aims to explore the rearrangement dynamics of the hydrogen-bond network of  $(\text{H}_2\text{O})_6^-$  during the association reactions with various molecules. The author has chosen alcohol molecules and benzene as the target reagents. The reaction with alcohols can be compared with the results of the homogeneous condensation,  $\text{D}_2\text{O} + (\text{H}_2\text{O})_6^-$ ,<sup>36</sup> which affords deeper insights into the mechanism in the condensation processes of  $(\text{H}_2\text{O})_n^-$ . The reaction with a benzene molecule allows us to investigate how a  $\pi \cdots \text{HO}$  hydrogen bond perturbs the water network.

The present study also deal with the reaction of  $(\text{H}_2\text{O})_6^-$  with an electron scavenging molecule. In aqueous solutions, the bulk  $e^-_{\text{aq}}$  act as a strong reducing agent; upon the encounter between  $e^-_{\text{aq}}$  and an electron scavenging molecule, the one-electron reduction readily occurs to form the aqueous anion,  $\text{M} + e^-_{\text{aq}} \rightarrow \text{M}^-_{\text{aq}}$ , whose reaction rates often reach the diffusion-controlled limit.<sup>55</sup> Although the reduction processes of  $e^-_{\text{aq}}$  have been extensively investigated in terms of kinetics, the dynamic details of those reactions have been obscured in the bulk environments and resistant to examination. Therefore, a fundamental question remains particularly in the molecular-level mechanism at play in the electron-transfer processes of  $e^-_{\text{aq}}$ . This process is a seemingly simple, but involves an elaborate interplay between hydrogen-bonding dynamics and electron dynamics; the diffuse electron in  $e^-_{\text{aq}}$  relocates into the more compact orbital in the electron scavenger, accompanying significant rearrangement of the water network. In order to gain such microscopic insights, the present study explores the gas-phase collisional reactions of  $(\text{H}_2\text{O})_6^-$  and nitromethane ( $\text{CH}_3\text{NO}_2$ ), which serves as a

cluster analog for the  $e^-_{\text{aq}}$  scavenging reaction of  $\text{CH}_3\text{NO}_2$  in solutions<sup>56</sup> and enable us to characterize the embryonic forms of the product anions in detail.

### ***Electron trapping of acetone***

Excess electrons trapped in non-aqueous environments provide us with a broader view about electron-solvent interactions, which are remarkably different from that in aqueous systems. Acetone ( $(\text{CH}_3)_2\text{CO}$ ) is a prototype of highly polar and aprotic solvent, which is known as a good electron scavenger in the solution phase; the valence anion of acetone,  $(\text{CH}_3)_2\text{CO}^-$ , is efficiently formed via electron transfer from reductive reagents.<sup>57</sup> Isolated in the gas-phase, on the other hand, the  $(\text{CH}_3)_2\text{CO}^-$  anion is unstable towards autodetachment,<sup>58</sup> a single acetone molecule has negative electron affinity and binds an excess electron only in a dipole-bound form<sup>59</sup> with its large dipole moment (2.88 D). This phase-dependent behavior for electron trapping of acetone has motivated the present study, in which the acetone cluster anions,  $[(\text{CH}_3)_2\text{CO}]_n^-$ , are prepared in the gas phase and their electronic properties are spectroscopically investigated in order to understand roles of solvation in achieving stability of the anionic forms of acetone.

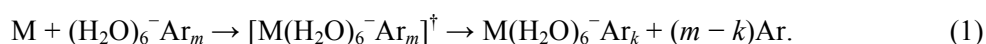
### ***Photodissociation of tri-iodide anion***

Study of photodissociation affords a unique insight into chemical dynamics involving bond cleavage, internal energy transfer, and energy relaxation. Moreover, dissociating behavior of a chromophore under solvated environments can be exploited to understand how solvation affects such dynamics. Photodissociation of the tri-iodide anion,  $\text{I}_3^-$ , provides an ideal opportunity for studying solvation effects on dissociation dynamics, since there is a sharp contrast between its photophysics in solutions and that in the gas phase.  $\text{I}_3^-$  is a well-known hypervalent species formed in polar solutions containing iodide salts and iodine through the equilibrium,  $\text{I}^- + \text{I}_2 \rightleftharpoons \text{I}_3^-$ . Its photoabsorption spectrum is dominated by the two intense bands at 360 and 290 nm.<sup>60</sup> It has been long known that photoexcitation of  $\text{I}_3^-$  in polar solutions results in the formation of  $\text{I}_2^-$  fragment.<sup>61,62</sup> On the other hand, both  $\text{I}^-$  and  $\text{I}_2^-$  fragments are produced by photodissociation in the gas-phase.<sup>63-66</sup> From these results, it has been suggested that the photoexcited  $\text{I}_3^-$  intrinsically undergoes nonadiabatic processes involving multiple excited-state potential surfaces, and that solvation exerts strong influence on the nonadiabatic dynamics. Despite the long-standing interest in the  $\text{I}_3^-$  photodissociation, its inherent nonadiabatic dynamics has not been fully understood, which is a prerequisite for microscopic understanding of the solvent effects. In this dissertation, photodissociation of the gas-phase  $\text{I}_3^-$  is examined in more detail than ever before with the goal of establishing a comprehensive picture of the nonadiabatic behavior of the dissociating  $\text{I}_3^-$ .

## 1.2 Thesis overview

### 1.2.1 Incorporation reactions of water cluster anions

The subsequent three chapters are focused on the gas-phase incorporation reactions of the water hexamer anion,  $M + (\text{H}_2\text{O})_6^- \rightarrow M(\text{H}_2\text{O})_6^-$ . Of particular interest in this process is floppiness or robustness of the hydrogen-bond network in  $(\text{H}_2\text{O})_6^-$  against the incorporation. The electronic and geometric properties of the  $M(\text{H}_2\text{O})_6^-$  product anions are investigated by photoelectron spectroscopy and *ab initio* calculations, and compared with those of the  $(\text{H}_2\text{O})_6^-$  reactant. The  $M(\text{H}_2\text{O})_6^-$  anions are synthesized by making use of the ‘‘Ar-mediated’’ association.<sup>24,36</sup>



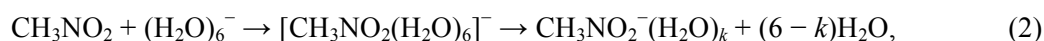
In this process, the excess energy gained from the collisional association between  $M$  and  $(\text{H}_2\text{O})_6^-$  is efficiently dissipated by evaporative loss of Ar atoms, which allows us to trap otherwise elusive complex anions; without Ar solvation, the nascent  $M(\text{H}_2\text{O})_6^-$  anions readily undergo thermionic electron emission or water evaporation.

Chapter 2 describes the uptake of an alcohol molecule in the  $(\text{H}_2\text{O})_6^-$  cluster ( $\text{ROH} + (\text{H}_2\text{O})_6^- \rightarrow \text{ROH}(\text{H}_2\text{O})_6^-$ ;  $\text{R}=\text{CH}_3, \text{C}_2\text{H}_5, 2\text{-C}_3\text{H}_7$ ). To microscopically address how an alcohol molecule can take part in the growth process of the hydrogen-bond network, structures of the  $\text{ROH}(\text{H}_2\text{O})_6^-$  products are investigated and compared with those of  $\text{D}_2\text{O}(\text{H}_2\text{O})_6^-$  produced in the homogeneous condensation process,  $\text{D}_2\text{O} + (\text{H}_2\text{O})_6^-$ , in which the  $\text{D}_2\text{O}$  molecule was found to randomly displace any site of the hydrogen-bond network, even the electron-binding AA water, during the  $\text{D}_2\text{O}(\text{H}_2\text{O})_6^-$  formation.<sup>36</sup> On the other hand, replaceable sites are obviously restricted for the ROH incorporation because they have only one OH group. From quantitative analysis of the product mass spectra, however, the relative cross sections of the  $\text{ROH}(\text{H}_2\text{O})_6^-$  formation are found to be almost same size as that of the  $\text{D}_2\text{O}(\text{H}_2\text{O})_6^-$  formation when  $\text{R}=\text{CH}_3$  and  $\text{C}_2\text{H}_5$ , but slightly smaller when  $\text{R}=2\text{-C}_3\text{H}_7$ . Photoelectron spectroscopic measurements reveals that the  $(\text{H}_2\text{O})_6^- \text{Ar}_m$  reactants are prepared initially in type I form, and that the  $\text{ROH}(\text{H}_2\text{O})_6^-$  products are formed preferentially in an isomeric form having the hydrogen-bond network associated with type I isomer of  $(\text{H}_2\text{O})_7^-$ ; the type I motif is almost retained during the ROH incorporation and the product anions are only slightly subject to type I  $\rightarrow$  type II isomeric interconversion. It is also revealed that the isomeric distribution of the  $\text{ROH}(\text{H}_2\text{O})_6^-$  products are almost equal to that of the  $\text{D}_2\text{O}(\text{H}_2\text{O})_6^-$  product. Based on these results, in conjunction with *ab initio* results of  $\text{CH}_3\text{OH}(\text{H}_2\text{O})_6^-$ , it is concluded that the incorporation takes place in the same manner for both ROH and  $\text{D}_2\text{O}$  at least in the initial stage of the reaction, suggesting that the process starts with a molecular uptake nearby a specific single hydrogen-bond donor site located away from the electron-binding AA water molecule.

In Chapter 3, the study is then extended to the reaction with a benzene (Bz) molecule to explore

the influence of non-conventional hydrogen-bonding ( $\pi \cdots \text{HO}$ ) interactions on the hydration structure. Although type I isomer of  $(\text{H}_2\text{O})_6^-$  has been observed to be robust against isomerization into type II isomer upon vibrational excitation and the  $\text{D}_2\text{O}$  incorporation,<sup>36,37</sup> photoelectron spectrum of  $\text{Bz}(\text{H}_2\text{O})_6^-$  produced in the Ar-mediated association signifies that type I  $\rightarrow$  type II interconversion efficiently occurs within the hydrogen-bond network of  $(\text{H}_2\text{O})_6^-$  when it interacts with Bz. *Ab initio* study on  $\text{Bz}(\text{H}_2\text{O})_6^-$  structures shows that both type isomers of  $(\text{H}_2\text{O})_6^-$  interact with Bz through a non-conventional  $\pi$ -hydrogen bond ( $\pi \cdots \text{HO}$ ), while the H-bond network of the  $(\text{H}_2\text{O})_6^-$  isomers remains almost intact. Close inspection of the energetics at play reveals that the association of Bz stabilizes the type II configuration more favorably than the type I configuration, which consequently drives the isomer interconversion.

In Chapter 4, the focus is turned to the gas-phase variation of the  $e^-_{\text{aq}}$  scavenging reaction of  $\text{CH}_3\text{NO}_2$ . The work presented in this chapter applies the Ar-mediated approach to the one-electron reduction process between  $\text{CH}_3\text{NO}_2$  and  $(\text{H}_2\text{O})_6^-$ ,



in order to trap and characterize the intermediate  $[\text{CH}_3\text{NO}_2(\text{H}_2\text{O})_6]^-$  anion. Photoelectron spectroscopy of  $[\text{CH}_3\text{NO}_2(\text{H}_2\text{O})_6]^-$  formed via the Ar-mediated association reveals that the  $(\text{H}_2\text{O})_6^-$  anion attaches  $\text{CH}_3\text{NO}_2$  via dipole interaction with retaining the electronic and geometric nature of the  $(\text{H}_2\text{O})_6^-$  reactant. The near IR photoexcitation of the  $[\text{CH}_3\text{NO}_2(\text{H}_2\text{O})_6]^-$  anion results in either electron detachment or fragmentation, the latter of which leads to transformation into the hydrated valence anion,  $\text{CH}_3\text{NO}_2^-(\text{H}_2\text{O})_3$ . This demonstrates that the intracluster electron transfer can be triggered by photoexcitation, and that the  $[\text{CH}_3\text{NO}_2(\text{H}_2\text{O})_6]^-$  anion prepared in the present study plays a role of a doorway state into the valence anion,  $\text{CH}_3\text{NO}_2^-$ , building a unique platform to study the electron transfer dynamics under well-defined hydration environment.

## 1.2.2 Electron trapping mechanism of acetone clusters

Chapter 5 examines the electronic and geometric properties of the acetone cluster anions,  $[(\text{CH}_3)_2\text{CO}]_n^-$ , in order to address the mechanism for the excess electron trapping. In this work, photoelectron imaging spectroscopy are employed to determine the VDEs and photoelectron angular distributions (PADs) of  $[(\text{CH}_3)_2\text{CO}]_n^-$ , ( $n = 2, 5-15$ ). The size dependence of the observed VDEs and PADs indicates that the electronic properties of  $n = 2$  are quite distinct from those of  $n \geq 5$ . With the aid of *ab initio* calculations, the  $n = 2$  anion is attributed to a charge-resonance dimer anion  $[(\text{CH}_3)_2\text{CO}]_2^-$ , where the excess electron is equally shared between the two acetone moieties. As for  $[(\text{CH}_3)_2\text{CO}]_n^-$  with  $n = 5-15$ , the comparison with the VDEs of the hydrated acetone anion clusters,  $(\text{CH}_3)_2\text{CO}^-(\text{H}_2\text{O})_m$  ( $m \geq 4$ ), leads us to conclude that the solvent-stabilized monomer anion,

$(\text{CH}_3)_2\text{CO}^-((\text{CH}_3)_2\text{CO})_{n-1}$  are formed in the clusters; at least four polar solvents are required to stabilize the  $(\text{CH}_3)_2\text{CO}^-$  anion.

### 1.2.3 Nonadiabatic photodissociation dynamics of gas-phase tri-iodide anion

Chapter 6 concerns photodissociation dynamics of the tri-iodide anion,  $\text{I}_3^-$  isolated in the gas phase. As mentioned in section 1.1.2, photodissociation of  $\text{I}_3^-$  has been already investigated both in solutions and in the gas phase; while  $\text{I}_3^-$  in polar solutions directly photodissociates into the  $\text{I}_2^-$  fragment, the gas-phase photodissociation results in competitive occurrence of multiple dissociation pathways,  $\text{I} + \text{I}_2^-$ ,  $\text{I}^- + \text{I}_2$ , and  $\text{I}^- + 2\text{I}$ .<sup>63-66</sup> The complicated photophysics of  $\text{I}_3^-$  stems from the congested excited-state potential energy surfaces<sup>67,68</sup> due to the strong spin-orbit interactions of heavy iodine atoms. Accordingly, there are many dissociation channels that are energetically accessible by the photoexcitation,<sup>66</sup> as illustrated in Fig. 1.3; the measured branching ratios among those dissociation channels have been still disputed.<sup>64-66</sup> In order to answer a question regarding how the dissociating  $\text{I}_3^-$  in solutions experiences solvent effects and eventually reaches the  $\text{I}_2^- + \text{I}$  limit, it is essential to obtain more accurate and complete description of the photodissociation dynamics of the bare  $\text{I}_3^-$ .

The purpose of Chapter 6 is to unravel the complicated dissociation pathways of bare  $\text{I}_3^-$  in the excitation energy range from 3.26 – 4.27 eV (380 – 290 nm), which covers the two photoabsorption

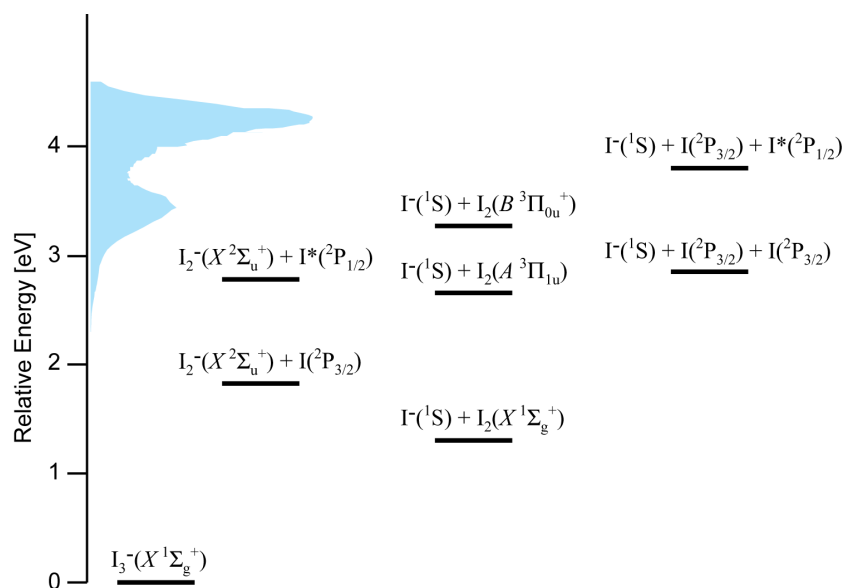


**Figure 1.3** Relative energy level diagram of the dissociation asymptotes of  $\text{I}_3^-$  with reference to the ground state  $\text{I}_3^-$ . The blue shaded area represents the photoabsorption bands of  $\text{I}_3^-$ .

bands of  $\text{I}_3^-$  (Fig. 1.3). The present work employs high-resolution photofragment translational spectroscopy to measure the translational energy and angular distributions of the photofragment anions and neutrals. From analysis of the observed photofragment translational energy distributions, the dissociation channels responsible for the  $\text{I}^-$  and  $\text{I}_2^-$  production are comprehensively assigned and their branching fractions are determined. The measurements show that in the whole range of the excitation energy, the three-body dissociation ( $\text{I}^- + 2\text{I}$ ) accounts for 30–40% of the photofragmentation yield and preferentially proceeds as  $\text{I}^-(^1\text{S}) + \text{I}(^2\text{P}_{3/2}) + \text{I}(^2\text{P}_{3/2})$ , where the excess charge resides on the end I atoms. In the lower-energy band, the two-body dissociation is dominated by the  $\text{I}^-(^1\text{S}) + \text{I}_2(\text{X or A})$  channel with a tiny contribution from the  $\text{I}_2^-(\text{X}) + \text{I}(^2\text{P}_{3/2})$  channel. In the higher-energy band, the two-body dissociation primarily occurs as the  $\text{I}_2^-(\text{X}) + \text{I}^*(^2\text{P}_{1/2})$  channel along with the  $\text{I}^-(^1\text{S}) + \text{I}_2(\text{B})$  channel. The photodissociation dynamics of gas-phase  $\text{I}_3^-$  is then interpreted as nonadiabatic processes evolving on the excited-state potential energy surfaces obtained by spin-orbit configuration interaction calculations,<sup>69</sup> which reveals the conical intersections and avoided crossings playing key roles in determining the photoproduct branching. This work lays the groundwork for further investigation into the photodissociation of partially solvated  $\text{I}_3^-$  clusters,  $\text{I}_3^-(\text{S})_n$ , in the gas phase, which will provide us with more detailed insights into the solvent effect on the nonadiabatic dynamics of the  $\text{I}_3^-$  photodissociation.



## References

- 1 Castleman, A. W., Jr; Keesee, R. G. *Chem. Rev.* **1986**, *86*, 589–618.
- 2 Castleman, A. W.; Bowen, K. H., Jr. *J. Phys. Chem.* **1996**, *100*, 12911–12944.
- 3 Bieske, E. J.; Maier, J. P. *Chem. Rev.* **1993**, *93*, 2603–2621.
- 4 Sanov, A.; Carl Lineberger, W. *Phys. Chem. Chem. Phys.* **2004**, *6*, 2018–2032.
- 5 Wang, X.-B.; Wang, L.-S. *Annu. Rev. Phys. Chem.* **2009**, *60*, 105–126.
- 6 Sanov, A.; Mabbs, R. *Int. Rev. Phys. Chem.* **2008**, *27*, 53–85.
- 7 Sanov, A. *Annu. Rev. Phys. Chem.* **2014**, *65*, 341–363.
- 8 Jarrold, M. F.; Illies, A. J.; Bowers, M. T. *J. Chem. Phys.* **1984**, *81*, 222–230.
- 9 Butler, L. J.; Neumark, D. M. *J. Phys. Chem.* **1996**, *100*, 12801–12816.
- 10 Asmis, K. R.; Neumark, D. M. *Acc. Chem. Res.* **2012**, *45*, 43–52.
- 11 Wolk, A. B.; Leavitt, C. M.; Garand, E.; Johnson, M. A. *Acc. Chem. Res.* **2014**, *47*, 202–210.
- 12 Hart, E. J.; Boag, J. W. *J. Am. Chem. Soc.* **1962**, *84*, 4090–4095.
- 13 Garrett, B. C.; Dixon, D. A.; Camaioni, D. M.; Chipman, D. M.; Johnson, M. A.; Jonah, C. D.; Kimmel, G. A.; Miller, J. H.; Rescigno, T. N.; Rossky, P. J.; Xantheas, S. S.; Colson, S. D.; Laufer, A. H.; Ray, D.; Barbara, P. F.; Bartels, D. M.; Becker, K. H.; Bowen, K. H., Jr.; Bradforth, S. E.; Carmichael, I.; Coe, J. V.; Corrales, L. R.; Cowin, J. P.; Dupuis, M.; Eisenthal, K. B.; Franz, J. A.; Gutowski, M. S.; Jordan, K. D.; Kay, B. D.; LaVerne, J. A.; Lyman, S. V.; Madey, T. E.; McCurdy, C. W.; Meisel, D.; Mukamel, S.; Nilsson, A. R.; Orlando, T. M.; Petrik, N. G.; Pimblott, S. M.; Rustad, J. R.; Schenter, G. K.; Singer, S. J.; Tokmakoff, A.; Wang, L.-S.; Zwier, T. S. *Chem. Rev.* **2005**, *105*, 355–390.
- 14 Simons, J. *Acc. Chem. Res.* **2006**, *39*, 772–779.
- 15 Posey, L. A.; Johnson, M. A. *J. Chem. Phys.* **1988**, *89*, 4807–4814.
- 16 Posey, L. A.; Deluca, M. J.; Campagnola, P. J.; Johnson, M. A. *J. Phys. Chem.* **1989**, *93*, 1178–1181.
- 17 Arnold, S. T.; Morris, R. A.; Viggiano, A. A.; Johnson, M. A. *J. Phys. Chem.* **1996**, *100*, 2900–2906.
- 18 Balaj, O. P.; Siu, C.-K.; Balteanu, I.; Beyer, M. K.; Bondybey, V. E. *Int. J. Mass Spectrom.* **2004**, *238*, 65–74.
- 19 Balaj, O. P.; Siu, C.-K.; Balteanu, I.; Beyer, M. K.; Bondybey, V. E. *Chem. Eur. J.* **2004**, *10*, 4822–4830.
- 20 Siu, C.-K.; Balaj, O. P.; Bondybey, V. E.; Beyer, M. K. *J. Am. Chem. Soc.* **2007**, *129*, 3238–3246.
- 21 Coe, J. V.; Lee, G. H.; Eaton, J. G.; Arnold, S. T.; Sarkas, H. W.; Bowen, K. H., Jr.; Ludewigt, C.; Haberland, H.; Worsnop, D. R. *J. Chem. Phys.* **1990**, *92*, 3980–3982.

- 22 Kim, J.; Becker, I.; Cheshnovsky, O.; Johnson, M. A. *Chem. Phys. Lett.* **1998**, 297, 90–96.
- 23 Lee, G. H.; Arnold, S. T.; Eaton, J. G.; Bowen, K. H., Jr. *Chem. Phys. Lett.* **2000**, 321, 333–337.
- 24 Shin, J.-W.; Hammer, N. I.; Headrick, J. M.; Johnson, M. A. *Chem. Phys. Lett.* **2004**, 399, 349–353.
- 25 Verlet, J.; Bragg, A. E.; Kammrath, A.; Cheshnovsky, O.; Neumark, D. M. *Science* **2005**, 307, 5706, 93–96.
- 26 Coe, J. V.; Arnold, S. T.; Eaton, J. G.; Lee, G. H.; Bowen, K. H., Jr. *J. Chem. Phys.* **2006**, 125, 014315.
- 27 Coe, J. V.; Williams, S. M.; Bowen, K. H., Jr. *Int. Rev. Phys. Chem.* **2008**, 27, 27–51.
- 28 Ma, L.; Majer, K.; Chirof, F.; Issendorff, von, B. *J. Chem. Phys.* **2009**, 131, 144303.
- 29 Maeyama, T.; Tsumura, T.; Fujii, A.; Mikami, N. *Chem. Phys. Lett.* **1997**, 264, 292–296.
- 30 Ayotte, P.; Johnson, M. A. *J. Chem. Phys.* **1997**, 106, 811–814.
- 31 Roscioli, J. R.; Weddle, G. H.; Shin, J. W.; Hammer, N. I.; Johnson, M. A.; Diken, E. G.; Headrick, J. M. *Science* **2004**, 306, 675–679.
- 32 Hammer, N. I.; Roscioli, J. R.; Johnson, M. A. *J. Phys. Chem. A* **2005**, 109, 7896–7901.
- 33 Roscioli, J. R.; Hammer, N. I.; Johnson, M. A. *J. Phys. Chem. A* **2006**, 110, 7517–7520.
- 34 Roscioli, J. R.; Johnson, M. A. *J. Chem. Phys.* **2007**, 126, 024307.
- 35 Roscioli, J. R.; Hammer, N. I.; Johnson, M. A.; Diri, K.; Jordan, K. D. *J. Chem. Phys.* **2008**, 128, 104314.
- 36 McCunn, L. R.; Headrick, J. M.; Johnson, M. A. *Phys. Chem. Chem. Phys.* **2008**, 10, 3118–3123.
- 37 McCunn, L. R.; Gardenier, G. H.; Guasco, T. L.; Elliott, B. M.; Bopp, J. C.; Relph, R. A.; Johnson, M. A. *J. Chem. Phys.* **2008**, 128, 234311.
- 38 Guasco, T. L.; Elliott, B. M.; Johnson, M. A.; Ding, J.; Jordan, K. D. *J. Phys. Chem. Lett.* **2010**, 1, 2396–2401.
- 39 Bragg, A. E.; Verlet, J. R. R.; Kammrath, A.; Cheshnovsky, O.; Neumark, D. M. *Science* **2004**, 306, 669–671.
- 40 Bragg, A. E.; Verlet, J. R. R.; Kammrath, A.; Cheshnovsky, O.; Neumark, D. M. *J. Am. Chem. Soc.* **2005**, 127, 15283–15295.
- 41 Neumark, D. M. *Mol. Phys.* **2008**, 106, 2183–2197.
- 42 Ehrler, O. T.; Neumark, D. M. *Acc. Chem. Res.* **2009**, 42, 769–777.
- 43 Tsurusawa, T.; Iwata, S. *Chem. Phys. Lett.* **1999**, 315, 433–440.
- 44 Lee, H. M.; Suh, S. B.; Tarakeshwar, P.; Kim, K. S. *J. Chem. Phys.* **2005**, 122, 044309.
- 45 Sommerfeld, T.; Jordan, K. D. *J. Am. Chem. Soc.* **2006**, 128, 5828–5833.
- 46 Herbert, J. M.; Head-Gordon, M. *J. Am. Chem. Soc.* **2006**, 128, 13932–13939.
- 47 Yagi, K.; Okano, Y.; Sato, T.; Kawashima, Y.; Tsuneda, T.; Hirao, K. *J. Phys. Chem. A* **2008**,

- 112, 9845–9853.
- 48 Jacobson, L. D.; Herbert, J. M. *J. Am. Chem. Soc.* **2011**, *133*, 19889–19899.
- 49 Siefertmann, K. R.; Liu, Y.; Lugovoy, E.; Link, O.; Faubel, M.; Buck, U.; Winter, B.; Abel, B. *Nature Chemistry* **2010**, *2*, 274–279.
- 50 Lübcke, A.; Buchner, F.; Heine, N.; Hertel, I. V.; Schultz, T. *Phys. Chem. Chem. Phys.* **2010**, *12*, 14629.
- 51 Tang, Y.; Shen, H.; Sekiguchi, K.; Kurahashi, N.; Mizuno, T.; Suzuki, Y.-I.; Suzuki, T. *Phys. Chem. Chem. Phys.* **2010**, *12*, 3653.
- 52 Shreve, A. T.; Yen, T. A.; Neumark, D. M. *Chem. Phys. Lett.* **2010**, *493*, 216–219.
- 53 Feng, D.-F.; Kevan, L. *Chem. Rev.* **1980**, *80*, 1–20.
- 54 Turi, L. *J. Chem. Theory Comput.* **2015**, *11*, 1745–1755.
- 55 Buxton, G. V.; Greenstock, C. L.; Helman, W. P. *J. Phys. Chem. Ref. Data* **1988**, *17*, 513.
- 56 Asmus, K. D.; Taub, I. A. *J. Phys. Chem.* **1968**, *72*, 3382–3387.
- 57 Scholes, G.; Simic, M.; Weiss, J. J. *Nature* **1960**, *188*, 1019–1020.
- 58 Naff, W. T.; Compton, R. N.; Cooper, C. D. *J. Chem. Phys.* **1972**, *57*, 1303–1307.
- 59 Desfrancois, C.; Abdoul-Carime, H.; Khelifa, N.; Schermann, J. P. *Phys. Rev. Lett.* **1994**, *73*, 2436–2439.
- 60 Awtrey, A. D.; Connick, R. E. *J. Am. Chem. Soc.* **1951**, *73*, 1842–1843.
- 61 Roy, J. C.; Hamill, W. H.; Williams, R. R., Jr. *J. Am. Chem. Soc.* **1955**, *77*, 2953–2957.
- 62 Grossweiner, L. I.; Matheson, M. S. *J. Phys. Chem.* **1957**, *61*, 1089–1095.
- 63 Zanni, M. T.; Greenblatt, B. J.; Davis, A. V.; Neumark, D. M. *J. Chem. Phys.* **1999**, *111*, 2991–3003.
- 64 Choi, H.; Bise, R. T.; Hoops, A. A. *J Chem Phys* **2000**, *113*, 2255–2262.
- 65 Zhu, L.; Takahashi, K.; Saeki, M.; Tsukuda, T.; Nagata, T. *Chem. Phys. Lett.* **2001**, *350*, 233–239.
- 66 Hoops, A. A.; Gascooke, J. R.; Faulhaber, A. E.; Kautzman, K. E.; Neumark, D. M. *J. Chem. Phys.* **2004**, *120*, 7901–7909.
- 67 Vala, J.; Kosloff, R.; Harvey, J. N. *J. Chem. Phys.* **2001**, *114*, 7413–7423.
- 68 Gomes, A. S. P.; Visscher, L.; Bolvin, H.; Saue, T.; Knecht, S.; Fleig, T.; Eliav, E. *J. Chem. Phys.* **2010**, *133*, 064305.
- 69 Yabushita, S.; Zhang, Z.; Pitzer, R. M. *J. Phys. Chem. A* **1999**, *103*, 5791–5800.



## Chapter 2

# Incorporation of ROH (R = CH<sub>3</sub>, C<sub>2</sub>H<sub>5</sub>, 2-C<sub>3</sub>H<sub>7</sub>) into (H<sub>2</sub>O)<sub>6</sub><sup>-</sup>: Substituent effect on growth process of the hydrogen-bond network

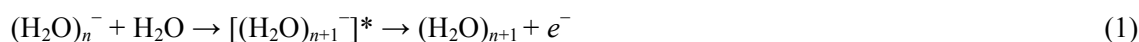
### ABSTRACT

The condensation reaction of water cluster anions,  $(\text{H}_2\text{O})_n^- + \text{H}_2\text{O} \rightarrow (\text{H}_2\text{O})_{n+1}^-$ , offers a prime opportunity to explore the growth process of the hydrogen-bond network involving molecular uptake and network rearrangement. Here, by exploiting an Ar-mediated approach, we investigate the association reaction of water hexamer anions,  $(\text{H}_2\text{O})_6^-$ , with ROH (R = CH<sub>3</sub>, C<sub>2</sub>H<sub>5</sub>, 2-C<sub>3</sub>H<sub>7</sub>) by mass spectrometry combined with photoelectron spectroscopy. Quantitative analysis of the product mass spectra reveals that incorporation of ROH (R = CH<sub>3</sub>, C<sub>2</sub>H<sub>5</sub>) into  $(\text{H}_2\text{O})_6^-$  occurs with a cross section of the same size as in the  $(\text{H}_2\text{O})_6^- + \text{D}_2\text{O}$  condensation, but with a slightly smaller cross section for R = 2-C<sub>3</sub>H<sub>7</sub>. Coexistence of two types of isomers, high electron-binding (type I) and low electron-binding (type II) forms, is observed in all the product ROH· $(\text{H}_2\text{O})_6^-$  species by photoelectron spectroscopic measurement. These findings, in conjunction with ab initio study of MeOH· $(\text{H}_2\text{O})_6^-$  structures, lead us to propose a molecular uptake mechanism at play in the incorporation of ROH into the  $(\text{H}_2\text{O})_6^-$  network. This also provides complementary information on the homogeneous condensation process of pure water cluster anions.

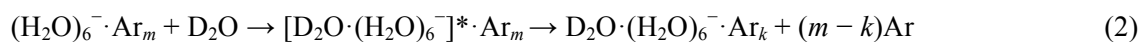
This chapter has been reproduced in part with permission from the following previously published article: Nakanishi, R.; Nagata, T. *Journal of Physical Chemistry A*, 2014, 118, 7360-7366. DOI: 10.1021/jp4121589 Copyright 2014 American Chemical Society

## 2.1 Introduction

The water cluster anions,  $(\text{H}_2\text{O})_n^-$ , have been a subject of many experimental and theoretical studies as the gas-phase analogues of the hydrated electron,  $e^-_{\text{aq}}$ , in solution. In those studies, much attention has been directed toward the geometrical structures and stabilities, the electron trapping mechanism and the formation processes of  $(\text{H}_2\text{O})_n^-$  of various sizes, which eventually show up in a tangible form as the distinct intensity anomalies in the ion distributions of  $(\text{H}_2\text{O})_n^-$ .<sup>1</sup> It has also been revealed by photoelectron spectroscopy that  $(\text{H}_2\text{O})_n^-$  anions are produced in several different isomeric forms, denoted as types I, I', II and III according to their vertical detachment energies.<sup>2-6</sup> Infrared vibrational predissociation spectroscopy has provided more detailed information on the electron binding sites of  $(\text{H}_2\text{O})_n^-$ .<sup>6-13</sup> In spite of those extensive investigations using a variety of experimental ingenuities, there remains a difficulty encountered in studying the growth-by-condensation process of the water cluster anions by binary-collisional reaction,  $(\text{H}_2\text{O})_n^- + \text{H}_2\text{O}$ . The difficulty arises from intrinsic properties of the weakly electron-binding species in that the reaction proceeds predominantly as associative electron detachment for  $n < 15$ :<sup>14</sup>



Recently, Johnson and his coworkers have demonstrated an ingenious way to circumvent this problem; they investigated the condensation reaction between  $(\text{H}_2\text{O})_6^-$  and  $\text{D}_2\text{O}$  by employing an Ar-mediated approach:<sup>15, 16</sup>



In process 2, rapid energy dissipation is accomplished by the evaporation of Ar solvents and, as a result, the condensation products can survive the thermionic electron emission. Their infrared spectroscopic study of the product anions revealed distinctive features of process 2: (i) Most of the product  $\text{D}_2\text{O} \cdot (\text{H}_2\text{O})_6^- \cdot \text{Ar}_k$  anions take on either type I' or II form although the reactant  $(\text{H}_2\text{O})_6^- \cdot \text{Ar}_m$  anions are initially prepared in type I form, (ii) In the type I' product anions, incorporated  $\text{D}_2\text{O}$  can migrate even into the electron-binding site, where a single water molecule resides as a double H-bond acceptor (AA), (iii) In the type II product anions,  $\text{D}_2\text{O}$  preferentially occupies the sites responsible to the vibrational signature of the isomeric form.<sup>15</sup> These findings indicate an inevitable occurrence of drastic rearrangement of the hydrogen-bond network of  $(\text{H}_2\text{O})_n^-$  during the growth-by-condensation.

Considering that  $\text{H}_2\text{O}$  is a unique species that can form hydrogen bonds in a double ionic hydrogen-bonding (DIHB) configuration, one may have a naive question as to how the condensation reaction proceeds when an ROH molecule, which only forms a single ionic hydrogen-bond (SIHB), is incorporated into  $(\text{H}_2\text{O})_n^-$  instead. In the present study, collisional association reactions between  $(\text{H}_2\text{O})_6^- \cdot \text{Ar}_m$  and ROH ( $\text{R} = \text{CH}_3, \text{C}_2\text{H}_5, 2\text{-C}_3\text{H}_7$ ) are investigated by the Ar-mediated approach

combined with mass spectrometry and photoelectron spectroscopy. Mass spectrometric measurements provide information on the relative cross section for the incorporation process,



Product branching into type I, I' and II forms is then probed by photoelectron spectroscopy. Our interest is focused mainly on whether or not the lack of DIHB ability makes a crucial difference in the condensation processes involving a substantial rearrangement of the hydrogen-bond networks. Experimental results are compared with the  $(\text{H}_2\text{O})_6^- \cdot \text{Ar}_m + \text{D}_2\text{O}$  result quantitatively in terms of the incorporation cross sections and isomer branching fractions in the product anions, which offers further insight into the incorporation mechanism operative in the condensation reactions of  $(\text{H}_2\text{O})_n^-$ .

## 2.2 Experimental

The experimental apparatus used in the present study consists of a cluster ion source, a time-of-flight (TOF) mass spectrometer and a photoelectron spectrometer. Details of the apparatus has been described elsewhere.<sup>17,18</sup> The  $(\text{H}_2\text{O})_n^- \cdot \text{Ar}_m$  reactants were prepared in an electron-impact ionized free jet. An argon gas containing a trace amount of water ( $\approx 0.2\%$  by volume) was expanded through a pulsed nozzle at a stagnation pressure of  $\approx 0.4$  MPa. The free jet was then crossed with a 200-eV electron beam at the expansion region. In the ionized jet secondary slow electrons produced by the electron impact were captured successively by preexisting neutral  $(\text{H}_2\text{O})_N \text{Ar}_M$  clusters, resulting in the formation of  $(\text{H}_2\text{O})_n^- \cdot \text{Ar}_m$ . When the target ROH was introduced through an effusive nozzle into the source chamber, the ambient pressure was increased typically up to  $4.0 \times 10^{-3}$  Pa. The sample-gas flow was regulated by a metering valve so as to introduce ROH molecules at the same pressure for all the samples. The pressure was monitored by an ionization gauge, of which the relative sensitivity was calibrated to the ionization cross-section of each ROH. The  $(\text{H}_2\text{O})_n^- \cdot \text{Ar}_m$  clusters reacted with the ambient ROH while drifting in the source chamber. The product anions were extracted at  $\approx 15$  cm downstream from the nozzle, perpendicularly to the initial beam direction by applying a pulsed electric field. The anions were further accelerated up to 1.25 keV, and mass-analyzed by a 1.9-m TOF mass spectrometer.

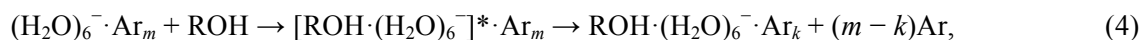
Photoelectron measurements were performed at 1064 nm by using a velocity-map imaging (VMI)<sup>19</sup> photoelectron spectrometer equipped at the end of the TOF mass spectrometer. The anions of interest, mass-selected prior to entering the VMI spectrometer, were intersected with the output of a pulsed Nd:YAG laser at the center of the spectrometer. Photoelectrons were extracted perpendicular to both the ion and laser beams by a static electric field, and projected onto a 40-mm diameter microchannel plate (MCP) coupled to a phosphor screen. The MCP was gated with a 300-ns time

window coincident with the photoelectron arrival in order to reduce background noise. The photoelectron images on the phosphor screen were recorded using a CCD camera (512×512 pixels). The images were acquired typically for 20 000 – 60 000 laser shots. Photoelectron spectra were reconstructed from the obtained images using the basis set expansion (BASEX) method.<sup>20</sup> The spectral resolution was  $\approx 40$  meV at the photoelectron kinetic energy of 500 meV after the reconstruction procedure. The measured electron kinetic energy was calibrated against the known photoelectron bands of  $\text{O}_2^{-21}$  and  $\Gamma^{-22}$ .

## 2.3 Results and discussion

### 2.3.1 ROH uptake measurement

Figure 2.1 displays the ion distributions measured before and after the entrainment of ROH molecules into the  $(\text{H}_2\text{O})_n^- \cdot \text{Ar}_m$  beam. As shown in Fig. 2.1(a), the reactant ion distribution exhibits an abrupt onset at  $(n, m) = (6, 0)$  followed by the  $(n, m)$  series with  $n = 6$  and 7, and  $m \leq 12$ . The  $(\text{H}_2\text{O})_n^- \cdot \text{Ar}_m$  anions with  $n \geq 8$  appear only as minor species in the mass spectrum. The characteristic ion distribution is attributable to the distinctive ability of neutral precursors,  $(\text{H}_2\text{O})_6$  and  $(\text{H}_2\text{O})_7$ , to form dipole-bound anions.<sup>23</sup> This enables us to exploit the ion source as coarsely  $n$ -selected  $(\text{H}_2\text{O})_n^- \cdot \text{Ar}_m$  reagents. When ROH molecules were entrained into the beam, the intensities of the reactant mass peaks were reduced by  $\sim 50\%$  and product mass peaks emerged in the spectra (ures 5.1(b) – (e)). These mass peaks are assignable to  $\text{ROH} \cdot (\text{H}_2\text{O})_n^-$  ( $n = 6 - 10$ ) according to their  $m/z$  values. Among these product anions, we focus our attention on  $\text{ROH} \cdot (\text{H}_2\text{O})_6^-$  for the study of incorporation processes between the water cluster anion and ROH because a wealth of information is available on the structural and spectral properties of  $(\text{H}_2\text{O})_6^-$ .<sup>8</sup> In analogy with the  $(\text{H}_2\text{O})_6^- \cdot \text{Ar}_m + \text{D}_2\text{O}$  reaction,<sup>15</sup> we expect that the Ar-mediated association process between  $(\text{H}_2\text{O})_6^- \cdot \text{Ar}_m$  and ROH proceeds primarily as



where the size of the water clusters anions is preserved as-is during the reaction. This inference is, as will be understood, in consonance with the fact that  $\text{ROH} \cdot (\text{H}_2\text{O})_5^-$  anions have never been detected in the mass analysis of the product anions.

The entrainment experiments were performed under the condition that ROH sample gas was introduced into the source chamber at the same partial pressure for all the target molecules. We also confirmed that product ion intensities increased proportionally with the sample gas pressure under our experimental conditions. The measurement was made also for the reaction with  $\text{D}_2\text{O}$  under the identical condition. By making use of this situation, relative cross sections for the collisional



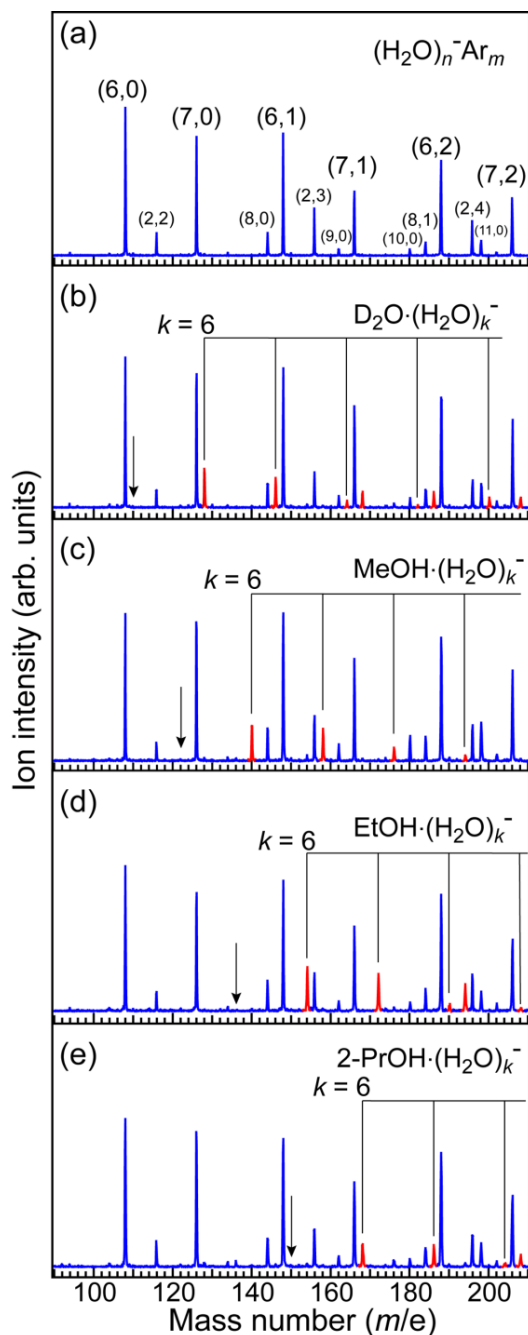


**Figure 2.1** Mass spectra of the  $(\text{H}_2\text{O})_n^- \text{Ar}_m$  reactants (a) and those after the reactions with (b)  $\text{D}_2\text{O}$ , (c)  $\text{CH}_3\text{OH}$ , (d)  $\text{C}_2\text{H}_5\text{OH}$  and (e)  $2\text{-C}_3\text{H}_7\text{OH}$ . The product  $\text{ROH} \cdot (\text{H}_2\text{O})_k^-$  peaks, interspersed between the unreacted  $(\text{H}_2\text{O})_n^- \text{Ar}_m$  peaks, are indicated in red. Note that the vertical scale is expanded by a factor of 2 in traces (b) – (e). The formula  $(\text{H}_2\text{O})_n^- \text{Ar}_m$  is abbreviated as  $(n, m)$  in the top trace. The arrows indicate the positions where  $\text{ROH} \cdot (\text{H}_2\text{O})_5^-$  peaks would appear.

condensation process (eq 4) can be evaluated from the mass peak intensities of the product anions. The relative cross sections are calculated as

$$\sigma_{rel} = C \left[ \frac{\sum_k I[\text{ROH} \cdot (\text{H}_2\text{O})_6^- \cdot \text{Ar}_k]}{\sum_m I[(\text{H}_2\text{O})_6^- \cdot \text{Ar}_m]} \right] \quad (5)$$

where  $I[(\text{H}_2\text{O})_6^- \cdot \text{Ar}_m]$  and  $I[\text{ROH} \cdot (\text{H}_2\text{O})_6^- \cdot \text{Ar}_k]$  represent the signal intensity of the  $(\text{H}_2\text{O})_6^- \cdot \text{Ar}_m$  peak before the entrainment and that of  $\text{ROH} \cdot (\text{H}_2\text{O})_6^- \cdot \text{Ar}_k$  after the reaction, respectively. The sum of  $I[(\text{H}_2\text{O})_6^- \cdot \text{Ar}_m]$  over  $m = 6 - 8$  is employed as the estimate for the total amount of reactant anions and that of  $I[\text{ROH} \cdot (\text{H}_2\text{O})_6^- \cdot \text{Ar}_k]$  over  $k = 0 - 2$  for product anions. The coefficient,  $C$ , in eq 5 is determined so that  $\sigma_{rel}$  become unity for the  $\text{D}_2\text{O}$  reaction. The cross sections thus determined are 0.99(10), 1.11(20) and 0.78(21) for  $\text{R} = \text{CH}_3$ ,  $\text{C}_2\text{H}_5$  and  $2\text{-C}_3\text{H}_7$ , respectively. The digits in parentheses represent uncertainties estimated from the intensity analysis of several sets of mass spectral data. The  $\sigma_{rel}$  value for  $\text{D}_2\text{O}$  is unity by definition. It can be inferred from these  $\sigma_{rel}$  values that process 4 occurs with an almost equal cross section for  $\text{D}_2\text{O}$ ,  $\text{CH}_3\text{OH}$  and  $\text{C}_2\text{H}_5\text{OH}$ , while with a smaller cross section for  $2\text{-C}_3\text{H}_7\text{OH}$ .

### 2.3.2 Photoelectron spectra

Figure 2.2 shows the photoelectron spectra of the  $\text{ROH} \cdot (\text{H}_2\text{O})_6^-$  products. Also shown for comparison are the spectra of  $(\text{H}_2\text{O})_6^- \cdot \text{Ar}_6$  (top trace) and  $(\text{H}_2\text{O})_7^-$  (bottom trace) existing in the reactant beam prior to  $\text{ROH}$  entrainment. We propose here that  $(\text{H}_2\text{O})_6^- \cdot \text{Ar}_6$  represents the  $(\text{H}_2\text{O})_6^- \cdot \text{Ar}_m$  reactants responsible for the  $\text{ROH} \cdot (\text{H}_2\text{O})_6^-$  production, considering the fact that an average of 6Ar atoms are evaporatively lost in the  $(\text{H}_2\text{O})_6^- \cdot \text{Ar}_m + \text{D}_2\text{O}$  condensation process.<sup>15</sup> As the  $(\text{H}_2\text{O})_6^- \cdot \text{Ar}_6$  spectra exhibit no spectral band ascribable to type II isomers, it can be said that  $(\text{H}_2\text{O})_6^- \cdot \text{Ar}_6$  reactants are prepared initially in type-I isomeric form. The spectral features of the  $\text{ROH} \cdot (\text{H}_2\text{O})_6^-$  products bear a strong resemblance to those of  $(\text{H}_2\text{O})_7^-$  except that in the  $\text{D}_2\text{O} \cdot (\text{H}_2\text{O})_6^-$  spectrum a shoulder is discernible at the high-energy side of the main band, as marked with an arrow in Figure 2.2. The resemblance among those spectral features leads us straightforwardly to infer that  $\text{ROH} \cdot (\text{H}_2\text{O})_6^-$  binds an excess electron by the same mechanism as  $(\text{H}_2\text{O})_7^-$  does. This means that  $(\text{H}_2\text{O})_7^-$  and  $\text{ROH} \cdot (\text{H}_2\text{O})_6^-$  have an identical H-bond network structure responsible for the excess electron binding. With this in mind, by referring to the spectral assignments for  $(\text{H}_2\text{O})_7^-$  in previous studies,<sup>5,6</sup> we have interpreted the band features of  $\text{ROH} \cdot (\text{H}_2\text{O})_6^-$  as follows. The main band located at  $\approx 0.5$  eV is assignable to the electron detachment from an isomeric form of  $\text{ROH} \cdot (\text{H}_2\text{O})_6^-$ , where the excess electron is trapped mainly by a single water molecule located at the double hydrogen-bond acceptor (AA) site of the H-bond network, as is the case with the higher electron-binding isomer (type I) of  $(\text{H}_2\text{O})_7^-$ .<sup>6</sup> A small hump located around 1.0 eV arises from the transition to the vibrational excited

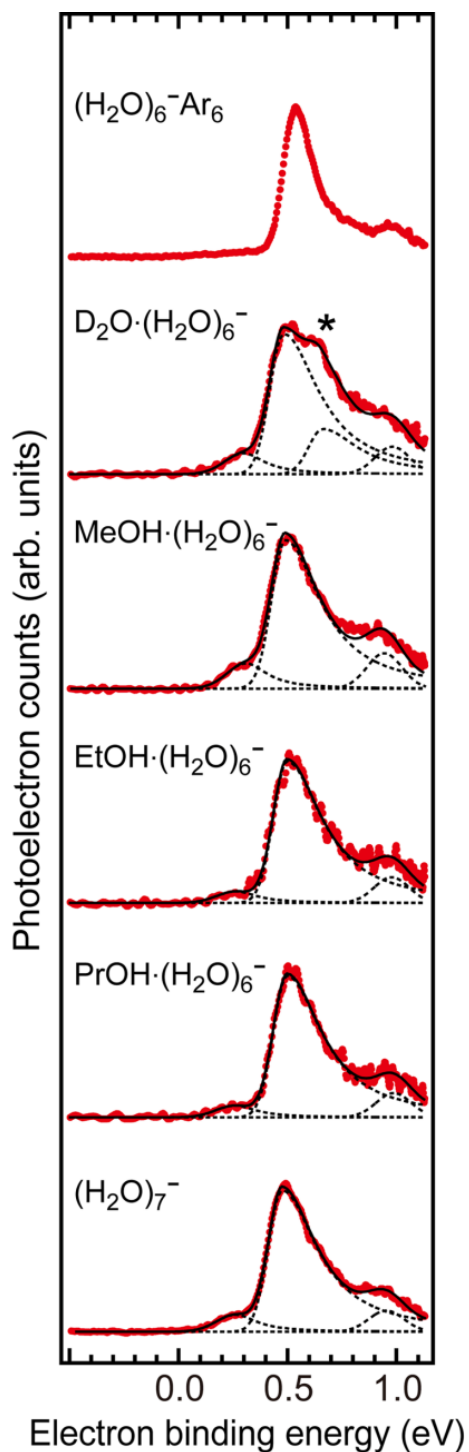


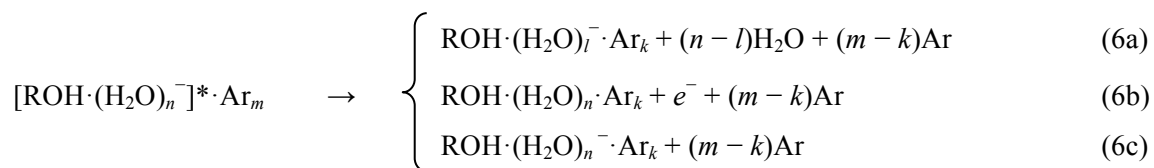
**Figure 2.2** Photoelectron spectra of  $(\text{H}_2\text{O})_6^- \text{Ar}_6$  reactant (top trace),  $\text{ROH} \cdot (\text{H}_2\text{O})_6^-$  products, and preexisting  $(\text{H}_2\text{O})_7^-$  (bottom trace) recorded at 1064 nm. Experimental data are plotted in red. Decomposed band shapes obtained in the band envelop analysis are shown with dotted lines; calculated band envelopes are shown with solid lines. Type I' components appearing in the  $\text{D}_2\text{O} \cdot (\text{H}_2\text{O})_6^-$  spectrum is marked with an asterisk.

state of the neutral manifold.<sup>5</sup> Another small hump at  $\approx 0.3$  eV is ascribable to the detachment from a lower electron-binding isomer of  $\text{ROH}\cdot(\text{H}_2\text{O})_6^-$ . As to this isomeric form, we can expect that multiple dangling H atoms at different sites of the H-bond network cooperatively bind the excess electron in the same manner as type II isomer of  $(\text{H}_2\text{O})_7^-$ .<sup>6</sup> In these situations, it seems rather appropriate to use the terms “type I” and “type II”, which are conventionally used to label the isomers of pure water cluster anions, loosely to denote the two isomeric forms of  $\text{ROH}\cdot(\text{H}_2\text{O})_6^-$ . The shoulder observed in the  $\text{D}_2\text{O}\cdot(\text{H}_2\text{O})_6^-$  spectrum is assigned unambiguously to type I' isomer of the water hexamer anion.

Isomer populations in  $\text{ROH}\cdot(\text{H}_2\text{O})_6^-$  were estimated from the photoelectron band intensities by using a band envelop analysis.<sup>5</sup> The analysis provided us with a set of quantities characterizing each photoelectron band, such as vertical detachment energy (VDE), band width, and relative band intensity, which are listed in Table 2.1. As is obvious from Table 2.1, the VDEs and the band widths take values almost same for all  $\text{ROH}\cdot(\text{H}_2\text{O})_6^-$  and  $\text{D}_2\text{O}\cdot(\text{H}_2\text{O})_6^-$ , whereas the isomer distributions show substituent dependence in that the population of type II isomer is significantly decreased in  $\text{EtOH}\cdot(\text{H}_2\text{O})_6^-$  and  $2\text{-PrOH}\cdot(\text{H}_2\text{O})_6^-$ . In view of the fact that the reactant  $(\text{H}_2\text{O})_6^- \cdot \text{Ar}_6$  anions were formed initially as type I isomer in the reactant beam, the emergence of type II in the product  $\text{ROH}\cdot(\text{H}_2\text{O})_6^-$  anions eventually indicates that a portion of  $\text{ROH}\cdot(\text{H}_2\text{O})_6^-$  anions undergo type I  $\rightarrow$  type II isomerization during the association process. The decrease in type-II population in  $\text{EtOH}\cdot(\text{H}_2\text{O})_6^-$  and  $2\text{-PrOH}\cdot(\text{H}_2\text{O})_6^-$  implies that the isomerization process is suppressed to some extent in those product anions.

### 2.3.3 Incorporation mechanism

As described above, the incorporation experiment was conducted in an ionized free jet containing reactant  $(\text{H}_2\text{O})_n^- \cdot \text{Ar}_m$  species. Product anions of process (4),  $\text{ROH}\cdot(\text{H}_2\text{O})_6^- \cdot \text{Ar}_k$ , were formed also in the free jet through the ROH entrainment. Low-energy collision conditions achieved by the beam-entrainment procedure<sup>24</sup> confer a significant advantage on the present experimental method, whereas the potential disadvantage of the method is a difficulty encountered in establishing rigorous one-to-one correspondence between the reactant and product species. Hence, the size preservation of the water cluster anions during the Ar-mediated process (eq. 4) is a key to the present study. As for the possible decay channels of  $[\text{ROH}\cdot(\text{H}_2\text{O})_n^-]^* \cdot \text{Ar}_m$  formed in the Ar-mediated process, one can raise the following pathways:



These decay processes are categorized as water-network degradation (6a), thermionic electron

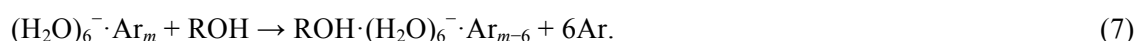
**Table 2.1** Vertical Detachment Energies (VDEs), Band Widths and Relative Band Intensities Determined from Photoelectron Spectra of  $\text{ROH}\cdot(\text{H}_2\text{O})_6^-$ 

Species	VDE (eV) <sup>a</sup>	Intensity <sup>b</sup>
$\text{D}_2\text{O}\cdot(\text{H}_2\text{O})_6^-$	0.30	0.08
	0.48	0.72
	0.66 <sup>c</sup>	0.20 <sup>c</sup>
$\text{CH}_3\text{OH}\cdot(\text{H}_2\text{O})_6^-$	0.31	0.11
	0.49	0.89
$\text{C}_2\text{H}_5\text{OH}\cdot(\text{H}_2\text{O})_6^-$	0.26	0.06
	0.50	0.94
$2\text{-C}_3\text{H}_7\text{OH}\cdot(\text{H}_2\text{O})_6^-$	0.26	0.06
	0.50	0.94
$(\text{H}_2\text{O})_7^-$	0.26	0.08
	0.48	0.92

<sup>a</sup>Uncertainty assessed to each VDE value is  $\pm 0.02$  eV. <sup>b</sup>Relative band intensities of type I (high-binding isomer) and type II (low-binding isomer) components. The Uncertainty assessed to each value is  $\pm 0.01$ . The band intensities are determined with the parameters for the bandwidth of  $0.27 \pm 0.01$  eV for type I and  $0.22 \pm 0.01$  eV for type II in the band envelope analysis. <sup>c</sup>VDE and relative intensity for the band assigned to type I'.

emission (6b) and evaporative cooling (6c), respectively. Process (6a) is the most energy-demanding process, where the amount of excess energy required for the reaction is that for breaking hydrogen bonds to evaporate one  $\text{H}_2\text{O}$  molecule from  $(\text{H}_2\text{O})_n^-$  ( $\approx 10$  kcal mol<sup>-1</sup>).<sup>25,26</sup> A less amount of excess energy is needed for process (6b). The adiabatic electron affinity (AEA) of type I form of  $(\text{H}_2\text{O})_n^-$  is estimated to lie in the range 0.12 – 0.23 eV (2.8 – 5.3 kcal mol<sup>-1</sup>).<sup>27,28</sup> Process (6c) is the least-energy demanding channel among the decay processes because the binding energy of one Ar atom to  $(\text{H}_2\text{O})_n^-$  is  $\approx 1.3$  kcal mol<sup>-1</sup>.<sup>15</sup> On the other hand, the excess energy imparted to nascent  $[\text{ROH}\cdot(\text{H}_2\text{O})_n^-] \cdot \text{Ar}_m$  species by the collisional incorporation is of the same amount as the association energy between  $(\text{H}_2\text{O})_n^-$  and ROH, or slightly larger than that by taking into account the relative kinetic energy between  $(\text{H}_2\text{O})_n^- \cdot \text{Ar}_m$  and ROH. The available excess energy of the reaction is comparable in magnitude to –or even larger than– the amount of energy required for processes (6a). Only from the viewpoint of reaction energy, it is inferred that all the decay channels, processes (6a) – (6c), could occur competitively in the  $(\text{H}_2\text{O})_6^- \cdot \text{Ar}_m + \text{ROH}$  reaction. However, the absence of  $\text{ROH}\cdot(\text{H}_2\text{O})_5^-$

species in the product mass spectra (Figs. 2.1(b) – (e)) evidently indicates a negligible contribution of process (6a) to the  $[\text{ROH}\cdot(\text{H}_2\text{O})_6^-]^*\cdot\text{Ar}_m$  decay process. Also, we take again particular note of the fact revealed by Johnson et al. that, in the binary  $(\text{H}_2\text{O})_n^-\cdot\text{Ar}_m + \text{D}_2\text{O}$  collision, the associative detachment channel is dramatically suppressed by rapid quenching of  $[\text{D}_2\text{O}\cdot(\text{H}_2\text{O})_{n+1}^-]^*\cdot\text{Ar}_m$  through sequential Ar evaporation, and that  $(\text{H}_2\text{O})_6^-\cdot\text{Ar}_{12} + \text{D}_2\text{O} \rightarrow \text{D}_2\text{O}\cdot(\text{H}_2\text{O})_6^-\cdot\text{Ar}_6 + 6\text{Ar}$  is the dominant pathway for the production of  $\text{D}_2\text{O}\cdot(\text{H}_2\text{O})_6^-\cdot\text{Ar}_6$ .<sup>15</sup> This is reasonably interpreted by the general truth that less energy-demanding reaction proceeds faster and more preferentially when the excess energy is dissipated through a statistical mechanism. In the present study, we thus expect the  $(\text{H}_2\text{O})_6^-\cdot\text{Ar}_m + \text{ROH}$  reaction to proceed primarily as



As revealed by the photoelectron spectroscopic measurement, the incorporation product,  $\text{ROH}\cdot(\text{H}_2\text{O})_6^-$ , is formed predominately in an isomeric form of type-I. We performed geometry optimization for type I structures of  $\text{MeOH}\cdot(\text{H}_2\text{O})_6^-$  to learn which cite of the H-bond network can be occupied by MeOH in the incorporation process. In the geometry optimization we chose two “open-prism” configurations predicted by Kim et al.<sup>29</sup> and by Jordan et al.,<sup>6</sup> more specifically the type-I framework of  $(\text{H}_2\text{O})_7^-$  denoted as Pf23a and Pf24a in References 6 and 29, as templates for constructing initial geometries for optimization. The initial geometries were prepared by replacing each  $\text{H}_2\text{O}$  located at possible SIHB sites of Pf23a/Pf24a with MeOH. Figure 2.3 displays stable geometries for  $\text{MeOH}\cdot(\text{H}_2\text{O})_6^-$  optimized by MP2/aug-cc-pVDZ+diff calculations (See Appendix for computational details.) It should be noted that the optimization with initial geometries having MeOH at the SIHB site adjacent to the electron-binding  $\text{H}_2\text{O}$  molecule eventually gave no local-minimum structures. Both in the stable geometries, **1** and **2**, MeOH is apt to occupy an AD (A = H-bond acceptor, D = H-bond donor) site. Isomer **2** is located 80 meV higher above isomer **1** in the calculated MP2 energy. The calculated VDEs are 0.44 and 0.48 eV for isomer **1** and **2**, respectively, which are in fair agreement with those determined experimentally (Table 2.1). The purpose of the present calculations is to show the existence of possible structures of  $\text{MeOH}\cdot(\text{H}_2\text{O})_6^-$  which retain the original H-bonding framework of  $(\text{H}_2\text{O})_7^-$ ; no effort has been made further to explore all the local-minimum structures and/or the global-minimum structure of  $\text{MeOH}\cdot(\text{H}_2\text{O})_6^-$ . The calculations, however, serve a useful purpose of discussing the incorporation mechanism at play in collisional reactions between  $(\text{H}_2\text{O})_6^-$  and ROH.

To summarize what we found in the present experiment, (1) Ar-medicated reactions of  $(\text{H}_2\text{O})_6^-\cdot\text{Ar}_m$  with ROH result in the formation of  $\text{ROH}\cdot(\text{H}_2\text{O})_6^-\cdot\text{Ar}_k$  with cross sections of almost the same size as in the reaction with  $\text{D}_2\text{O}$ , and (2) a portion of the  $\text{ROH}\cdot(\text{H}_2\text{O})_6^-$  products undergo type I  $\rightarrow$  type II interconversion as is the case in  $\text{D}_2\text{O}\cdot(\text{H}_2\text{O})_6^-$ ; a large substituent such as  $\text{C}_2\text{H}_5$  and  $\text{C}_3\text{H}_7$

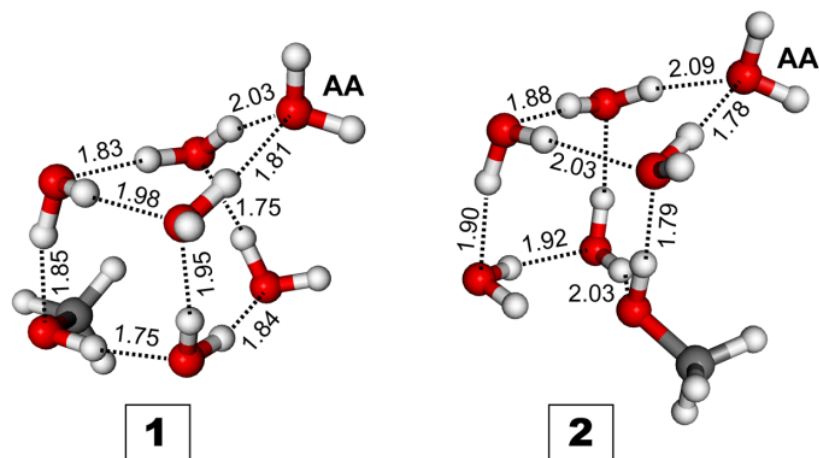


**Figure 2.3** Optimized geometries of  $\text{MeOH}\cdot(\text{H}_2\text{O})_6^-$  isomers at MP2/aug-cc-pVDZ+diff. The notation AA indicates the electron-binding site in a double H-bond acceptor configuration. Distances are given in angstroms.

can cause suppression of the interconversion. Finding (1) indicates that an ROH molecule is incorporated into the H-bond network of  $(\text{H}_2\text{O})_6^-$  in the same manner as the growth-by-condensation process,  $(\text{H}_2\text{O})_6^- + \text{H}_2\text{O} \rightarrow (\text{H}_2\text{O})_7^-$ . This also means that, in both the ROH incorporation and the growth-by-condensation, the process starts with a molecular uptake at the close vicinity of the sites where the incoming molecule can consequently occupy a single H-bond donor site at least in the early stage of the reaction. The observed substituent dependence – or rather its absence – leads us to infer that the pregnable sites are located away from the electron-binding AA site so that the bulky substituent could not overlap sterically with the diffuse electron. It can be said from finding (2) that the amount of energy imparted by the association provokes a rearrangement of the H-bond network, involving type I  $\rightarrow$  type II interconversion, in parallel with the Ar-evaporative cooling process. The smaller populations of type II isomers observed in  $\text{EtOH}\cdot(\text{H}_2\text{O})_6^-$  and  $2\text{-PrOH}\cdot(\text{H}_2\text{O})_6^-$  are reasonably interpreted either by a steric hindrance to isomerization or by increasing internal degrees of freedom for energy dissipation.

Within the context of above arguments, we can illustrate an incorporation scheme as shown in Figure 2.4. Assuming here that  $(\text{H}_2\text{O})_6^-$  takes on an “armchair”<sup>8,30</sup> configuration of type I isomer, one can find at least two possible ways to approach the pregnable site where the attack of ROH eventually leads to the formation of  $\text{ROH}\cdot(\text{H}_2\text{O})_6^-$  configurations displayed in Figure 2.3. Although the scheme is rather naïve in the interpretation of the present results, it still deserves a target for comparison with arguments in previous studies. In the  $(\text{H}_2\text{O})_6^- \cdot \text{Ar}_m + \text{D}_2\text{O}$  experiment, Johnson et al. found the

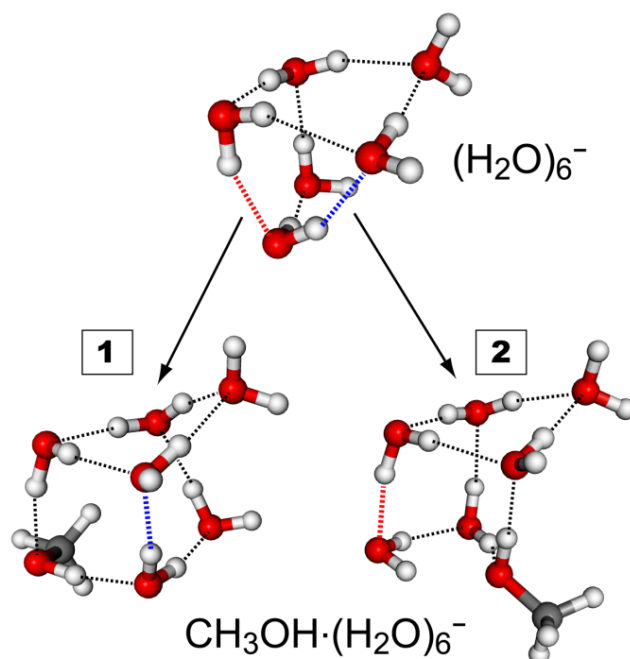


**Figure 2.4** A schematic of MeOH incorporation into  $(\text{H}_2\text{O})_6^-$ . Here,  $(\text{H}_2\text{O})_6^-$  is assumed to take on the H-bond network configuration referred to as 6Af, which was originally identified by Kim et al. (ref. 30). The figure is illustrative only for suggesting the possibility that MeOH insertion into the  $(\text{H}_2\text{O})_6^-$  network by breaking the red-colored (blue-colored) H-bond leads to the formation of  $\text{MeOH}\cdot(\text{H}_2\text{O})_6^-$  in isomeric form **1** (isomeric form **2**) without a rigorous network rearrangement.

incorporated  $\text{D}_2\text{O}$  to displace even the molecule in the AA electron-binding site.<sup>15,16</sup> They pointed out the possibility of displacement by direct collisional impact of  $\text{D}_2\text{O}$  at the AA site as well as thermal rearrangement of the H-bond network after incorporation.<sup>13,15</sup> On the basis of the present results, we infer that the direct collisional impact at the electron-binding site, if it occurs, makes a minor contribution to the growth-by-condensation of  $(\text{H}_2\text{O})_6^-$ , and that the displacement at the AA site results mainly from the subsequent thermal rearrangement.

## 2.4 Conclusions

The reactions between Ar-solvated water hexamer anion,  $(\text{H}_2\text{O})_6^- \cdot \text{Ar}_m$ , and ROH (R =  $\text{CH}_3$ ,  $\text{C}_2\text{H}_5$ , 2- $\text{C}_3\text{H}_7$ ) are observed to proceed as Ar-mediated association,  $(\text{H}_2\text{O})_6^- \cdot \text{Ar}_m + \text{ROH} \rightarrow \text{ROH}\cdot(\text{H}_2\text{O})_6^- \cdot \text{Ar}_k + (m - k)\text{Ar}$ , where the  $\text{ROH}\cdot(\text{H}_2\text{O})_6^- \cdot \text{Ar}_k$  products efficiently survive autodetachment and/or H-bond network degradation with a rapid energy dissipation through Ar



evaporation. We have found that relative cross sections for the  $\text{ROH}\cdot(\text{H}_2\text{O})_6^- \cdot \text{Ar}_k$  production are about the same size as that in the growth-by-condensation reaction,  $(\text{H}_2\text{O})_6^- \cdot \text{Ar}_m + \text{D}_2\text{O} \rightarrow \text{D}_2\text{O}\cdot(\text{H}_2\text{O})_6^- \cdot \text{Ar}_k + (m - k)\text{Ar}$ , when  $\text{R} = \text{CH}_3$  and  $\text{C}_2\text{H}_5$ , while slightly smaller when  $\text{R} = n\text{-C}_3\text{H}_7$ . It is also found that a portion of the product  $\text{ROH}\cdot(\text{H}_2\text{O})_6^-$  undergoes type I  $\rightarrow$  type II interconversion, which is thermally induced by the excess energy of reaction, during the association process. The fraction of type-II isomer in  $\text{ROH}\cdot(\text{H}_2\text{O})_6^-$  lies in the range 0.06 – 0.11, which is almost equal to the type-II fraction in  $\text{D}_2\text{O}\cdot(\text{H}_2\text{O})_6^-$  formed via the growth-by-condensation. From these findings we conclude that an ROH molecule, despite the lack of ability to take a DIHB configuration, is incorporated into  $(\text{H}_2\text{O})_6^-$  overall in the same manner as in the homogeneous growth-by-condensation of  $(\text{H}_2\text{O})_6^-$ . Substitution of a bulky alkyl group for one of the H atoms of the incoming water molecule scarcely modifies the entrance valley of the potential energy landscape relevant to the growth-by-condensation; it suppresses the subsequent occurrence of H-bond network rearrangement to some extent. The present study gives us a rough idea of the growth mechanism of water cluster anions, which now awaits consideration by more sophisticated molecular dynamics calculations.

## References

- 1 Haberland, H.; Ludewigt, C.; Schindler, H. G.; Worsnop, D. R. *J. Chem. Phys.* **1984**, *81*, 3742–3744.
- 2 Coe, J. V.; Lee, G. H.; Eaton, J. G.; Arnold, S. T.; Sarkas, H. W.; Bowen, K. H.; Ludewigt, C.; Haberland, H.; Worsnop, D. R. *J. Chem. Phys.* **1990**, *92*, 3980–3982.
- 3 Kim, J.; Becker, I.; Cheshnovsky, O.; Johnson, M. A. *Chem. Phys. Lett.* **1998**, *297*, 90–96.
- 4 Verlet, J.; Bragg, A. E.; Kammrath, A.; Cheshnovsky, O.; Neumark, D. M. *Science* **2005**, *307*, 93–96.
- 5 Coe, J. V.; Arnold, S. T.; Eaton, J. G.; Lee, G. H.; Bowen, K. H. *J. Chem. Phys.* **2006**, *125*, 014315.
- 6 Roscioli, J. R.; Hammer, N. I.; Johnson, M. A.; Diri, K.; Jordan, K. D. *J. Chem. Phys.* **2008**, *128*, 104314.
- 7 Hammer, N. I.; Shin, J.-W.; Headrick, J. M.; Diken, E. G.; Roscioli, J. R.; Weddle, G. H.; Johnson, M. A. *Science* **2004**, *306*, 675–679.
- 8 Hammer, N. I.; Roscioli, J. R.; Johnson, M. A. *J. Phys. Chem. A* **2005**, *109*, 7896–7901.
- 9 Hammer, N. I.; Roscioli, J. R.; Johnson, M. A.; Myshakin, E. M.; Jordan, K. D. *J. Phys. Chem. A* **2005**, *109*, 11526–11530.
- 10 Hammer, N. I.; Roscioli, J. R.; Bopp, J. C.; Headrick, J. M.; Johnson, M. A. *J. Chem. Phys.* **2005**, *123*, 244311.
- 11 Roscioli, J. R.; Hammer, N. I.; Johnson, M. A. *J. Phys. Chem. A* **2006**, *110*, 7517–7520.
- 12 Roscioli, J. R.; Johnson, M. A. *J. Chem. Phys.* **2007**, *126*, 024307.
- 13 McCunn, L. R.; Gardenier, G. H.; Guasco, T. L.; Elliott, B. M.; Bopp, J. C.; Relph, R. A.; Johnson, M. A. *J. Chem. Phys.* **2008**, *128*, 234311.
- 14 Campagnola, P. J.; Cyr, D. M.; Johnson, M. A. *Chem. Phys. Lett.* **1991**, *181*, 206–212.
- 15 McCunn, L. R.; Headrick, J. M.; Johnson, M. A. *Phys. Chem. Chem. Phys.* **2008**, *10*, 3118–3123.
- 16 Guasco, T. L.; Elliott, B. M.; Johnson, M. A.; Ding, J.; Jordan, K. D. *J. Phys. Chem. Lett.* **2010**, *1*, 2396–2401.
- 17 Nakanishi, R.; Muraoka, A.; Nagata, T. *Chem. Phys. Lett.* **2006**, *427*, 56–61.
- 18 Tsukuda, T.; Saeki, M.; Iwata, S.; Nagata, T. *J. Phys. Chem. A* **1997**, *101*, 5103–5110.
- 19 Eppink, A. T. J. B.; Parker, D. H. *Rev. Sci. Instrum.* **1997**, *68*, 3477–3484.
- 20 Dribinski, V.; Ossadtchi, A.; Mandelshtam, V. A.; Reisler, H. *Rev. Sci. Instrum.* **2002**, *73*, 2634–2642.
- 21 Travers, M. J.; Cowles, D. C.; Ellison, G. B. *Chem. Phys. Lett.* **1989**, *164*, 449–455.
- 22 Arnold, D. W.; Bradforth, S. E.; Kim, E. H.; Neumark, D. M. *J. Chem. Phys.* **1995**, *102*, 3510–3518.

- 23 Lee, H. M.; Suh, S. B.; Tarakeshwar, P.; Kim, K. S. *J. Chem. Phys.* **2005**, *122*, 044309.
- 24 Arnold, S. T.; Morris, R. A.; Viggiano, A. A.; Johnson, M. A. *J. Phys. Chem.* **1996**, *100*, 2900–2906.
- 25 Klots, C. E. Evaporative Cooling. *J. Chem. Phys.* **1985**, *83*, 5854–5860.
- 26 Campagnola, P. J.; Posey, L. A.; Johnson, M. A. *J. Chem. Phys.* **1991**, *95*, 7998–8004.
- 27 Arnold, S. T.; Morris, R. A.; Viggiano, A. A. *J. Chem. Phys.* **1995**, *103*, 9242–9248.
- 28 Elliot, B. M.; McCunn, L. R.; Johnson, M. A. *Chem. Phys. Lett.* **2008**, *467*, 32–36.
- 29 Lee, H. M.; Suh, S. B.; Kim, K. S. *J. Chem. Phys.* **2003**, *118*, 9981–9986.
- 30 Lee, H. M.; Lee, S.; Kim, K. S. *J. Chem. Phys.* **2003**, *119*, 187–194.

## Supplemental material for Chapter 2

### S2.1 Computational details

The geometry optimization for  $\text{MeOH}\cdot(\text{H}_2\text{O})_6^-$  was done by the second-order Møller-Plesset perturbation (MP2) method implemented in the Gaussian 03 program package.<sup>1</sup> We employed Dunning's aug-cc-pVDZ basis set<sup>2,3</sup> with additional diffuse functions for oxygen and hydrogen atoms (denoted aug-cc-pVDZ+diff) having exponents of  $9.87\times 10^{-3}$  au for O(s),  $8.57\times 10^{-3}$  for O(p), and  $3.72\times 10^{-3}$  for H(s).

As mentioned in the main text, the calculations aimed at demonstrating the existence of stable structures of  $\text{MeOH}\cdot(\text{H}_2\text{O})_6^-$ , while not exploring all the possible local-minimum structures for the global minimum. For this purpose, we used known structures of  $(\text{H}_2\text{O})_7^-$  as a template for the initial geometries of  $\text{MeOH}\cdot(\text{H}_2\text{O})_6^-$  in the optimization. The  $(\text{H}_2\text{O})_7^-$  structures denoted as Pf23a/Pf24a (“prism structure having a partly free water monomer” with AA-configuration)<sup>4,5</sup> were employed as the templates (Figure S1). The initial geometries were prepared by replacing one of  $\text{H}_2\text{O}$  molecules located at the SIHB sites of Pf23a/Pf24a with MeOH. The optimization procedure gave at least five tentative geometries, two of which were finally confirmed as local-minimum structures of  $\text{MeOH}\cdot(\text{H}_2\text{O})_6^-$  by subsequent vibrational frequency analysis. These two structures are displayed in Figure 2.3 in the main text as isomers **1** and **2**. The geometrical parameters for isomers **1** and **2** are given in Tables S1 and S2, respectively, as their x, y, z-coordinates in the “standard orientation” of the Gaussian 03 package. Their MP2 energies and VDEs are listed in Table S3.

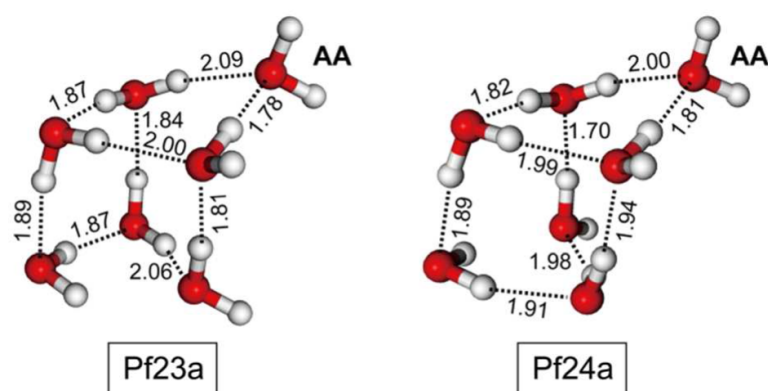


**Figure S1.** Pf23a and Pf24a structures of  $(\text{H}_2\text{O})_7^-$  optimized at the MP2/ aug-cc-pVDZ+diff level. They serve not only as templates for the initial geometries but also as references to compare with the optimized  $\text{MeOH}\cdot(\text{H}_2\text{O})_6^-$  structures (see Tables S1 and S2). The symbol AA indicates the electron-binding site in a double H-bond acceptor configuration. Distances are given in angstroms.

Table S1. MP2 geometry for isomer 1 of  $MeOH \cdot (H_2O)_6^-$ 

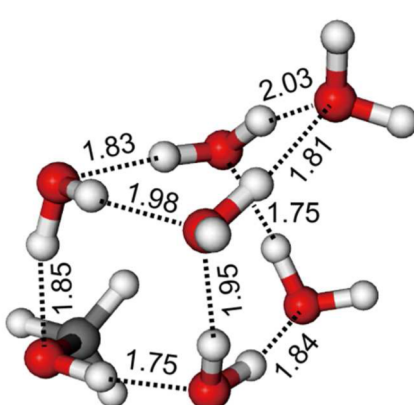
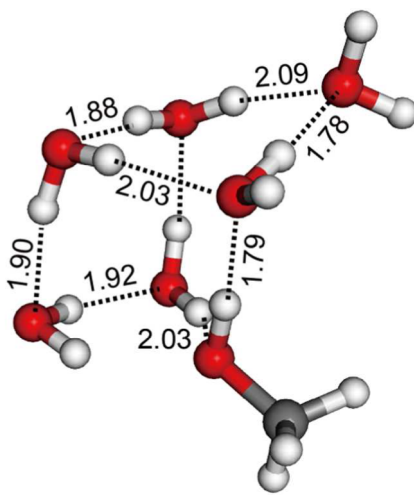
Structure	Coordinates (Angstroms)			
	x	y	z	
	O	0.261457	-1.649454	-1.292549
	H	1.129106	-1.511809	-0.853469
	H	-0.333282	-1.864739	-0.551399
	O	-1.549282	-1.517060	0.977839
	H	-2.062520	-2.127326	1.524446
	H	-2.229937	-0.913393	0.600964
	O	-3.318188	0.252401	-0.257650
	H	-4.084699	-0.176100	-0.683165
	H	-3.745908	0.882619	0.353851
	O	-0.761602	0.947552	-1.571321
	H	-1.698252	0.806403	-1.345769
	H	-0.387073	0.036561	-1.571481
	O	0.207937	2.355864	0.561828
	H	-0.534686	2.891243	0.870437
	H	-0.144534	1.898708	-0.243827
	O	2.573631	-0.855042	0.091745
	C	2.892968	0.364142	-0.594696
	H	1.984600	-0.600495	0.844243
	H	3.596122	0.110001	-1.400391
	H	3.372589	1.091536	0.081285
H	1.998177	0.832926	-1.037386	
O	0.748728	-0.019803	1.945289	
H	0.543762	0.870631	1.585079	
H	-0.062727	-0.527284	1.753307	

Table S2. MP2 geometry for isomer 2 of  $\text{MeOH}\cdot(\text{H}_2\text{O})_6^-$ 

Structure	Coordinates (Angstroms)			
	x	y	z	
	O	-0.644186	-1.667441	1.642754
	H	0.307379	-1.773927	1.429946
	H	-0.731400	-0.711716	1.803075
	O	-0.852590	1.252138	1.340197
	H	-1.052629	1.990166	1.934889
	H	-1.584471	1.285937	0.677939
	O	-2.862205	1.197958	-0.550460
	H	-3.725251	1.359911	-0.125364
	H	-2.785844	1.952548	-1.164092
	O	-1.673871	-1.553963	-1.000458
	H	-2.193848	-0.733155	-0.993728
	H	-1.424316	-1.679739	-0.058880
	O	0.977618	-1.163875	-1.853254
	H	1.124189	-0.280208	-1.470840
	H	0.018862	-1.311222	-1.692761
	O	2.056876	-1.748689	0.700574
	C	1.759035	-1.820374	-0.232215
	H	2.229128	-0.793105	0.750880
	H	1.554257	1.065001	-0.007692
	H	2.05195	2.363517	-0.357148
H	0.710627	1.192804	0.481180	
O	2.968501	2.212372	-0.943972	
H	2.297088	2.956081	0.540410	
H	1.324051	2.923484	-0.966855	

**Table S3.** MP2 energies for  $\text{MeOH}\cdot(\text{H}_2\text{O})_6^-$  isomers

Energy	Configuration	
	1	2
$E$ (Hartree)	-573.0852837	-573.0824520
$\Delta E$ (meV) <sup>a</sup>	0	77.1
VDE (meV)	436	478

<sup>a</sup> Energy difference,  $\Delta E$ , is evaluated with reference to the total energy of isomer **1**.

## S2.2 References

- 1 Frisch, M. J.; Trucks, G. W.; Schlegel, H. B.; Scuseria, G. E.; Robb, M. A.; Cheeseman, J. R.; Montgomery, Jr., J. A.; Vreven, T.; Kudin, K. N.; Burant, J. C.; et al. Gaussian 03, Revision C.02; Gaussian, Inc.: Wallingford CT, 2004.
- 2 Dunning, T. H., Jr. *J. Chem. Phys.* 1989, 90, 1007–1023.
- 3 Kendall, R. A., Dunning, T. H., Jr.; Harrison, R. J. *J. Chem. Phys.* 1992, 96, 6796–6806.
- 4 Lee, H. M.; Suh, S. B.; Kim, K. S. *J. Chem. Phys.* 2003, 118, 9981–9986.
- 5 Roscioli, J. R.; Hammer, N. I.; Johnson, M. A.; Diri, K.; Jordan, K. D. *J. Chem. Phys.* 2008, 128, 104314.





# Chapter 3

## Hydrogen-bond network transformation in water-cluster anions induced by the complex formation with benzene

### ABSTRACT

We report spectroscopic evidence of isomer interconversion in water cluster anions,  $(\text{H}_2\text{O})_n^-$ , which occurs through the interaction with a benzene molecule. An anion complex composed of  $(\text{H}_2\text{O})_6^-$  and benzene,  $\text{Bz}\cdot(\text{H}_2\text{O})_6^-$ , is formed via the reaction of  $(\text{H}_2\text{O})_6^- \text{Ar}_m$  with benzene. The reaction proceeds as an Ar-mediated association process such that a rapid energy dissipation by sequential Ar evaporation efficiently suppresses the thermionic emission of  $e^-$ ,  $\text{H}_2\text{O}$ , or both, giving rise to the formation of  $\text{Bz}\cdot(\text{H}_2\text{O})_6^-$ . Photoelectron spectroscopy is employed to probe the electronic properties of the anionic species, which reveals that “type I  $\rightarrow$  type II” isomer interconversion proceeds in the  $(\text{H}_2\text{O})_6^-$  moiety during the formation of  $\text{Bz}\cdot(\text{H}_2\text{O})_6^-$ . With the aid of ab initio calculations, we conclude that the interconversion is driven by preferential stabilization of the H-bond network of type II arrangement through the formation of a nonconventional  $\text{O}-\text{H}\cdots\pi$  hydrogen bond between  $(\text{H}_2\text{O})_6^-$  and Bz.

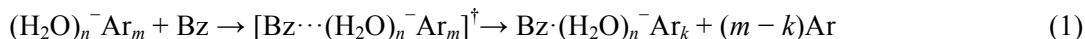
This chapter has been reproduced in part with permission from the following previously published article: Nakanishi, R; Sato, T.; Yagi, K; Nagata, T. *Journal of Physical Chemistry Letters*, 2012, 3 3571-3575. DOI: 10.1021/jz301599f Copyright 2012 American Chemical Society

### 3.1 Introduction

While a single water molecule does not possess any bound anionic form, aggregates of water molecules can bind an excess electron to form water cluster anions,  $(\text{H}_2\text{O})_n^-$ , in several distinct isomeric structures.<sup>1,2</sup> A series of IR spectroscopic studies by Johnson and his coworkers have unveiled the structural properties and electron binding mechanism of  $(\text{H}_2\text{O})_n^-$  in the small size regime  $n \leq 8$ , especially at  $n = 6$  and  $7$ .<sup>3-7</sup> According to the studies, two types of isomeric forms are distinguishable in  $(\text{H}_2\text{O})_{6,7}^-$  by their vibrational spectral patterns. Those isomeric forms are denoted as types I and II in decreasing order of their electron binding energies. A notable difference between I and II, aside from their structural difference, is that in the former the excess electron is trapped mainly by a single water molecule located at the double hydrogen-bond acceptor (AA) site of the H-bond network while in the latter multiple dangling H atoms at different sites of the network cooperatively binds the electron. There exists another type of isomeric form in  $(\text{H}_2\text{O})_7^-$  (type I') which also possesses the AA electron-binding motif while binds the diffuse electron more strongly than type I.<sup>6</sup> These isomeric forms are theoretically calculated to be close in energy and experimentally observed to coexist in a beam of  $(\text{H}_2\text{O})_n^-$  anions.<sup>4,6,8-19</sup>

This raises an obvious question regarding the structural dynamics in  $(\text{H}_2\text{O})_{6,7}^-$ : i.e., whether or not the isomeric forms can interconvert one another and, if so, how large is the relevant potential energy barrier between them. McCunn *et al.* carried out an experiment to probe the isomer interconversion in  $(\text{H}_2\text{O})_{6,7}^-$  by using IR spectroscopy combined with photoelectron spectroscopy.<sup>20</sup> They found that  $\text{I} \rightarrow \text{II}$  interconversion scarcely proceeded in vibrationally-excited  $(\text{H}_2\text{O})_6^-$  in the excitation energy range of  $\approx 0.4$  eV. They also observed that the vibrational excitation could induce  $\text{I}' \rightarrow \text{I}$  interconversion but neither  $\text{I} \rightarrow \text{II}$  nor  $\text{I}' \rightarrow \text{II}$  in  $(\text{H}_2\text{O})_7^-$ . In addition, as described in Chapter 2, only a small portion of  $(\text{H}_2\text{O})_6^-$  undergoes  $\text{I} \rightarrow \text{II}$  interconversion during the uptake of  $\text{D}_2\text{O}$  or alcohol molecules. Thus, type I isomers of  $(\text{H}_2\text{O})_{6,7}^-$  are rather robust and less subject to  $\text{I} \rightarrow \text{II}$  interconversion when they are internally excited.

Here, we design another type of experiment for exploring  $\text{I} \rightarrow \text{II}$  interconversion accompanied with a substantial H-bond network transformation in  $(\text{H}_2\text{O})_{6,7}^-$ . In the present study,  $(\text{H}_2\text{O})_{6,7}^-$  anions once prepared in type I structure are allowed to interact with benzene (Bz) to form  $\text{Bz} \cdot (\text{H}_2\text{O})_{6,7}^-$  complexes. While the H-bond networks of  $(\text{H}_2\text{O})_{6,7}^-$  do not incorporate Bz, they can interact with the aromatic molecule through the formation of a nonconventional  $\text{O}-\text{H} \cdots \pi$  hydrogen bond.<sup>21-25</sup> As the  $\text{O}-\text{H} \cdots \pi$  interaction is comparable in bond strength with  $\text{O}-\text{H} \cdots \text{O}$  interactions operative in the H-bond network, either deformation or transformation of the network is expected to occur in  $(\text{H}_2\text{O})_{6,7}^-$  through the interaction with Bz. This scenario was experimentally performed in an Ar-mediated association process:<sup>26</sup>



In process (1) the excess energy of reaction is rapidly dissipated as the evaporation energy of Ar atoms so that the product anions are efficiently quenched to possible local minima in the potential energy landscape relevant to the interconversion. More specifically, in the present experiment, Bz was entrained into a free jet containing  $(\text{H}_2\text{O})_n^-\text{Ar}_m$  anions; the product anions were mass-analyzed and their isomer populations were monitored by anion photoelectron spectroscopy.

## 3.2. Experimental

The  $(\text{H}_2\text{O})_n^-\text{Ar}_m$  reactants were prepared in an electron-impact ionized free jet.<sup>27</sup> An argon gas containing a trace amount of water ( $\approx 0.16\%$  by volume) was expanded through a pulsed nozzle at a stagnation pressure of  $\approx 0.4$  MPa. The free jet was then crossed with a 200-eV electron beam at the expansion region, where secondary slow electrons produced by the electron impact were captured by preexisting neutral  $(\text{H}_2\text{O})_N\text{Ar}_M$  clusters to form  $(\text{H}_2\text{O})_n^-\text{Ar}_m$ . Benzene was introduced through an effusive nozzle into the vacuum chamber;  $(\text{H}_2\text{O})_n^-\text{Ar}_m$  react with the entrained Bz while drifting in the source chamber. The product anions were extracted from the beam by applying a pulsed electric field, and mass-analyzed by a 1.9-m TOF mass spectrometer.

Photoelectron measurements were performed at 1064 nm by using a velocity-map imaging<sup>28</sup> photoelectron spectrometer equipped at the end of the TOF mass spectrometer.<sup>29</sup> The photoelectron images were acquired typically for 20000 – 60000 laser shots. Photoelectron spectra were reconstructed from the obtained images using the basis set expansion (BASEX) method.<sup>30</sup> The spectral resolution was  $\approx 40$  meV at the photoelectron kinetic energy of 500 meV after the reconstruction procedure. The measured electron kinetic energy was calibrated against the known photoelectron bands of  $\text{O}_2^-$ .<sup>31</sup> Quantum chemical calculations were performed with the Gaussian 03 package.<sup>32</sup>

## 3.3. Results and Discussion

Figure 3.1 displays the ion distributions before and after the entrainment of Bz molecules into the  $(\text{H}_2\text{O})_n^-\text{Ar}_m$  beam. The reactant ion distribution is characterized by an overwhelming abundance of the  $(\text{H}_2\text{O})_n^-\text{Ar}_m$  series with  $n = 6$  and 7, as well as by an almost-complete absence of the  $n \leq 5$  families (Fig. 3.1(a)). The  $n = 8 - 10$  series appear only as minor species, while a discernible amount of  $(\text{H}_2\text{O})_n^-\text{Ar}_m$  with  $n \geq 11$  are observed. When the Bz gas was entrained into the beam, all the  $(\text{H}_2\text{O})_n^-\text{Ar}_m$  peaks were decreased in intensity by  $\approx 50\%$  and product mass peaks emerged in the

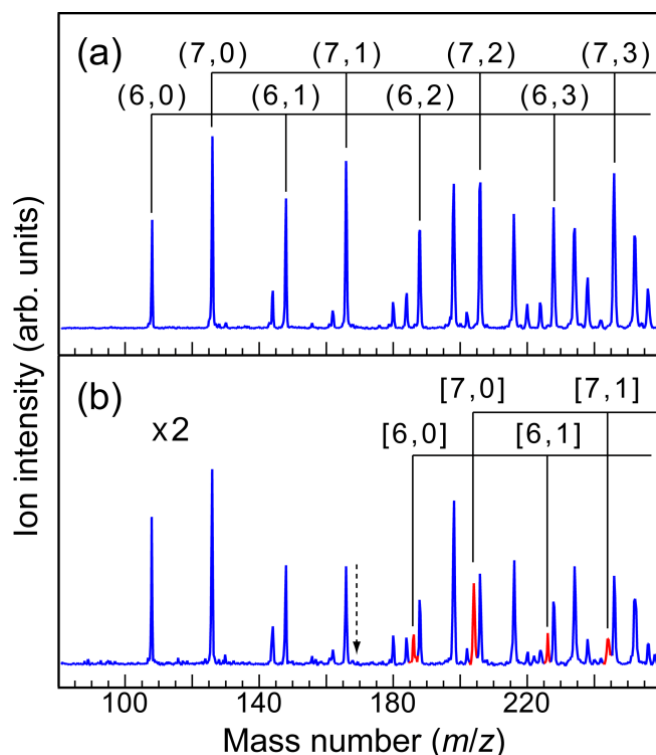


**Figure 3.1** Mass spectra of the  $(\text{H}_2\text{O})_n^- \text{Ar}_m$  reactants (a) and those after the reaction with Bz (b). The product  $[\text{Bz} \cdot (\text{H}_2\text{O})_n]^- \text{Ar}_k$  peaks, interspersed between the unreacted  $(\text{H}_2\text{O})_n^- \text{Ar}_m$  peaks, are indicated in red. Note that the vertical scale is expanded by a factor of 2 in trace (b). The formula  $(\text{H}_2\text{O})_n^- \text{Ar}_m$  is abbreviated as  $(n, m)$ , and  $[\text{Bz} \cdot (\text{H}_2\text{O})_n]^- \text{Ar}_k$  as  $[n, k]$  in the spectra. The dashed arrow indicates the position where  $[\text{Bz} \cdot (\text{H}_2\text{O})_5]^-$  peak would appear.

spectrum (Fig. 3.1(b)). These mass peaks are assigned to  $[\text{Bz} \cdot (\text{H}_2\text{O})_n]^- \text{Ar}_k$  ( $n = 6 - 10$ ,  $k = 0, 1$ ) according to their  $m/e$  values. The absence of  $[\text{Bz} \cdot (\text{H}_2\text{O})_n]^- \text{Ar}_k$  anions with  $n \leq 5$ , along with a tiny population for  $n = 8 - 10$ , is reminiscent of the characteristic features of the reactant  $(\text{H}_2\text{O})_n^- \text{Ar}_m$  distribution in the primary beam, reinforcing our claim that  $[\text{Bz} \cdot (\text{H}_2\text{O})_n]^- \text{Ar}_k$  are produced via the Ar-mediated association process where the preferential Ar-evaporation can efficiently suppress the loss of water molecules during the reaction. (See Appendix of this chapter for detailed discussion on the size preservation of the water cluster anions during the reaction.)

The electronic properties of the  $[\text{Bz} \cdot (\text{H}_2\text{O})_n]^- \text{Ar}_k$  products were probed by photoelectron spectroscopy. Figure 3.2 shows the photoelectron spectra of the dominant product anions,  $[\text{Bz} \cdot (\text{H}_2\text{O})_6]^-$  and  $[\text{Bz} \cdot (\text{H}_2\text{O})_7]^-$ , formed in process (1). The  $[\text{Bz} \cdot (\text{H}_2\text{O})_6]^-$  spectrum consists of two photoelectron bands comparable in band intensity. The band features are reasonably interpreted as the presence of two distinct isomeric forms rather than as the vibrational progressions in the neutral

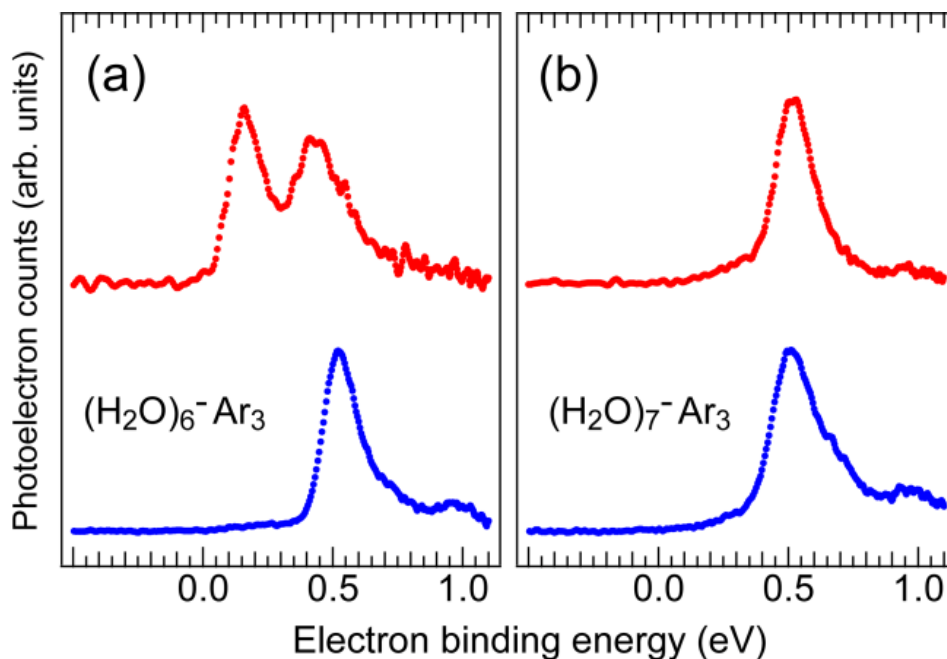


**Figure 3.2** Photoelectron spectra of  $[\text{Bz}\cdot(\text{H}_2\text{O})_6]^-$  (upper trace of panel (a)) and  $[\text{Bz}\cdot(\text{H}_2\text{O})_7]^-$  (upper trace of panel (b)) recorded at 1064 nm. The lower traces are the spectra of  $(\text{H}_2\text{O})_{6,7}^- \text{Ar}_3$  reactants measured under the same expansion conditions. The photoelectron counts are plotted against the electron binding energy,  $\epsilon_{\text{BE}}$ , defined as  $\epsilon_{\text{BE}} = h\nu - \epsilon_{\text{KE}}$ , where  $h\nu$  and  $\epsilon_{\text{KE}}$  represent the photon energy and the photoelectron kinetic energy, respectively.

manifold because the spectrum of  $[\text{Bz}\cdot\text{d}_6\cdot(\text{D}_2\text{O})_6]^-$  isotopomer shows no significant band shift. The VDE values for the two species determined from the band maxima are  $0.16 \pm 0.02$  and  $0.43 \pm 0.02$  eV, respectively. On the basis of the band positions and their separation of 0.27 eV, we identify the spectral carriers as two isomeric forms of the complex of  $(\text{H}_2\text{O})_6^-$  and Bz, where  $(\text{H}_2\text{O})_6^-$  interacts with Bz in a manner such that the  $(\text{H}_2\text{O})_6^-$  moiety retains the structural properties as type I (high-binding) or type II (low-binding) form of  $(\text{H}_2\text{O})_6^-$ . In contrast to  $[\text{Bz}\cdot(\text{H}_2\text{O})_6]^-$ , the  $[\text{Bz}\cdot(\text{H}_2\text{O})_7]^-$  spectrum is composed primarily of a single band, from which the VDE value is determined to be  $0.52 \pm 0.01$  eV. The  $[\text{Bz}\cdot(\text{H}_2\text{O})_7]^-$  photoelectron band is assignable unambiguously to the photodetachment from a  $\text{Bz}\cdot(\text{H}_2\text{O})_7^-$  complex containing  $(\text{H}_2\text{O})_7^-$  of type I as a substructure. Thus, the  $[\text{Bz}\cdot(\text{H}_2\text{O})_6]^-$  and  $[\text{Bz}\cdot(\text{H}_2\text{O})_7]^-$  product anions are both characterized as the association complex between  $(\text{H}_2\text{O})_n^-$  and Bz, represented hereafter as  $\text{Bz}\cdot(\text{H}_2\text{O})_6^-$  and  $\text{Bz}\cdot(\text{H}_2\text{O})_7^-$ , respectively.

In Fig. 3.2 also shown for comparison are the spectra of the  $(\text{H}_2\text{O})_{6,7}^- \text{Ar}_3$  reactants. As described below, the association energy between Bz and  $(\text{H}_2\text{O})_6^-$  is calculated to be in the range 3 – 4 kcal mol<sup>-1</sup>, depending on the isomeric forms of  $(\text{H}_2\text{O})_6^-$ . From this value the number of Ar atoms lost in process

(1) is roughly estimated to be 3, by considering the binding energy of Ar atom to  $(\text{H}_2\text{O})_6^-$  ( $\approx 1.3$  kcal mol $^{-1}$ )<sup>20</sup>. This estimate allows us to nominate  $(\text{H}_2\text{O})_{6,7}^-\text{Ar}_3$  as representatives of the  $(\text{H}_2\text{O})_{6,7}^-\text{Ar}_m$  reactants responsible for the  $\text{Bz}\cdot(\text{H}_2\text{O})_{6,7}^-$  production: hence, the  $(\text{H}_2\text{O})_{6,7}^-\text{Ar}_3$  spectra serve our purpose of evaluating the “initial” isomer distribution in the Ar-solvated  $(\text{H}_2\text{O})_{6,7}^-$  reactant anions. As the  $(\text{H}_2\text{O})_{6,7}^-\text{Ar}_3$  spectra exhibit no spectral band ascribable to type II isomer, it is safe to say that the  $(\text{H}_2\text{O})_{6,7}^-\text{Ar}_3$  reactants are prepared initially in type-I isomeric form. The comparison between the product and reactant spectra in Fig. 3.2 readily leads us to infer that (1) type I  $\rightarrow$  II interconversion occurs efficiently during the Ar-mediated association reaction between type I isomer of  $(\text{H}_2\text{O})_6^-$  with Bz, and that (2) the interconversion is almost inhibited in the  $(\text{H}_2\text{O})_7^-$  reaction. The present findings contrast starkly with the previous report by Johnson *et al.* that I  $\rightarrow$  II interconversion is driven neither in  $(\text{H}_2\text{O})_6^-$  nor in  $(\text{H}_2\text{O})_7^-$  by vibrational excitation.<sup>20</sup>

With this in mind, we focus our attention on the I  $\rightarrow$  II interconversion observed in the complex formation of  $\text{Bz}\cdot(\text{H}_2\text{O})_6^-$ . Our primary focus is on the energetics at play, especially the stabilization energy for each form of the  $(\text{H}_2\text{O})_6^-$  isomers, type I or II, through the interactions with Bz. To address this issue, we performed geometry optimization for the  $\text{Bz}\cdot(\text{H}_2\text{O})_6^-$  complex by starting with initial configurations constructed of either type I or type II form of  $(\text{H}_2\text{O})_6^-$  and neutral Bz. As for the type I hexamer, we chose the “armchair”-type configuration predicted by Kim and co-workers,<sup>13</sup> more specifically the  $(\text{H}_2\text{O})_6^-$  structure denoted as 6Af in Ref. 13. As for type II, the “book”-type configuration denoted as 6Bd<sup>13</sup> was chosen. Figure 3.3 displays two distinct geometries for  $\text{Bz}\cdot(\text{H}_2\text{O})_6^-$  optimized by MP2/aug-cc-pVDZ+diff calculations. Also shown in Fig. 3.3 are the  $(\text{H}_2\text{O})_6^-$  isomers with 6Af and 6Bd configurations optimized at the same level of theory. Isomer 6Af has an AA electron binding site characteristic of type I whereas 6Bd has five dangling hydrogen atoms, four of which collectively trap the diffuse electron with relatively lower binding energy (type II).<sup>4</sup> As seen in Fig. 3.3, the “armchair” framework is retained in configuration **A** as a substructure; however, the hydrogen-bond network is deformed due to the interaction with Bz in that the AD water, whose dangling hydrogen atom is originally pointed toward the excess electron in free  $(\text{H}_2\text{O})_6^-$ , now flips the H atom toward Bz as opposed to the electron. On the other hand, the “book” remains almost intact in configuration **B**. The CCSD(T) energies calculated for these two  $\text{Bz}\cdot(\text{H}_2\text{O})_6^-$  configurations are summarized in Table 3.1. The calculated VDEs are in fair agreement with the observed ones; based on this we treat **A** and **B** as the representatives of type I and II isomers of  $\text{Bz}\cdot(\text{H}_2\text{O})_6^-$  in further discussion. Among the quantities listed in Table 3.1, the difference in the total energy between configurations **A** and **B**,  $\Delta E_{\text{total}}$ , is of specific interest, which should be compared with that between 6Af and 6Bd isomers of  $(\text{H}_2\text{O})_6^-$  to assess the isomer-dependent stabilization by association with Bz. The  $\Delta E_{\text{total}}$  value is calculated to be 0.08 kcal·mol $^{-1}$  at CCSD(T)/aug-cc-pVDZ+diff//MP2/aug-cc-pVDZ+diff, and to be 0.36 kcal·mol $^{-1}$  after the corrections for basis set superposition error (BSSE)

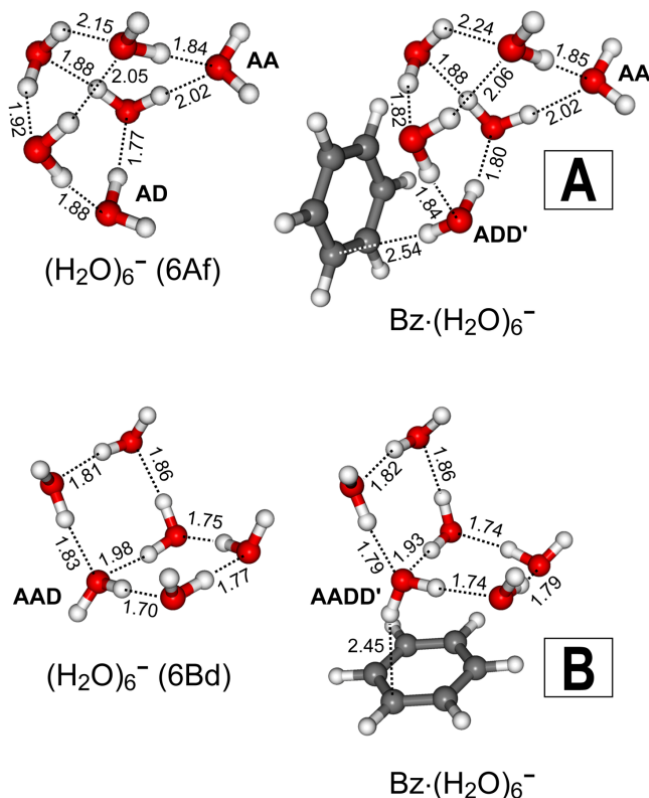


**Figure 3.3** Optimized geometries of  $(\text{H}_2\text{O})_6^-$  and  $\text{Bz}\cdot(\text{H}_2\text{O})_6^-$  isomers at MP2/aug-cc-pVDZ+diff. The hydrogen-bond network configurations, 6Af and 6Bd, were originally identified by Kim et al. (Ref. 13). Abbreviated notations are used for indicating specific sites of the network; AA: double H-bond acceptor site, AD: single acceptor/single donor site, AAD: double acceptor/single donor site, ADD: single acceptor/double donor site, AADD: double acceptor/double donor site. Distances are given in angstroms.

using the counterpoise (CP) procedure. The calculations also revealed that  $(\text{H}_2\text{O})_6^-$  in 6Bd configuration is located higher in energy by  $1.34 \text{ kcal}\cdot\text{mol}^{-1}$  with reference to that in 6Af. On the basis of these calculations, we infer that 6Bd configuration is stabilized more favorably than 6Af through the association with Bz. The net association energy between  $(\text{H}_2\text{O})_6^-$  and Bz, which is defined as the energy difference between  $\text{Bz}\cdot(\text{H}_2\text{O})_6^-$  and  $(\text{H}_2\text{O})_6^- + \text{Bz}$ , is expressed as  $E_{\text{asn}} = E_{\text{int}} + E_{\text{dfm}}$ , where  $E_{\text{int}}$  represents the interaction energy between the  $(\text{H}_2\text{O})_6^-$  and Bz moieties within the complex, and  $E_{\text{dfm}}$  is the energy associated with the structural deformation of  $(\text{H}_2\text{O})_6^-$  and Bz induced by complex formation. As  $E_{\text{dfm}}$  is smaller by  $0.43 \text{ kcal}\cdot\text{mol}^{-1}$  and  $E_{\text{int}}$  is larger in absolute magnitude by  $0.55 \text{ kcal}\cdot\text{mol}^{-1}$  in configuration **B** than in **A**, the net gain in  $E_{\text{asn}}$  is larger by  $0.98 \text{ kcal}\cdot\text{mol}^{-1}$  for configuration **B** (Table 3.1). By combining these energetics arguments with the experimental

**Table 3.1** Calculated energies for  $\text{Bz}\cdot(\text{H}_2\text{O})_6^-$  complexes<sup>a</sup>

$E^b$	configuration		$\Delta E$
	<b>A</b>	<b>B</b>	
$E_{\text{total}}$	-689.352053 <sup>c</sup>	-689.351928 <sup>c</sup>	0.08
$E_{\text{total}}^{\text{CP}}$	-689.343998 <sup>c</sup>	-689.343419 <sup>c</sup>	0.36
BSSE	5.06	5.34	0.28
$E_{\text{dfm}}$	1.24	0.81	-0.43
$E_{\text{int}}$	-4.38	-4.93	-0.55
$E_{\text{asn}}$	-3.14	-4.12	-0.98
VDE	360 <sup>d</sup>	65 <sup>d</sup>	-

<sup>a</sup>Relations between the quantities in the table are given as follows:

$$E_{\text{total}}^{\text{CP}} = E_{\text{total}} + \text{BSSE}$$

$$E_{\text{asn}} = E_{\text{total}}^{\text{CP}} - (E[(\text{H}_2\text{O})_6^-] + E[\text{Bz}]) = E_{\text{int}} + E_{\text{dfm}}$$

$$\Delta E = E[\text{B}] - E[\text{A}]$$

<sup>b</sup>Energies are given in units of kcal mol<sup>-1</sup> unless otherwise noted.

<sup>c</sup>Values are in Hartree atomic units.

<sup>d</sup>Values are in millielectronvolts.

observations, we infer that type I  $\rightarrow$  II interconversion in  $\text{Bz}\cdot(\text{H}_2\text{O})_6^-$  is thermodynamically driven in a manner such that a substantial portion of the complex anions flow into the product states of configuration **B** due to the larger  $E_{\text{asn}}$  gain, and that the potential-energy barrier relevant to the H-bond network transformation is surmountable with the internal energy imparted by the association reaction.

Concerning the energetics arguments described above, it seems worth discussing the origin of the preferential stabilization of configuration **B**. The relatively small VDE (0.16 eV) for **B** suggests importance of the intrinsic stability of the  $\text{Bz}\cdot(\text{H}_2\text{O})_6$  framework in configuration **B** rather than its strength of the excess electron binding. Subramanian *et al.* have predicted possible geometries for neutral complexes of benzene and water clusters by using M05-2X/6-31+G\*\* calculations.<sup>25</sup> Their results show that  $(\text{H}_2\text{O})_6$  having “book” motif interacts with Bz to form  $\text{Bz}\cdot(\text{H}_2\text{O})_6$  into two types of isomeric configurations; in their lower-energy configuration, designated as “BZW<sub>6b</sub>” in ref. 25, the O–H group at the spine of the “book” directly forms hydrogen-bond with the  $\pi$ -cloud of Bz, as is the case in configuration **B** of  $\text{Bz}\cdot(\text{H}_2\text{O})_6^-$ . It should be also noted that BZW<sub>6b</sub> and **B** are topologically equivalent to each other. We thus attribute the stability of configuration **B** largely to that of the neutral  $\text{Bz}\cdot(\text{H}_2\text{O})_6$  framework. This inference is further supported by the following experimental



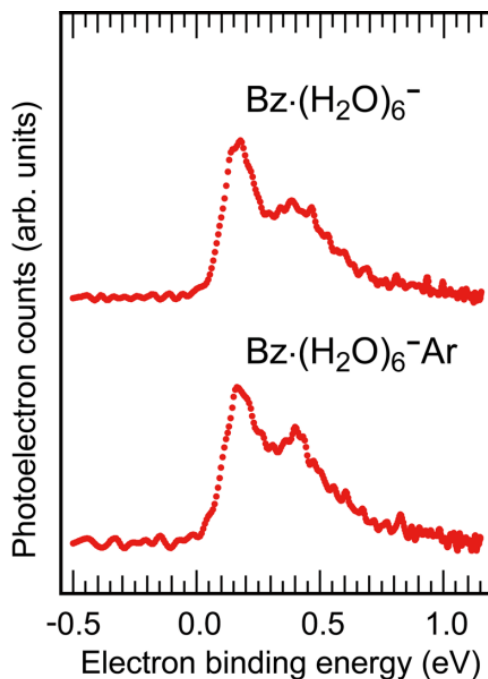


**Figure 3.4** Photoelectron spectra of  $\text{Bz}\cdot(\text{H}_2\text{O})_6^-$  (upper trace) and  $\text{Bz}\cdot(\text{H}_2\text{O})_6^- \text{Ar}$  (lower trace) formed via the  $\text{Bz}\cdot(\text{H}_2\text{O})_6\text{Ar}_m + e^-$  reaction in the electron-impact ionized free jet.

observation. Figure 3.4 displays the photoelectron spectra of  $\text{Bz}\cdot(\text{H}_2\text{O})_6^- \text{Ar}_k$  ( $k = 0, 1$ ) prepared via the electron attachment to neutral precursors:



The  $\text{Bz}\cdot(\text{H}_2\text{O})_6\text{Ar}_m$  precursors were prepared in the beam by a supersonic expansion of an  $\text{H}_2\text{O}(0.16\%)/\text{Bz}(0.03\%)/\text{Ar}$  gas mixture. Both in the  $\text{Bz}\cdot(\text{H}_2\text{O})_6^-$  and  $\text{Bz}\cdot(\text{H}_2\text{O})_6^- \text{Ar}$  spectra, the relative intensity of the lower-energy band, ascribable to the photodetachment from configuration **B**, is enhanced significantly as compared with that in the spectrum of  $\text{Bz}\cdot(\text{H}_2\text{O})_6^-$  formed via the Ar-mediated association process (Fig. 3.2(a)). This observation suggests that process (2) proceeds in such a way that the neutral precursor takes on the energetically-favored configuration  $\text{BZW}_{6b}$  and, with starting from the  $\text{BZW}_{6b}$  neutral, the product  $\text{Bz}\cdot(\text{H}_2\text{O})_6^- \text{Ar}_k$  anion is eventually formed with an enhanced branching fraction into configuration **B** along with a minor portion transformed into configuration **A**.

### 3.4 Summary

In summary, we have demonstrated by exploiting an Ar-mediated approach that  $(\text{H}_2\text{O})_6^-$  undergoes type I  $\rightarrow$  II interconversion in the process of complex formation with benzene. The interconversion occurs with a substantial change in the structural arrangement of hydrogen-bond network such that  $(\text{H}_2\text{O})_6^-$  even sacrifices the AA electron-binding motif to take on a specific form favorable for the complex formation with Bz, where a book-shaped  $(\text{H}_2\text{O})_6$  framework interacts with Bz through a nonconventional O–H $\cdots\pi$  hydrogen bond. Thus,  $(\text{H}_2\text{O})_6^-$  is prone to H-bond network transformation to attain more stable geometrical arrangements – or more favorable geometrical arrangements for the complex formation – but not to gain larger electron-binding energies. This inference is reinforced by the observation that electron capture by preformed neutral  $\text{Bz}\cdot(\text{H}_2\text{O})_6$  ends up with a large population of more weakly electron-binding  $\text{Bz}\cdot(\text{H}_2\text{O})_6^-$  of non-AA structure. The present study also shows that an amount of energy in the order of 3 – 4 kcal $\cdot$ mol $^{-1}$  is sufficient enough for  $(\text{H}_2\text{O})_6^-$  to sample a certain number of minima on the relevant potential energy landscape: hence, the Ar-mediated association process provides an intriguing possibility to get a microscopic insight into the transformation dynamics at play in H-bond networks composed of a restricted number of water molecules.

## References

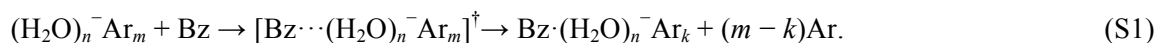
- 1 Kim, J.; Becher, I.; Cheshnovsky, O.; Johnson, M. A. *Chem. Phys. Lett.* **1998**, 297, 90–96.
- 2 Verlet, J. R. R.; Bragg, A. E.; Kammrath, A.; Cheshnovsky, O.; Neumark, D. M. *Science* **2005**, 307, 93–96.
- 3 Hammer, N. I.; Shin, J.-W.; Headrick, J. M.; Diken, E. G.; Roscioli, J. R.; Weddle, G. H.; Johnson, M. A. *Science* **2004**, 306, 675–679.
- 4 Hammer, N. I.; Roscioli, J. R.; Johnson, M. A. *J. Phys. Chem. A* **2005**, 109, 7896–7901.
- 5 Roscioli, J. R.; Hammer, N. I.; Johnson, M. A. *J. Phys. Chem. A* **2006**, 110, 7517–7520
- 6 Roscioli, J. R.; Hammer, N. I.; Johnson, M. A.; Diri, K.; Jordan, K. D. *J. Chem. Phys.* **2008**, 128, 104314.
- 7 Guasco, T. L.; Elliott, B. M.; Johnson, M. A.; Ding, J.; Jordan, K. D. *J. Phys. Chem. Lett.* **2010**, 1, 2396–2401.
- 8 Coe, J. V.; Arnold, S. T.; Eaton, J. G.; Lee, G. H.; Bowen, K. H. *J. Chem. Phys.* **2006**, 125, 014315.
- 9 Lee, S.; Kim, J.; Lee, S. J.; Kim, K. S. *Phys. Rev. Lett.* **1997**, 79, 2038–2041.
- 10 Tsurusawa, T.; Iwata, S. *Chem. Phys. Lett.* **2000**, 315, 433–440.
- 11 Suh, S. B.; Lee, H. M.; Kim, J.; Lee, J. Y.; Kim, K. S. *J. Chem. Phys.* **2000**, 113, 5273–5277.
- 12 Lee, H. M.; Suh, S. B.; Kim, K. S. *J. Chem. Phys.* **2003**, 118, 9981–9986.
- 13 Lee, H. M.; Lee, S.; Kim, K. S. *J. Chem. Phys.* **2003**, 119, 187–194.
- 14 Sommerfeld, T.; Gardner, S. D.; DeFusco, A.; Jordan, K. D. *J. Chem. Phys.* **2006**, 125, 174301.
- 15 Choi, T. H.; Jordan, K. D. *Chem. Phys. Lett.* **2009**, 475, 293–297
- 16 Herbert, J. M.; Head-Gordon, M. *J. Phys. Chem. A* **2005**, 109, 5217–5229.
- 17 Herbert, J. M.; Head-Gordon, M. *J. Am. Chem. Soc.* **2006**, 128, 13932–13939.
- 18 Herbert, J. M.; Head-Gordon, M. *Phys. Chem. Chem. Phys.* **2006**, 8, 68–78.
- 19 Yagi, K.; Okano, Y.; Sato, T.; Kawashima, Y.; Tsuneda, T.; Hirao, K. *J. Phys. Chem. A*, **2008**, 112, 9845–9853.
- 20 McCunn, L. R.; Gardenier, G. H.; Guasco, T. L.; Elliott, B. M.; Bopp, J. C.; Relph, R. A.; Johnson, M. A. *J. Chem. Phys.* **2008**, 128, 234311.
- 21 Augspurger, J. D.; Dykstra, C. E.; Zwier, T. S. *J. Phys. Chem.* **1993**, 97, 980–984.
- 22 Gruenloh, C. J.; Carney, J. R.; Arrington, C. A.; Zwier, T. S.; Fredericks, S. Y.; Jordan, K. D. *Science* **1997**, 276, 1678–1681.
- 23 Gruenloh, C. J.; Carney, J. R.; Hagemester, F. C.; Zwier, T. S. *J. Chem. Phys.* **2000**, 113, 2290–2303.
- 24 Kim, S.-J.; Seo, H.-Il.; Boo, B. H. *Mol. Phys.* **2009**, 107, 1261–1270.
- 25 Prakash, M.; Samy, K. G.; Subramanian, V. *J. Phys. Chem. A* **2009**, 113, 13845–13852.

- 26 Nakanishi, R; Nagata, T. *J. Chem. Phys.* **2009**, 130, 224309.
- 27 Johnson, M. A.; Lineberger, W. In *Techniques of Chemistry: Techniques for the Study of Ion-Molecule Reactions*, Farrar, J. M.; Saunders, W. H., Eds.; Wiley: New York, 1988; pp 591–635.
- 28 Eppink, A. T. J. B.; Parker, D. H. *Rev. Sci. Instrum.* **1997**, 68, 3477–3484.
- 29 Nakanishi, R; Muraoka, A.; Nagata, T. *Chem. Phys. Lett.* **2006**, 427, 56–61.
- 30 Dribinski, V.; Ossadtchi, A.; Mandelshtam, V. A.; Reisler, H. *Rev. Sci. Instrum.* **2002**, 73, 2634–2642.
- 31 Travers, M. J.; Cowles, D. C.; Ellison, G. B. *Chem. Phys. Lett.* **1989**, 164, 449–455.
- 32 Frisch, M. J.; Trucks, G. W.; Schlegel, H. B.; Scuseria, G. E.; Robb, M. A.; Cheeseman, J. R.; Montgomery, Jr., J. A.; Vreven, T.; Kudin, K. N.; Burant, J. R; et al. *Gaussian 03*, Revision A.02; Gaussian, Inc.: Wallingford CT, 2004.

## Supplemental material for Chapter 3

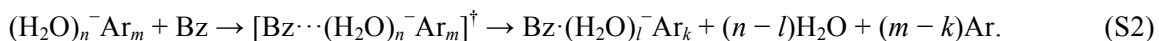
### S3.1 Ar-mediated association process

In the present study we exploit an Ar-mediated association process to prepare the  $\text{Bz}\cdot(\text{H}_2\text{O})_n^-$  complex anions:



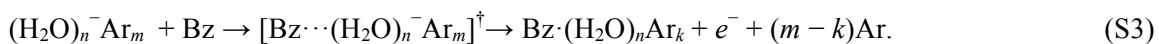
We determine the isomer distributions of  $(\text{H}_2\text{O})_n^- \text{Ar}_m$  and  $\text{Bz}\cdot(\text{H}_2\text{O})_n^- \text{Ar}_k$  both existing in a supersonic beam by using photoelectron spectroscopy and assume those as the isomer distributions of the reactant and product of process (S1); therefore, the size preservation of the water cluster anions during the reaction is key to the present study. In order to assure the validity of this approach, we discuss the possible decay channels of  $[\text{Bz}\cdots(\text{H}_2\text{O})_n^- \text{Ar}_m]^\ddagger$  formed in the Ar-mediated association process in terms of thermodynamic properties of the small water cluster anions.

Besides process (S1), one might raise an alternative possibility that the reaction proceeds as a water-network degradation via the  $\text{H}_2\text{O}$  evaporation:



We infer, however, on the following grounds that this is not the case here. The excess energy imparted to the nascent  $[\text{Bz}\cdots(\text{H}_2\text{O})_n^- \text{Ar}_m]^\ddagger$  species by the reaction is of the same order as the association energy between  $(\text{H}_2\text{O})_n^- \text{Ar}_m$  and Bz, which is calculated to be in the range 3 – 4 kcal mol<sup>-1</sup>. Even with taking into account the relative kinetic energy between  $(\text{H}_2\text{O})_n^- \text{Ar}_m$  and Bz in the condensation process, the available excess energy of the reaction is considerably smaller than the amount of energy required for breaking the hydrogen bonds to evaporate one  $\text{H}_2\text{O}$  molecule from  $(\text{H}_2\text{O})_n^-$  ( $\approx 10$  kcal mol<sup>-1</sup>).<sup>1, 2</sup> As the excess energy is dissipated primarily through a statistical mechanism, it is unlikely that process (S2) makes a significant contribution to the decay of  $[\text{Bz}\cdots(\text{H}_2\text{O})_n^- \text{Ar}_m]^\ddagger$ .

The less energy-demanding channel for the decay of  $[\text{Bz}\cdots(\text{H}_2\text{O})_n^- \text{Ar}_m]^\ddagger$  is the associative electron detachment:



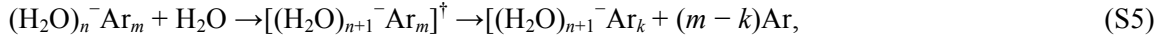
The vertical detachment energy (VDE) of type I form of  $(\text{H}_2\text{O})_6^-$  is 0.49 eV (11.3 kcal mol<sup>-1</sup>),<sup>3</sup> whereas the adiabatic electron affinity (AEA) is estimated to be on the order of 0.12 eV (2.8 kcal mol<sup>-1</sup>).<sup>4</sup> Although no information is available on the AEA of type II form of  $(\text{H}_2\text{O})_n^-$ , recent calculations predict that type II possesses smaller AEA than type I does.<sup>5</sup> As these AEAs are lower than the available excess energy of the reaction, it is possible that reaction (S3) proceeds competitively with (S1), which means that a portion of products is removed from the ion beam. Also

note that process (S1) is the least-energy demanding channel for the decay of  $[\text{Bz}\cdots(\text{H}_2\text{O})_n^-\text{Ar}_m]^\dagger$  because the binding energy of one Ar atom to  $(\text{H}_2\text{O})_n^-$  is  $\approx 1.3 \text{ kcal mol}^{-1}$ .<sup>6</sup>

It seems worth comparing the present system with the binary collisional reaction,  $(\text{H}_2\text{O})_n^- + \text{H}_2\text{O}$ . For  $n < 15$ , the reaction proceeds predominantly as the associative electron detachment process:<sup>7,8</sup>



This is because the AEAs of the small clusters are lower than the energy imparted to the  $[(\text{H}_2\text{O})_{n+1}]^\dagger$  intermediate by the condensation. Johnson et al. found that the associative detachment channel was dramatically suppressed in the Ar-mediated version of the reaction,



by rapid quenching of  $[(\text{H}_2\text{O})_{n+1}^-\text{Ar}_m]^\dagger$  through sequential Ar evaporation.<sup>9</sup> This observation is reasonably interpreted by the general truth that less energy-demanding reaction proceeds faster. Process (S5) can be regarded as the Ar-mediated growth-by-condensation of  $(\text{H}_2\text{O})_n^-$ .

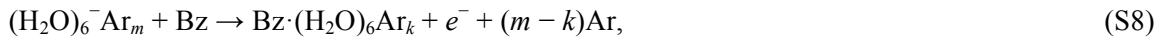
Based on the above discussion, we infer that process (S1) is the dominant pathway for the production of  $\text{Bz}\cdot(\text{H}_2\text{O})_n^-\text{Ar}_k$  species. More specifically, for  $n = 6$ , we propose that  $\text{Bz}\cdot(\text{H}_2\text{O})_6^-$  and  $\text{Bz}\cdot(\text{H}_2\text{O})_6^-\text{Ar}$  are prepared mainly via the following processes:



and



Here, the excess energy gained by the association events ( $3 - 4 \text{ kcal mol}^{-1}$ ) is consumed as the evaporation energy of three Ar atoms on average ( $1.3 \text{ kcal mol}^{-1}/\text{Ar}$ ). In addition to these processes, the associative electron detachment,



possibly competes with processes (S6) and (S7) because the excess energy is comparable in magnitude to – or even larger than – the AEAs of the relevant species. This might affect the product isomer distributions in the following manner. In general, the rate of thermionic emission increases with the amount of internal energy in excess of the threshold for electron ejection. As the AEA of type II form of  $(\text{H}_2\text{O})_6^-$  is predicted to be smaller than that of type I,  $[\text{Bz}\cdots(\text{H}_2\text{O})_6^-\text{Ar}_m]^\dagger$  is more likely to undergo electron ejection on the pathway leading to configuration **B**, which contains  $(\text{H}_2\text{O})_6^-$  of type II as a substructure. Thus, the associative electron detachment (S8), if it occurs, gives rise to an apparent reduction in the yield of isomer **B**. In the next section, we will further discuss this issue with the aid of additional experimental observations.

### S3.2 PES measurement of $\text{Bz}(\text{H}_2\text{O})_6^- \text{Ar}$

In the present study, the Ar-mediated association process provides  $\text{Bz} \cdot (\text{H}_2\text{O})_6^-$  and  $\text{Bz} \cdot (\text{H}_2\text{O})_6^- \text{Ar}$  as the product anions for  $n = 6$  (see Figure 3.1(b) in the main text). In addition to the results described in the main text, we also examined the isomer distribution of  $\text{Bz} \cdot (\text{H}_2\text{O})_6^- \text{Ar}$  by using photoelectron spectroscopy. According to the Ar-mediated scheme,  $\text{Bz} \cdot (\text{H}_2\text{O})_6^- \text{Ar}$  is produced from  $[\text{Bz} \cdots (\text{H}_2\text{O})_6^- \text{Ar}_m]^\ddagger$  ensembles with larger  $m$  values and/or smaller internal energies; the system survives the evaporative cooling process with one Ar still remaining weakly bound to the product anion. We therefore expect that the  $[\text{Bz} \cdots (\text{H}_2\text{O})_6^- \text{Ar}_m]^\ddagger$  intermediate is quenched by sequential Ar evaporation so rapidly that it eludes the electron detachment with a high probability and, as a result, the product  $\text{Bz} \cdot (\text{H}_2\text{O})_6^- \text{Ar}$  eventually preserves an isomer distribution closer to the nascent.

Figure S1 displays the photoelectron spectra of  $(\text{H}_2\text{O})_6^- \text{Ar}_m$  ( $m = 1 - 6$ ) responsible for the  $\text{Bz} \cdot (\text{H}_2\text{O})_6^- \text{Ar}_k$  production in the left panel (labeled as **R**), and those of the  $\text{Bz-d}_6 \cdot (\text{H}_2\text{O})_6^- \text{Ar}_k$  ( $k = 0, 1$ ) products in the right panel (labeled as **P**). We used  $\text{Bz-d}_6$  as the target molecule in the measurement for the sake of  $m/z$  discrimination and assignment. As readily seen in Figure S1, all the  $(\text{H}_2\text{O})_6^- \text{Ar}_m$  spectral features are dominated by a single band ascribable to the photodetachment from the high electron-binding isomer (type I). The  $\text{Bz-d}_6 \cdot (\text{H}_2\text{O})_6^-$  spectrum shows a band profile almost identical to that of  $\text{Bz} \cdot (\text{H}_2\text{O})_6^-$  (see Figure 3.2(a) in the main text), as is only to be expected. More importantly, the  $\text{Bz-d}_6 \cdot (\text{H}_2\text{O})_6^- \text{Ar}$  spectrum exhibits a similar band profile consisting of two components, but the low-energy component (isomer **B**) is slightly enhanced in intensity as compared with the  $\text{Bz-d}_6 \cdot (\text{H}_2\text{O})_6^-$  spectrum. This observation is consistent with the above arguments that the associative electron detachment can modify the nascent isomer distribution in a way that the branching fraction is apparently reduced for the production of isomer **B**. On the basis of the fact that the low-energy band is enhanced only slightly in the  $\text{Bz-d}_6 \cdot (\text{H}_2\text{O})_6^- \text{Ar}$  spectrum, we infer that process (S8) scarcely deteriorates the nascent isomer distribution present in  $\text{Bz-d}_6 \cdot (\text{H}_2\text{O})_6^-$ . It should be understood that such is the case with  $\text{Bz} \cdot (\text{H}_2\text{O})_6^-$ . By combining the discussion here with the above consideration that the  $\text{H}_2\text{O}$  evaporation pathway (eq. (S2)) is energetically inaccessible, we infer that reaction (S1) is the dominant process responsible for the isomer distributions observed in the present study.

### S3.3. Computational details

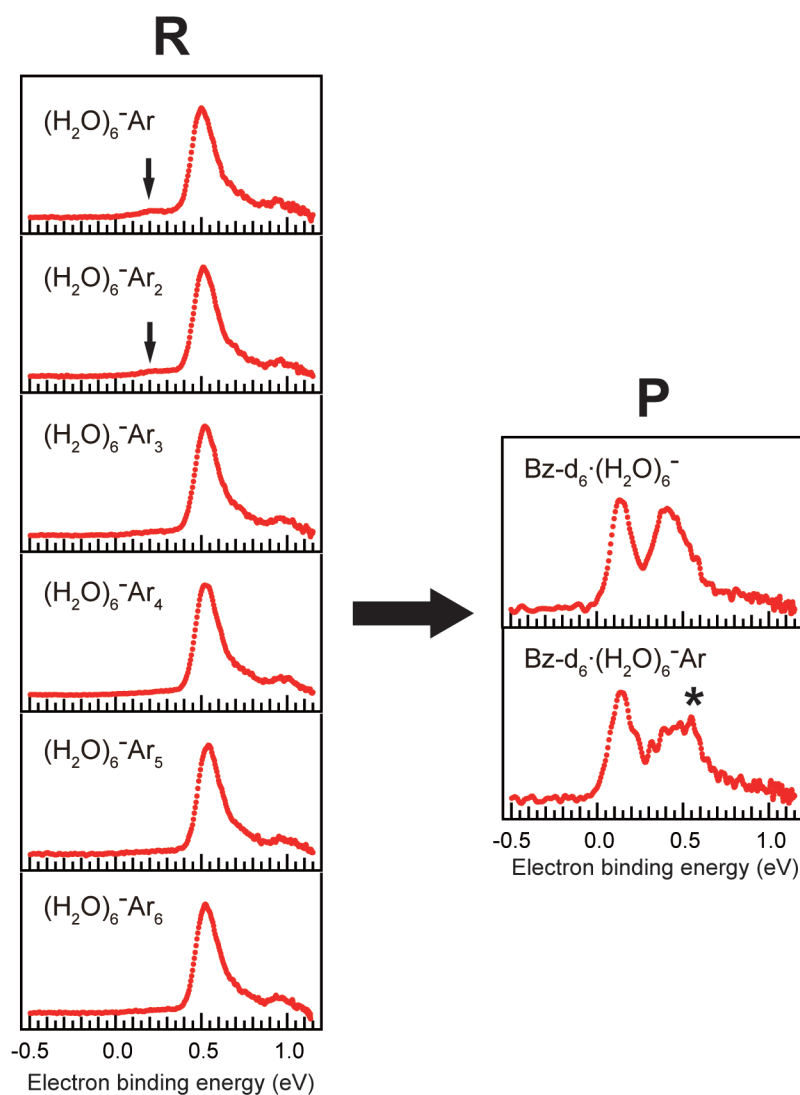
The geometries of  $(\text{H}_2\text{O})_6^-$  (isomers 6Af and 6Bd) and  $\text{Bz} \cdot (\text{H}_2\text{O})_6^-$  (**A** and **B**) were optimized by the second-order Møller-Plesset perturbation (MP2) method. We employed Dunning's aug-cc-pVDZ basis set<sup>10, 11</sup> with additional diffuse functions for oxygen and hydrogen atoms in  $(\text{H}_2\text{O})_6^-$  (denoted aug-cc-pVDZ+diff) having exponents of  $9.87 \times 10^{-3}$  au for O(s),  $8.57 \times 10^{-3}$  for O(p), and  $3.72 \times 10^{-3}$  for H(s). The single point calculations were also performed by the coupled-cluster method with single,

double, and perturbative triple excitations [CCSD(T)] with the same basis set, at the MP2-optimized geometries [CCSD(T)/aug-cc-pVDZ+diff //Mp2/aug-cc-pVDZ+diff]. The calculated CCSD(T) energies were used to evaluate the quantities listed in Table 1 of the main text. The basis-set superposition errors were corrected by the counterpoise (CP) method<sup>12</sup> after the geometry optimizations without CP corrections.

### **S3.4 Optimized geometries**

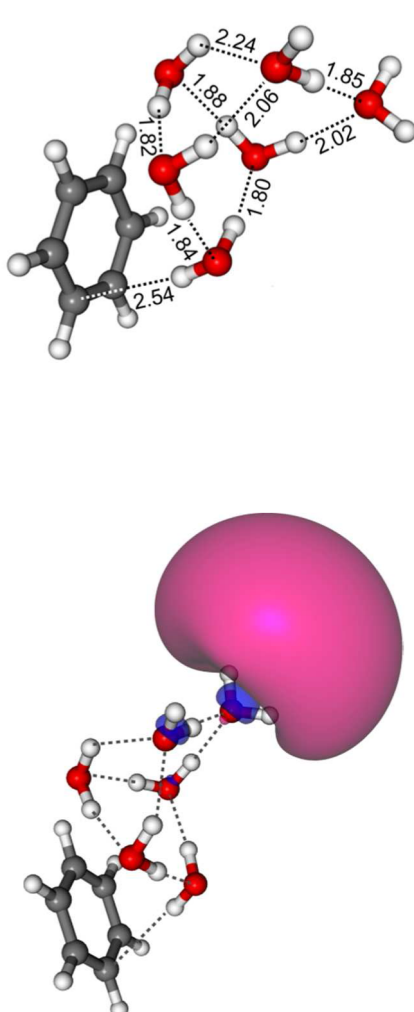
The optimized geometries for isomers A and B of  $\text{Bz}\cdot(\text{H}_2\text{O})_6^-$  are given in Tables S1 and S2, respectively, as their x, y, z-coordinates in the “standard orientation” of the Gaussian 03 package.<sup>13</sup>





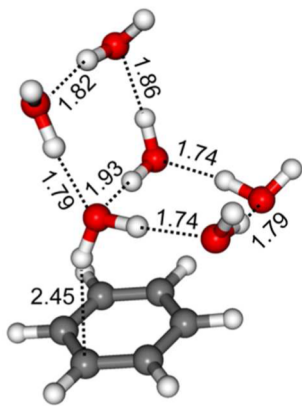
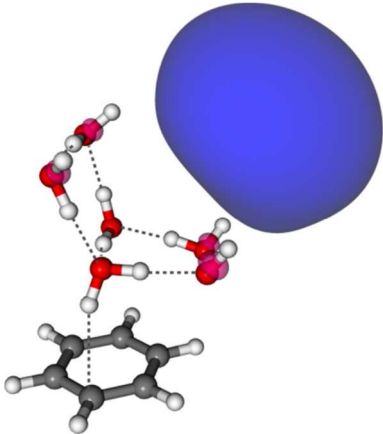
**Figure S1** Photoelectron spectra of  $(\text{H}_2\text{O})_6^- \text{Ar}_m$  (left panel) and  $\text{Bz-d}_6 \cdot (\text{H}_2\text{O})_6^- \text{Ar}_k$  (right panel). **R** represents the reactant species and **P** the product anions.  $(\text{H}_2\text{O})_6^- \text{Ar}_m$  with  $m \geq 3$  mainly contribute to the Ar-mediated reactions (see text). The hump marked with an arrow is assigned to isomer II of  $(\text{H}_2\text{O})_6^-$ . In the  $\text{Bz-d}_6 \cdot (\text{H}_2\text{O})_6^- \text{Ar}$  spectrum, the high-energy band is accompanied with a shoulder at  $\approx 0.6$  eV as indicated by the asterisk. The shoulder component is tentatively assigned to an isomeric form of the high electron-binding isomer (type I'), which is eventually quenched by sequential Ar evaporation during the formation of  $\text{Bz-d}_6 \cdot (\text{H}_2\text{O})_6^- \text{Ar}$ .

Table S1. MP2 geometry for isomer A of  $\text{Bz}\cdot(\text{H}_2\text{O})_6^-$ 

Structure <sup>a</sup>	coordinates (Angstroms)			
	x	y	z	
	O	1.106418	1.602568	0.420816
	H	1.158459	0.779151	0.952878
	H	2.038278	1.791094	0.209035
	O	1.239754	-0.952371	1.671012
	H	0.932226	-1.357072	0.826234
	H	2.194336	-1.120853	1.610320
	O	0.794416	-1.894755	-0.911423
	H	0.415603	-1.091067	-1.333522
	H	1.757007	-1.772641	-0.997936
	H	0.229857	1.047234	-1.044460
	O	-0.215703	0.578549	-1.789942
	H	-1.152821	0.613066	-1.546912
	H	4.420684	-1.656084	-0.301383
	O	3.561983	-1.234461	-0.160563
	H	3.761002	-0.278300	-0.258079
	H	4.297029	1.874964	-1.161152
	O	3.974684	1.560622	-0.297891
	H	4.684881	1.839866	0.308730
	C	-2.349122	1.318760	0.831982
	C	-1.693426	0.186854	1.353226
	C	-1.926844	-1.082844	0.790919
	C	-2.815716	-1.221963	-0.292275
	C	-3.476908	-0.090845	-0.811557
	C	-3.243944	1.180905	-0.247802
H	-2.140717	2.308009	1.249101	
H	-0.976201	0.291182	2.170430	
H	-1.394455	-1.955179	1.177953	
H	-2.977149	-2.205519	-0.743199	
H	-4.160412	-0.196428	-1.659924	
H	-3.744265	2.062170	-0.661144	

<sup>a</sup> The pink-colored shaded surface depicts the isosurface contour of the singly occupied molecular orbital with the fraction of electrons equal to 0.5.

Table S2. MP2 geometry for isomer **B** of  $\text{Bz}\cdot(\text{H}_2\text{O})_6^-$ 

Structure <sup>a</sup>	coordinates (Angstroms)			
	x	y	z	
	O	-1.384599	0.530646	-1.441661
	H	-2.343112	0.334213	-1.366781
	H	-0.992505	-0.058812	-0.766981
	H	-3.789714	-0.926691	-0.223287
	O	-4.037537	-0.277752	-0.919190
	H	-4.602892	0.357819	-0.460898
	H	-0.335615	-0.075180	1.420150
	O	-0.479793	-0.900251	0.893697
	H	0.407047	-1.273928	0.775622
	O	-2.980143	-2.065228	0.945240
	H	-2.060526	-1.732412	1.033190
	H	-3.312093	-2.108985	1.851280
	H	-0.901087	2.060929	-0.783752
	O	-0.497131	2.823719	-0.293281
	H	-1.150730	3.532677	-0.354094
	O	-0.116964	1.511503	2.101863
	H	-0.283393	2.097659	1.325786
	H	-0.745501	1.804820	2.775934
	C	2.752975	0.054605	0.879029
	C	2.201724	0.963357	-0.045161
	C	1.740079	0.505656	-1.293923
	C	1.824627	-0.862077	-1.619117
C	2.378443	-1.773105	-0.697427	
C	2.844607	-1.313859	0.553052	
H	3.087866	0.408832	1.858010	
H	2.102809	2.020003	0.214271	
H	1.284551	1.207277	-1.996634	
H	1.441460	-1.218299	-2.579672	
H	2.439673	-2.837060	-0.946701	
H	3.268374	-2.021418	1.272498	

<sup>a</sup> The pink-colored shaded surface depicts the isosurface contour of the singly occupied molecular orbital with the fraction of electrons equal to 0.5.

### S3.5 References

1. Klots, C. E. *J. Chem. Phys.* 1985, 83, 5854–5860.
2. Campagnola, P. J.; Posey, L. A.; Johnson, M. A. *J. Chem. Phys.* 1991, 95, 7998–8004.
3. Coe, J. V.; Arnold, S. T.; Eaton, J. G.; Lee, G. H.; Bowen, K. H. *J. Chem. Phys.* 2006, 125, 041315.
4. Elliott, B. M.; McCunn, L. R.; Johnson, M. A. *Chem. Phys. Lett.* 2008, 467, 32–36.
5. Choi, T. H.; Jordan, K. D. *Chem. Phys. Lett.* 2009, 475, 293–297.
6. McCunn, L. R.; Headrick, J. M.; Johnson, M. A. *Phys. Chem. Chem. Phys.* 2008, 10, 3118–3123.
7. Knapp, M.; Echt, O.; Kreisle, D.; Recknagel, E. *J. Phys. Chem.* 1987, 91, 2601–2607.
8. Campagnola, P. J.; Cyr, D. M.; Johnson, M. A. *Chem. Phys. Lett.* 1991, 181, 206–212.
9. Shin, J.-W.; Hammer, N. I.; Headrick, J. M.; Johnson, M. A. *Chem. Phys. Lett.* 2004, 399, 349–353.
10. Dunning, T. H., Jr. *J. Chem. Phys.* 1989, 90, 1007–1023.
11. Kendall, R. A., Dunning, T. H., Jr.; Harrison, R. J. *J. Chem. Phys.* 1992, 96, 6796–6806.
12. Boys, S. F.; Bernardi, F. *Mol. Phys.* 1970, 19, 553–566.
13. Frisch, M. J.; Trucks, G. W.; Schlegel, H. B.; Scuseria, G. E.; Robb, M. A.; Cheeseman, J. R.; Montgomery, Jr., J. A.; Vreven, T.; Kudin, K. N.; Burant, J. C.; et al. Gaussian 03, Revision A.02; Gaussian, Inc.: Wallingford CT, 2004.

# Chapter 4

## Formation and photodestruction of *dual dipole-bound* anion $(\text{H}_2\text{O})_6\{e^-\}\text{CH}_3\text{NO}_2$

### ABSTRACT

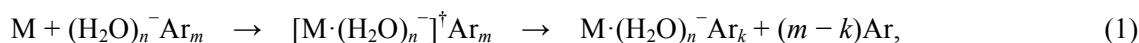
A new type of dipole-bound anion composed of water and nitromethane ( $\text{CH}_3\text{NO}_2$ ) is formed via the incorporation of  $\text{CH}_3\text{NO}_2$  into argon-solvated water hexamer anions,  $(\text{H}_2\text{O})_6^-\text{Ar}_m$ . The reaction proceeds as an Ar-mediated process such that an effective energy dissipation through sequential Ar evaporation gives rise to the formation of  $[\text{CH}_3\text{NO}_2 \cdot (\text{H}_2\text{O})_6]^-$ . Photoelectron spectroscopy is employed to probe the electronic properties of the  $[\text{CH}_3\text{NO}_2 \cdot (\text{H}_2\text{O})_6]^-$  anion, which reveals that the dipole-bound nature of  $(\text{H}_2\text{O})_6^-$  remains almost intact in the product anion; the vertical detachment 26 energy of  $[\text{CH}_3\text{NO}_2 \cdot (\text{H}_2\text{O})_6]^-$  is determined to be  $0.65 \pm 0.02$  eV. This spectroscopic finding, together with other suggestive evidences, allows us to refer to  $\text{CH}_3\text{NO}_2 \cdot \text{H}_2\text{O}_6^-$  as a *dual dipole-bound* anion described as  $(\text{H}_2\text{O})_6\{e^-\}\text{CH}_3\text{NO}_2$ , where the diffuse excess electron interacts with both the  $(\text{H}_2\text{O})_6$  and  $\text{CH}_3\text{NO}_2$  moieties via the electron-dipole interactions. The photodestruction of  $(\text{H}_2\text{O})_6\{e^-\}\text{CH}_3\text{NO}_2$  at 2134 nm 0.58 eV occurs with a competition between electron detachment and fragmentation. The latter leads exclusively to the formation of  $\text{CH}_3\text{NO}_2^-\cdot(\text{H}_2\text{O})_3$ , indicating that the dual dipole-bound anion serves as a precursor to the hydrated valence anion of  $\text{CH}_3\text{NO}_2$ .

This chapter has been reproduced in part with permission from the following previously published article: Nakanishi, R.; Nagata, T. *Journal of Chemical Physics* 2009, 130, 224309. DOI: 10.1063/1.3152636 Copyright 2009 American Institute of Physics

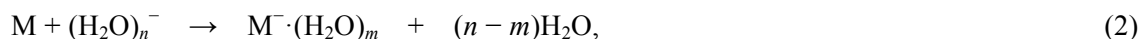
## 4.1 Introduction

This chapter is focused on cluster analogs of hydrated electron ( $e^-_{\text{aq}}$ ) scavenging reaction in solution: the reaction of the water cluster anions,  $(\text{H}_2\text{O})_n^-$ , with an electron scavenging molecule. As mentioned in the preceding chapters,  $(\text{H}_2\text{O})_n^-$  have provided us with a unique opportunity to explore the nature of  $e^-_{\text{aq}}$  at the molecular level by employing gas-phase experimental techniques<sup>1-12</sup> in combination with quantum mechanical calculations.<sup>13-17</sup> The electronic properties of  $(\text{H}_2\text{O})_n^-$  have been investigated systematically by photoelectron spectroscopy,<sup>1-3</sup> which has revealed the presence of isomeric forms in  $(\text{H}_2\text{O})_n^-$  distinguishable by the difference in their electron-binding energies. A series of infrared spectroscopic studies have so far provided detailed information on the distinctive manner of electron accommodation in  $(\text{H}_2\text{O})_n^-$  especially in the small size regime,<sup>4-9</sup> the clusters take on a specific form of hydrogen-bond network to bind a diffuse excess electron. Femtosecond transient spectroscopy has also been applied to the  $(\text{H}_2\text{O})_n^-$  system, revealing the fast electronic relaxation dynamics involving nonadiabatic processes.<sup>10-12</sup> The chemical properties of  $(\text{H}_2\text{O})_n^-$  were studied by using mass spectrometric techniques.<sup>18-20</sup> These experiments showed that the  $(\text{H}_2\text{O})_n^-$  anions served as one-electron reducing reagents as  $e^-_{\text{aq}}$  in solution:  $(\text{H}_2\text{O})_n^-$  react with neutral electron scavengers to form hydrated valence anions,  $X^-\cdot(\text{H}_2\text{O})_m$ , via either dissociative or nondissociative charge transfer.

As described in the previous two chapters, the Ar-mediated association,<sup>21</sup>



was successfully employed to trap a fleeting anion complex,  $\text{M}(\text{H}_2\text{O})_n^-$ . This approach takes advantage of rapid quenching of an energized  $[\text{M}\cdot(\text{H}_2\text{O})_n^-]^\ddagger$  anion by evaporative loss of Ar atoms. In the present work, we applied the Ar-mediated approach to the charge transfer reactions of  $(\text{H}_2\text{O})_n^-$ :



where the target molecule having positive electron affinity deprives  $(\text{H}_2\text{O})_n^-$  of the loosely bound electron to form a valence anion, which is followed by the stabilization of the product anion by partial hydration into the form of  $\text{M}^-\cdot(\text{H}_2\text{O})_m$ . From the microscopic point of view, the incoming molecule interacts with the diffuse electron cloud sticking out of  $(\text{H}_2\text{O})_n^-$  prior to accommodation of the electron into an outer valence orbital. Especially when the molecule has a large dipole moment capable of forming a dipole-bound state, the interaction between the dipole and the diffuse electron possibly dominates the early stage of the collision process between M and  $(\text{H}_2\text{O})_n^-$ . In such a case, one can expect the existence of a weakly bound intermediate species,  $[\text{M}\cdot\cdot(\text{H}_2\text{O})_n^-]$ , constructed by the electron-dipole interactions. It is also natural to expect that the intermediate species, if energized, becomes unstable against autodetachment, fragmentation or decay into the valence anionic state of M.

The aim of the present study is to trap the intermediate species by employing the Ar-mediated method. It is also our purpose to demonstrate that the intermediate species, once energized, decays into the valence anion that is the final product of process (2). In this article, we deal with the reaction between  $(\text{H}_2\text{O})_n^- \text{Ar}_m$  and nitromethane ( $\text{CH}_3\text{NO}_2$ ).

Nitromethane (hereafter referred to as NM for brevity in some cases) is a highly polar molecule possessing a dipole moment of  $3.46 \text{ D}^{22}$ , which is sufficiently large to form a dipole-bound state.<sup>23</sup> The NM molecule also forms a stable valence anion; the adiabatic electron affinity of NM was determined to be  $172 \pm 6 \text{ meV}$ .<sup>24</sup> Due to its ability to form both a dipole-bound and a valence anion, the formation and properties of  $\text{CH}_3\text{NO}_2^-$  have been extensively investigated both experimentally and theoretically.<sup>24-29</sup> One of the remarkable results shown by Rydberg electron transfer (RET) experiment<sup>25</sup> is that the dipole-bound state of NM plays a role of the “doorway” state to the valence anion, being consistent with theoretical predictions.<sup>28</sup>

Here, we report on the formation of a new type of anion with the formula  $[\text{NM} \cdot (\text{H}_2\text{O})_6]^-$ , which can be regarded as the intermediate of process (2), produced in the reactions between NM and  $(\text{H}_2\text{O})_6 \text{Ar}_m^-$  in a molecular beam. The electronic properties of the  $[\text{NM} \cdot (\text{H}_2\text{O})_6]^-$  species are probed by negative ion photoelectron spectroscopy, revealing the dipole-bound nature of the anion. Photodestruction experiment is also performed at  $2.1 \mu\text{m}$ . Two types of decay channels, photodetachment and photofragmentation, are observed for  $[\text{NM} \cdot (\text{H}_2\text{O})_6]^-$  energized slightly above the photodetachment threshold. Based on these experimental findings, we discuss the properties of the newly-formed  $[\text{NM} \cdot (\text{H}_2\text{O})_6]^-$  anion as an intermediate species, from which one can access directly to the “collision complex” at play in the charge transfer reaction (process (2)).

## 4.2 Experimental

The experimental apparatus used in the present study consists of a cluster ion source, a time-of-flight (TOF) mass spectrometer, and a photoelectron spectrometer. Details of the apparatus has been described elsewhere.<sup>30, 31</sup> The  $(\text{H}_2\text{O})_n^- \text{Ar}_m$  reactants were prepared in an electron-impact ionized free jet.<sup>32</sup> An argon gas containing a trace amount of water ( $\approx 0.2\%$  by volume) was expanded through a pulsed nozzle at a stagnation pressure of  $\approx 0.4 \text{ MPa}$ . The free jet was then crossed with a  $200\text{-eV}$  electron beam at the expansion region. In the ionized jet secondary slow electrons produced by the electron impact were captured successively by preexisting neutral  $(\text{H}_2\text{O})_N \text{Ar}_M$  clusters, resulting in the formation of  $(\text{H}_2\text{O})_n^- \text{Ar}_m$ . Figure 4.1(a) displays the ion distribution of  $(\text{H}_2\text{O})_n^- \text{Ar}_m$  produced in the present source, which exhibits an abrupt onset at  $(n, m) = (6, 0)$  followed by the  $(n, m)$  series with  $n = 6$  and  $7$ , and  $m \leq 8$ . Bare  $(\text{H}_2\text{O})_n^-$  clusters with  $n \geq 8$  appear as minor species in the mass spectrum. This characteristic ion distribution has been attributed

to the distinctive ability of neutral precursors,  $(\text{H}_2\text{O})_6$  and  $(\text{H}_2\text{O})_7$ , to form dipole-bound anions.<sup>13</sup> Thanks to the abrupt onset along with the distinguishable distribution, one can exploit the ion source as coarsely  $n$ -selected  $(\text{H}_2\text{O})_n^- \text{Ar}_m$  reagents. When the nitromethane sample gas was introduced through an effusive nozzle into the source chamber, the ambient pressure was increased typically up to  $4.010^{-3}$  Pa. The  $(\text{H}_2\text{O})_n^- \text{Ar}_m$  clusters reacted with the ambient NM while drifting in the source chamber. The product anions were extracted at  $\approx 15$  cm downstream from the nozzle, perpendicularly to the initial beam direction by applying a pulsed electric field. The anions were further accelerated up to 1.25 keV, and mass-analyzed by a 1.9-m TOF mass spectrometer.

Photoelectron measurements were performed at 355, 532 and 1064 nm by using a velocity-map imaging (VMI)<sup>33</sup> photoelectron spectrometer equipped at the end of the TOF mass spectrometer. The anions of interest, mass-selected prior to entering the VMI spectrometer, were intersected with the output of a pulsed Nd:YAG laser at the center of the spectrometer. Photoelectrons were extracted perpendicular to both the ion and the laser beams by a static electric field, and projected onto a 40-mm diameter microchannel plate (MCP) coupled to a phosphor screen. The MCP was gated with a 300-ns time window coincident with the photoelectron arrival in order to reduce background noise. The photoelectron images on the phosphor screen were recorded using a CCD camera (512\*512 pixels). The images were acquired typically for 20000 – 60000 laser shots. Photoelectron spectra were reconstructed from the obtained images using the basis set expansion (BASEX) method.<sup>34</sup> The spectral resolution was  $\approx 40$  meV at the photoelectron kinetic energy of 500 meV after the reconstruction procedure. The measured electron kinetic energy was calibrated against the known photoelectron bands of  $\text{O}_2^-$  and  $\text{I}^-$ .<sup>35, 36</sup>

A magnetic-bottle type photoelectron spectrometer was employed in the 266-nm measurement because the magnetic bottle often gave a larger signal-to-noise ratio than the VMI spectrometer in the measurements at shorter wavelengths. The mass-selected anions were irradiated by the forth harmonic (266 nm) of a Nd:YAG laser in an inhomogeneous magnetic field ( $\approx 1000$  G). A weak field ( $\approx 10$  G) guided the photoelectrons to a detector mounted at the end of a 1-m flight tube. The photoelectron signals were accumulated for 50 000 laser shots with background subtraction. The typical resolution of the spectrometer was  $\sim 100$  meV at the photoelectron kinetic energy of 1 eV. The measured electron kinetic energy was calibrated against the  $\text{I}^-$  photoelectron bands.<sup>36</sup>

Photodestruction measurements were carried out by using a function of the equipment as a tandem mass spectrometer. A 2.1- $\mu\text{m}$  radiation was employed as the excitation wavelength, which was the Stokes component from a hydrogen Raman shifter pumped by the fundamental output (1064 nm) of the Nd:YAG laser. The fundamental output was downconverted to 2.1  $\mu\text{m}$  via the Raman scattering associated with the S(1) transition ( $\nu = 1, J = 3 \leftarrow \nu = 0, J = 1$ ) of  $\text{H}_2$ . The 2.1- $\mu\text{m}$  output was isolated by passing through a dichroic mirror, further dispersed by a Pellin-Broca prism, and



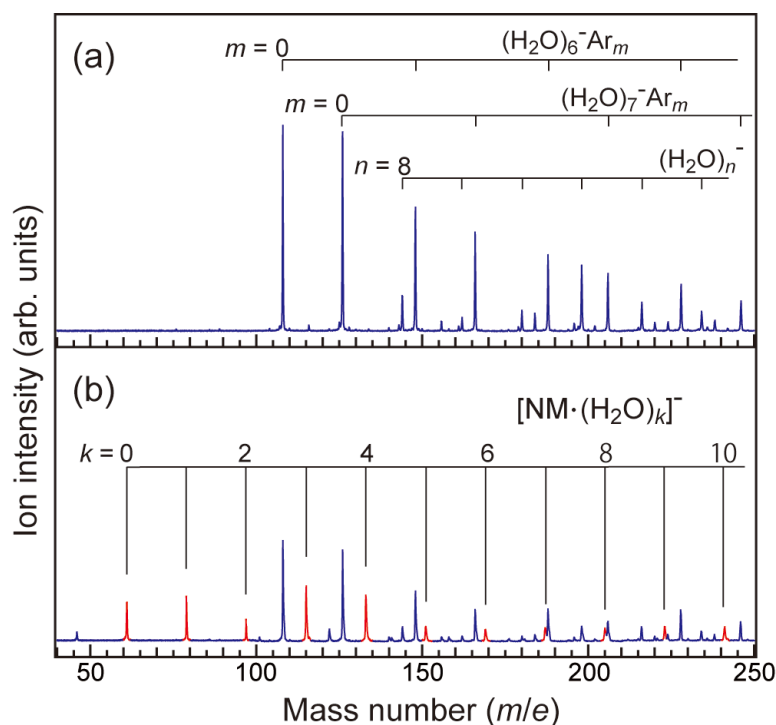


**Figure 4.1** Mass spectra of (a) the  $(\text{H}_2\text{O})_n^- \text{Ar}_m^-$  reactants and (b) the product anions in the  $(\text{H}_2\text{O})_n^- \text{Ar}_m^- + \text{NM}$  reaction. In trace (b), the product  $[\text{NM} \cdot (\text{H}_2\text{O})_k]^-$  peaks are interspersed between the unreacted  $(\text{H}_2\text{O})_n^- \text{Ar}_m^-$  peaks.

and allowed to intersect with the mass-selected ion bunch at the primary focus of the tandem mass spectrometer. The photofragments along with the residual parent anions were collinearly reaccelerated by a 1.5-kV electric pulse at the second acceleration assembly, and mass-analyzed during the flight in the rest of the TOF tube. The fragment ion signals were accumulated typically for 500 laser shots.

## 4.3 Results and Discussion

### 4.3.1 Formation of “dual dipole-bound” anion $(\text{H}_2\text{O})_6\{e^-\}\text{NM}$

As shown in Fig. 4.1(b), the intensities of the  $(\text{H}_2\text{O})_n^- \text{Ar}_m^-$  peaks were decreased by  $\approx 50\%$  and mass peaks ascribable to the product anions emerged in the spectrum, when the NM gas was introduced into the source chamber. The product mass peaks are assignable unquestionably to species with the formulae  $[\text{NM} \cdot (\text{H}_2\text{O})_k]^-$  ( $k \geq 0$ ). The electronic properties of the  $[\text{NM} \cdot (\text{H}_2\text{O})_k]^-$

anions were then probed by photoelectron spectroscopy. Figure 4.2 displays the photoelectron spectra of  $[\text{NM}\cdot(\text{H}_2\text{O})_k]^-$  with  $k = 0 - 6$ . The spectra were recorded at 532 nm (2.33 eV) for  $k = 0 - 1$ , 355 nm (3.49 eV) for  $k = 2 - 3$  and 266 nm (4.66 eV) for  $k = 4 - 6$  along with increasing electron binding energy of  $[\text{NM}\cdot(\text{H}_2\text{O})_k]^-$  with  $k$ . The  $k \geq 7$  species eventually eluded the photoelectron measurements due firstly to its large electron binding energy and secondly to the severe background noise arising from the stray electrons with low kinetic energies in the 266 nm measurements. The main feature of the  $k = 0 - 6$  spectra consists of a bell-shaped band; the  $k = 3$  and 4 bands are accompanied by a sharp rising edge due to autodetachment near the high-energy cutoff of the spectra. The maxima of the bell-shaped bands correspond to the vertical detachment energies (VDEs) of the anions. The VDE values determined by the band-envelop analysis<sup>37</sup> are listed in Table 4.1. Another significant feature in the present results is a hump appearing around 0.7 eV in the  $k = 6$  spectrum. As the hump appeared as a broad band due to the high kinetic energy imparted to photoelectrons in the 266 nm measurements, the photoelectron spectrum of  $[\text{NM}\cdot(\text{H}_2\text{O})_6]^-$  was reexamined at 1064 nm (1.17 eV). The 1064-nm measurement provided a sharp photoelectron band as shown by the inset in the bottom panel of Fig. 4.2. The 1064-nm spectrum is also shown by an expanded scale in Fig. 4.3 along with the  $(\text{H}_2\text{O})_6^-$  spectrum for comparison. It is apparent in Fig. 4.3 that the two spectra conspicuously resemble each other except that the main band shifts toward higher binding energies by 0.17 eV in the  $[\text{NM}\cdot(\text{H}_2\text{O})_6]^-$  spectrum. Based on the results shown in Figs. 4.2 and 4.3, we draw the following conclusions: (1) the monomer anion of nitromethane ( $\text{NM}^-$ ) is formed as an ionic core in  $[\text{NM}\cdot(\text{H}_2\text{O})_k]^-$  ( $k = 0 - 6$ ); i.e., the  $[\text{NM}\cdot(\text{H}_2\text{O})_k]^-$  species can be represented as hydrated  $\text{NM}^-$  anions,  $\text{NM}^-\cdot(\text{H}_2\text{O})_k$ , (2) an anionic form other than  $\text{NM}^-\cdot(\text{H}_2\text{O})_k$  coexists in  $[\text{NM}\cdot(\text{H}_2\text{O})_6]^-$ ; its electronic properties rather resemble those of  $(\text{H}_2\text{O})_6^-$  and are characterized by a small VDE attributable to a dipole-bound nature. Conclusion (1) is derived from the facts that the  $k = 0$  spectrum (Fig. 4.2) agrees well with that of the monomer anion of nitromethane,<sup>25</sup> and that the VDE of  $[\text{NM}\cdot(\text{H}_2\text{O})_k]^-$  increases by 0.3 – 0.6 eV with each additional  $\text{H}_2\text{O}$  (Table 4.1), which is ascribable to the stabilization of  $\text{NM}^-$  by hydration. Conclusion (2) stems from the observation that the  $[\text{NM}\cdot(\text{H}_2\text{O})_6]^-$  and  $(\text{H}_2\text{O})_6^-$  spectra exhibit almost identical features at 1064 nm (Fig. 4.3). It is also noted here that no photoelectron band was observed by 1064-nm irradiation on  $[\text{NM}\cdot(\text{H}_2\text{O})_k]^-$  ( $k = 1 - 5$ ).

As mentioned above, the dipole-bound nature of  $(\text{H}_2\text{O})_6^-$  persists in the weakly electron-binding species formed in  $[\text{NM}\cdot(\text{H}_2\text{O})_6]^-$ . As the spectral profile of  $(\text{H}_2\text{O})_6^-$  remains almost intact in the  $[\text{NM}\cdot(\text{H}_2\text{O})_6]^-$  spectrum with only a small spectral shift (Fig. 4.3), we infer that the weakly electron-binding  $[\text{NM}\cdot(\text{H}_2\text{O})_6]^-$  retains the hydrogen-bond network of the intact  $(\text{H}_2\text{O})_6^-$ . Considering the fact that nitromethane is an aprotic molecule with a dipole moment of 3.46 D, we propose a possible form of  $[\text{NM}\cdot(\text{H}_2\text{O})_6]^-$ ; that is, a *dual dipole-bound* configuration described as

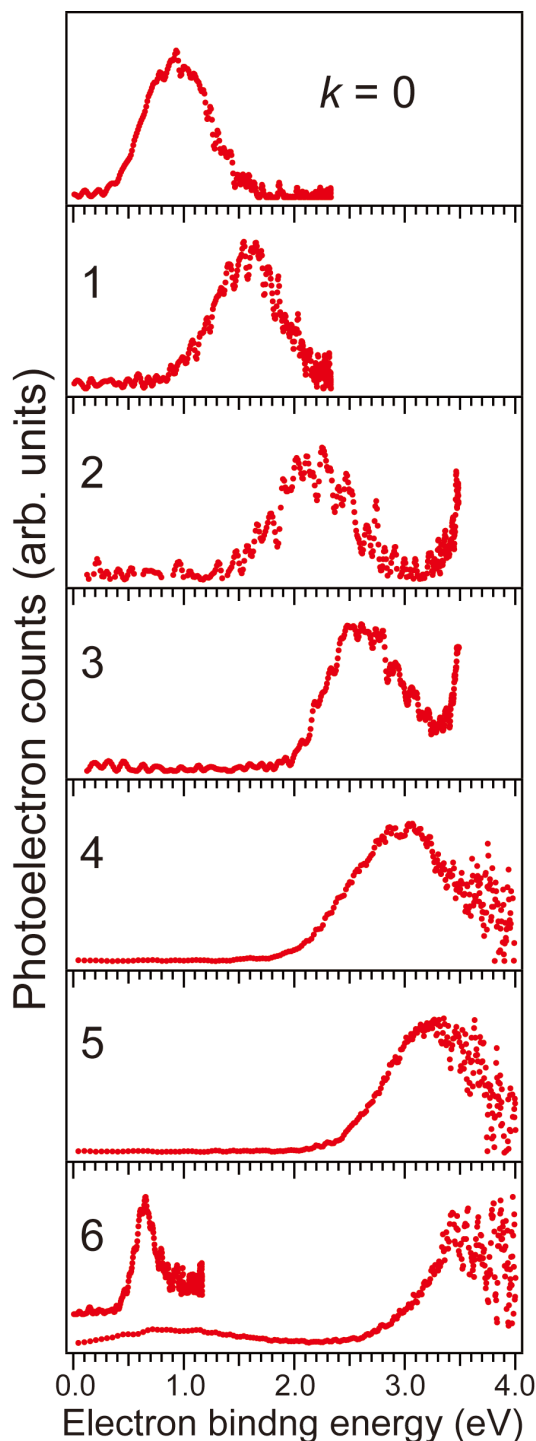


**Figure 4.2** Photoelectron spectra of  $[\text{NM}\cdot(\text{H}_2\text{O})_k]^-$  measured at 532 nm ( $k = 0, 1$ ), 355 nm ( $k = 2, 3$ ), and 266 nm ( $k = 4 - 6$ ). The photoelectron counts are plotted against the electron binding energy,  $\varepsilon_{\text{BE}}$ , defined as  $\varepsilon_{\text{BE}} = h\nu - \varepsilon_{\text{KE}}$ , where  $h\nu$  and  $\varepsilon_{\text{KE}}$  represent the photon energy and the photoelectron kinetic energy, respectively. The  $k = 0 - 3$  spectra were recorded by a VMI photoelectron spectrometer, while  $k = 4 - 6$  by a magnetic-bottle photoelectron spectrometer. The inset represents the  $[\text{NM}\cdot(\text{H}_2\text{O})_6]^-$  spectrum measured at 1064 nm.

**Table 4.1** Vertical detachment energies (VDEs) of  $[\text{NM}\cdot(\text{H}_2\text{O})_k]^-$ 

$k$	VDE (eV)
0	0.94(1) <sup>a</sup>
1	1.57(1)
2	2.18(2)
3	2.62(2)
4	2.97(1)
5	3.24(2)
6	0.65(2), <sup>b</sup> 3.54(6)

<sup>a</sup> Digits in parentheses represent uncertainties estimated from the band-envelop analysis.

<sup>b</sup> VDE for the band appearing in the lower binding energies in the  $k = 6$  spectrum.

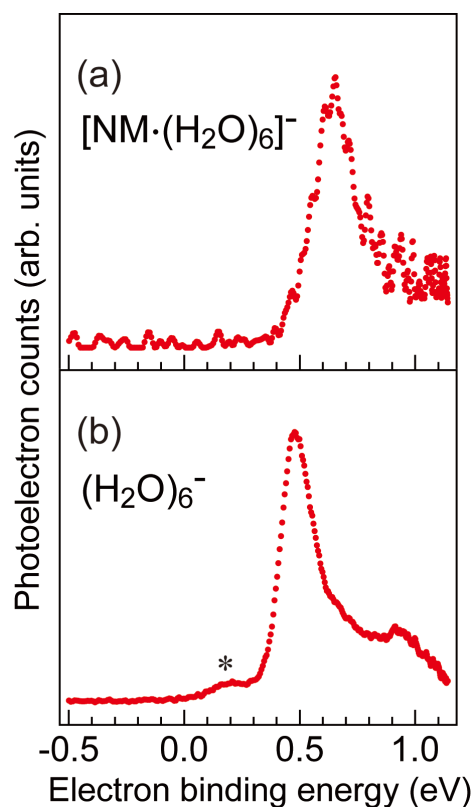
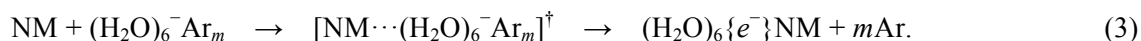


**Figure 4.3** Photoelectron spectra of (a)  $[\text{NM}\cdot(\text{H}_2\text{O})_6]^-$  and (b)  $(\text{H}_2\text{O})_6^-$  recorded at a photon energy of 1.17 eV. Both spectra were recorded by using the VMI photoelectron spectrometer. The hump marked with an asterisk is assigned to isomer I of the photoelectron angular distributions (PADs) were also measured in experiment. The anisotropy parameter,  $\beta$ , was observed to depend slightly on the photoelectron kinetic energy. The averaged  $\beta$  value for each photoelectron band was determined to be  $1.1\pm 0.2$  for  $[\text{NM}\cdot(\text{H}_2\text{O})_6]^-$ , and  $1.0\pm 0.1$  for  $(\text{H}_2\text{O})_6^-$ .

$(\text{H}_2\text{O})_6\{e^-\}\text{NM}$ . Here,  $\{e^-\}$  represents a diffuse electron interacting with both  $(\text{H}_2\text{O})_6$  and NM through attractive electron-dipole interactions. Accordingly,  $\{e^-\}$  can be viewed as a dipole-bound electron for  $(\text{H}_2\text{O})_6$  and, at the same time, also as a dipole-bound electron for NM. The electron trapping scheme proposed here is akin to that operative in  $(\text{HF})_3^-$ , where a dipole-bound anion of  $(\text{HF})_2$  is additionally solvated by another HF monomer at the side of the excess electron to form  $(\text{HF})_2\{e^-\}\text{HF}$ .<sup>38</sup> Note that the  $(\text{H}_2\text{O})_6\{e^-\}\text{NM}$  system differs from  $(\text{HF})_2\{e^-\}\text{HF}$  in that both the constituents,  $(\text{H}_2\text{O})_6$  and NM, possess a large dipole moment intrinsically capable of forming a dipole-bound state.

Although the “dual dipole-bound” scheme awaits a theoretical underpinning by quantum mechanical calculations, a corroborative evidence is given experimentally as follows. In the course of the present experiment, we found that the reaction of  $(\text{H}_2\text{O})_n^- \text{Ar}_m$  with a polar molecule having a large dipole moment, such as acetaldehyde (AA, 2.75 D<sup>22</sup>), acetone (Acn, 2.88 D<sup>22</sup>) and acetonitrile (AN, 3.92 D<sup>22</sup>), also led to the formation of weakly electron-binding forms of  $[\text{M}\cdot(\text{H}_2\text{O})_6]^-$  (M = AA, Acn and AN). The photoelectron spectra of these  $[\text{M}\cdot(\text{H}_2\text{O})_6]^-$  at 1064 nm (not shown here) share characteristics in common with that of  $[\text{NM}\cdot(\text{H}_2\text{O})_6]^-$ ; an  $(\text{H}_2\text{O})_6^-$ -like narrow band with a small spectral shift (0.11 – 0.18 eV) relative to  $(\text{H}_2\text{O})_6^-$ . In Fig. 4.4 shown is the spectral shift, which is defined as  $\Delta\text{VDE} = \text{VDE}([\text{M}\cdot(\text{H}_2\text{O})_6]^-) - \text{VDE}((\text{H}_2\text{O})_6^-)$ , plotted against the magnitude of the dipole moment of the entrained molecule M. As readily seen in Fig. 4.4,  $\Delta\text{VDE}$  increases approximately linearly with the magnitude of dipole moment. Within the context of the dual dipole-bound scheme, the spectral shift is attributed in part to the attractive force exerted between  $\{e^-\}$  and M in the  $(\text{H}_2\text{O})_6\{e^-\}\text{M}$  configuration, and in part to the repulsive force exerted between  $(\text{H}_2\text{O})_6$  and M in the corresponding neutral  $(\text{H}_2\text{O})_6\cdots\text{M}$  prepared by photodetachment. In the latter part, photoejection from  $(\text{H}_2\text{O})_6\{e^-\}\text{M}$  with retaining its geometrical configuration results possibly in an unfavorable “head-on” orientation of two permanent dipoles. The forces at play in  $(\text{H}_2\text{O})_6\{e^-\}\text{M}$  and  $(\text{H}_2\text{O})_6\cdots\text{M}$ , although one is attractive and the other repulsive, tend to increase with increasing polarity of M. This provides a qualitative explanation for the increasing trend of  $\Delta\text{VDE}$  shown in Fig. 4.4.

On the basis of the above considerations, we discuss the formation process of  $(\text{H}_2\text{O})_6\{e^-\}\text{NM}$ . By extending the 1064-nm measurements up to  $k = 8$ , it was revealed that the weakly electron-binding species coexisted in  $[\text{NM}\cdot(\text{H}_2\text{O})_k]^-$  only at  $k = 6$  and 7. It was also found that the formation of the weakly electron-binding species was suppressed almost completely under the reaction conditions that the electron-impact ionized free jet contained predominantly bare  $(\text{H}_2\text{O})_n^-$  reactants. These observations lead us to conclude that the dual dipole-bound anions,  $(\text{H}_2\text{O})_6\{e^-\}\text{NM}$ , are formed via the following Ar-mediated process:



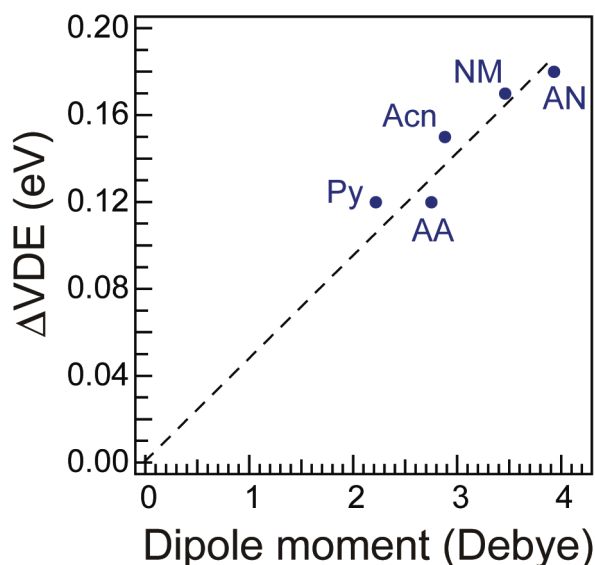


**Figure 4.4** Spectral shift of the  $[M \cdot (H_2O)_6]^-$  photoelectron band relative to  $(H_2O)_6^-$  plotted against the magnitude of the dipole moment of M. M = acetaldehyde (AA), acetone (Acn), nitromethane (NM), and acetonitrile (AN)).

In process (3), the excess energy imparted by the collisional association between NM and  $(H_2O)_6^- Ar_m$  can be dissipated efficiently via the evaporative loss of Ar atoms. The operative energy dissipation is essential to the formation of  $(H_2O)_6\{e^-\}NM$ , where the  $(H_2O)_6$  moiety retains the intact hydrogen-bond network and NM is prepared in an otherwise unstable dipole-bound state by sharing the diffuse excess electron with  $(H_2O)_6$ .

#### 4.3.2 Photostimulated conversion of $(H_2O)_6\{e^-\}NM$ to valence anion

As discussed in the previous section, two types of anionic forms,  $(H_2O)_6\{e^-\}NM$  and  $NM^-(H_2O)_6$ , coexist in  $[NM \cdot (H_2O)_6]^-$  prepared under the present experimental conditions. When  $[NM \cdot (H_2O)_6]^-$  was irradiated by 2.1  $\mu m$  (0.58 eV) photons, both photofragmentation and photodetachment took place competitively. In Fig. 4.5, trace (a) represents the photofragment mass spectrum of  $[NM \cdot (H_2O)_6]^-$  recorded at 2.1  $\mu m$ . The spectrum was obtained by subtracting the photofragment signals measured with laser-off from those with laser-on. The positive-going signal at  $m/e = 115$  corresponds to the production of fragment anions, while the negative-going one at  $m/e = 169$  to the depletion of the parent  $[NM \cdot (H_2O)_6]^-$ . The intensity ratio between two signals was measured to be roughly 1:5, indicating that photodetachment was the dominant process in the 2.1- $\mu m$  photoexcitation.

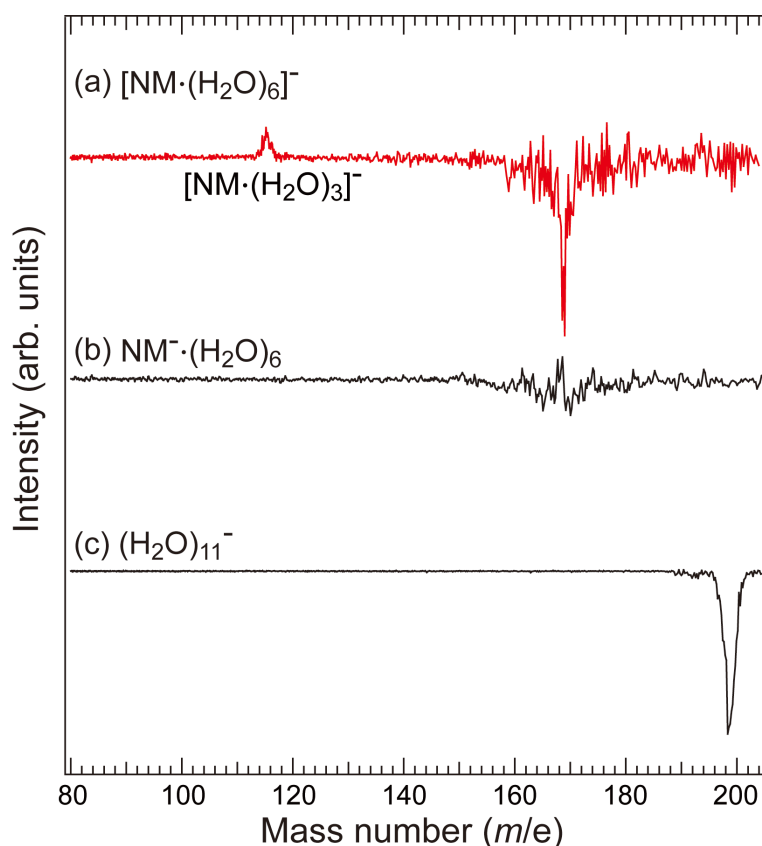
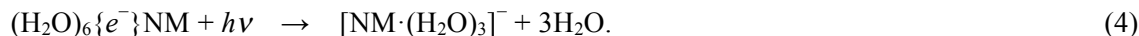


**Figure 4.5** Photofragment mass spectra of (a)  $[\text{NM}\cdot(\text{H}_2\text{O})_6]^-$ , (b)  $\text{NM}^-\cdot(\text{H}_2\text{O})_6$ , and (c)  $(\text{H}_2\text{O})_{11}^-$  recorded at 2.1  $\mu\text{m}$ . The upward peak corresponds to the production of photofragment anions while the downward peaks to the photodepletion of parent anions.

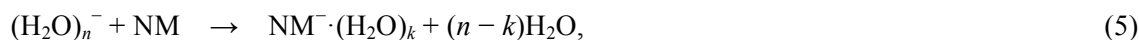
This observation seems consistent with the fact that the excitation energy (0.58 eV) lies within the photoelectron band of  $(\text{H}_2\text{O})_6\{e^-\}\text{NM}$  (see Fig. 4.3(a)).

Although the 2.1- $\mu\text{m}$  photodestruction of  $[\text{NM}\cdot(\text{H}_2\text{O})_6]^-$  proceeds dominantly as photodetachment, we focus our attention on the photofragmentation because this minor channel is peculiar to the  $(\text{H}_2\text{O})_6\{e^-\}\text{NM}$  configuration. This peculiarity is confirmed by the following observations. As shown by trace (b) in Fig. 4.5, neither photofragmentation nor photodepletion was detected when the hydrated anion of nitromethane,  $\text{NM}^-\cdot(\text{H}_2\text{O})_6$ , was irradiated by 2.1- $\mu\text{m}$  photons. In this measurement  $\text{NM}^-\cdot(\text{H}_2\text{O})_6$  was generated via the electron attachment to neutral  $(\text{NM})_M(\text{H}_2\text{O})_N$  clusters; the electronic properties of  $\text{NM}^-\cdot(\text{H}_2\text{O})_6$  was further checked by photoelectron spectroscopy. We also checked that photodetachment was the only decay channel available for bare  $(\text{H}_2\text{O})_n^-$  anions with  $n = 6, 7$ , and 11 by 2.1- $\mu\text{m}$  photoexcitation. As an example, trace (c) in Fig. 4.5 represents the

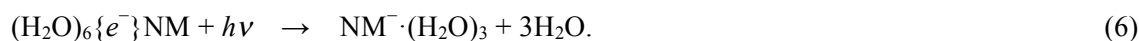
photodepletion spectrum of  $(\text{H}_2\text{O})_{11}^-$ , which possesses VDE of  $0.72 \text{ eV}^2$  slightly larger than that of  $(\text{H}_2\text{O})_6\{e^-\}\text{NM}$ . Hence, we conclude that the  $2.1\text{-}\mu\text{m}$  photofragmentation of  $[\text{NM}\cdot(\text{H}_2\text{O})_6]^-$  proceeds exclusively as



Now we are in position to discuss the chemical identity of the product anion  $[\text{NM}\cdot(\text{H}_2\text{O})_3]^-$  in process (4). In the course of the present study, we also investigated the product anions in the reaction of bare  $(\text{H}_2\text{O})_n^-$  ( $n \geq 6$ ) with NM. The reaction was observed to proceed as



where the number of  $\text{H}_2\text{O}$  molecules lost was roughly determined to be  $3 - 4$  for the  $(\text{H}_2\text{O})_n^-$  reactants with  $n = 6 - 7$ , and  $4 - 5$  for  $n \geq 11$ . The  $\text{NM}^-\cdot(\text{H}_2\text{O})_3$  species was the smallest member of the product anions. These observations are reminiscent of the reactions of  $(\text{H}_2\text{O})_n^-$  with  $\text{M}$  ( $\text{M} = \text{NO}, \text{CO}_2, \text{O}_2$ ),<sup>18-20</sup> where the formation of  $\text{M}^-\cdot(\text{H}_2\text{O})_k$  is accompanied with the evaporative loss of several  $\text{H}_2\text{O}$  molecules; the number of  $\text{H}_2\text{O}$  lost is strongly correlated to the overall reaction exothermicities.<sup>18,19</sup> The present observation on process (5) indicates that the exothermicity of the  $(\text{H}_2\text{O})_n^- + \text{NM} \rightarrow \text{NM}^-\cdot(\text{H}_2\text{O})_n$  reaction is such an amount that  $3 - 5$   $\text{H}_2\text{O}$  molecules are ejected from the hydrated product anion, and that  $\text{NM}^-\cdot(\text{H}_2\text{O})_3$  is rather stable against the  $\text{H}_2\text{O}$  evaporation due possibly to the increasing hydration energy in the small size regime. Comparing this with what we observed in process (4), we can infer more explicitly that the  $2.1\text{-}\mu\text{m}$  photofragmentation of  $(\text{H}_2\text{O})_6\{e^-\}\text{NM}$  proceeds as



Process (6) can be regarded as a photostimulated conversion of the dipole-bound anion to the valence anion of NM,  $\{e^-\}\text{NM} \rightarrow \text{NM}^-$ , followed by ion hydration.

In Fig. 4.6, the overall photofragmentation process of  $(\text{H}_2\text{O})_6\{e^-\}\text{NM}$  is illustrated by the schematic drawing of the relevant potential energy curves. As is the case with a bare nitromethane,<sup>28</sup> the dual dipole-bound  $(\text{H}_2\text{O})_6\{e^-\}\text{NM}$  state is coupled with the valence  $\text{NM}^-\cdot(\text{H}_2\text{O})_6$  state through an electronic interaction, forming the adiabatic potential energy surface of the anion. Along the reaction coordinate connecting the dipole-bound and valence states, there exists a potential barrier which isolates  $(\text{H}_2\text{O})_6\{e^-\}\text{NM}$  from  $\text{NM}^-\cdot(\text{H}_2\text{O})_6$ . This situation differs obviously from the bare nitromethane case, where the potential barrier is rather small such that the dipole-bound anion is readily converted to a valence anion.<sup>25, 27, 28</sup>

This arises possibly from the fact that, in the present system, the reaction coordinate involves not only the distortion of the NM framework, incurred by the accommodation of an excess electron in the LUMO of NM, but also the reconstruction of the hydrogen-bond network of  $(\text{H}_2\text{O})_6$ . The large



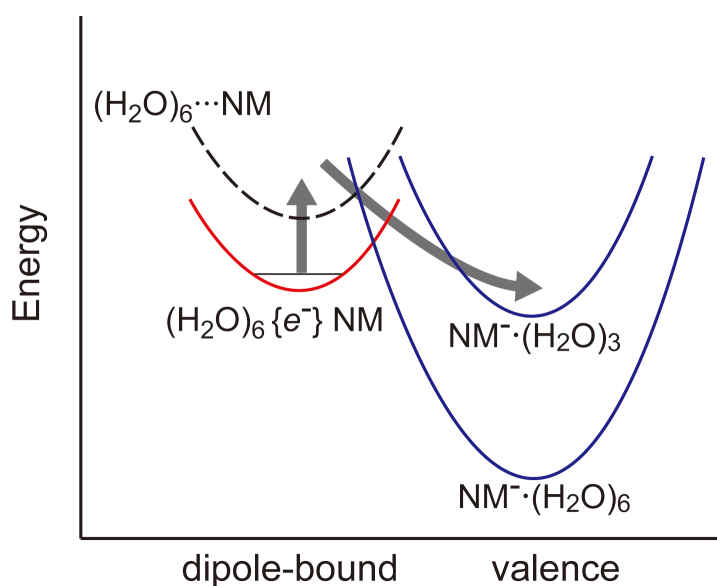


**Figure 4.6** Schematic drawing of the potential energy curves relevant to the photostimulated conversion of the dual dipole-bound anion  $(\text{H}_2\text{O})_6\{e^-\}\text{NM}$  to the hydrated valence anion  $\text{NM}^-\cdot(\text{H}_2\text{O})_6$ .

difference in the equilibrium configuration between  $(\text{H}_2\text{O})_6\{e^-\}\text{NM}$  and  $\text{NM}^-\cdot(\text{H}_2\text{O})_6$  gives rise to the substantial potential barrier along the reaction coordinate. The 2.1- $\mu\text{m}$  photoexcitation of  $(\text{H}_2\text{O})_6\{e^-\}\text{NM}$  corresponds to the electron promotion from the diffuse dipole-bound orbital to a continuum just above the detachment threshold. The resulting upper state can be expressed as  $(\text{H}_2\text{O})_6\cdots\text{NM} + e^-$ , where the nuclear configuration retains the  $(\text{H}_2\text{O})_6\{e^-\}\text{NM}$  geometry while the excess electron now behaves as a “quasi” free electron with very low kinetic energy. The decay process of the  $(\text{H}_2\text{O})_6\cdots\text{NM} + e^-$  system resembles that of a transient intermediate formed in the free electron attachment to  $(\text{H}_2\text{O})_6\cdots\text{NM}$ , where the transition to the valence anionic state competes with the electron ejection.<sup>25</sup> This inference is consistent with the present observation that photofragmentation and photodetachment occur competitively upon the 2.1- $\mu\text{m}$  excitation.

Once the system decays into the valence state, it gains a considerable amount of excess energy due to the large stabilization energy of  $\text{NM}^-\cdot(\text{H}_2\text{O})_6$  relative to the  $(\text{H}_2\text{O})_6\cdots\text{NM} + e^-$  transient. The available excess energy is consumed as the evaporation energy of  $\text{H}_2\text{O}$  molecules during the stabilization process toward  $\text{NM}^-\cdot(\text{H}_2\text{O})_6$ . The exothermicity of this decay process is estimated approximately by  $\Delta H = -\text{EA}(\text{NM}) - E_{\text{hydr}}[\text{NM}^-\cdot(\text{H}_2\text{O})_6]$  by neglecting the weak interactions between  $(\text{H}_2\text{O})_6$  and  $\text{NM}$  as well as the kinetic energy of the excess electron. Here,  $\text{EA}(\text{NM})$  represents the electron affinity of  $\text{NM}$  and  $E_{\text{hydr}}[\text{NM}^-\cdot(\text{H}_2\text{O})_6]$  the hydration energy of  $\text{NM}^-$ . Note that the

exothermicity of the charge transfer followed by ion hydration,  $(\text{H}_2\text{O})_6^- + \text{NM} \rightarrow \text{NM}^-\cdot(\text{H}_2\text{O})_6$ , is formulated as  $\Delta H' = \text{EA}[(\text{H}_2\text{O})_6] - \text{EA}(\text{NM}) - E_{\text{hydr}}[\text{NM}^-\cdot(\text{H}_2\text{O})_6]$ ,<sup>18</sup> where  $\text{EA}[(\text{H}_2\text{O})_6]$  is the adiabatic electron affinities of  $(\text{H}_2\text{O})_6$ . Hence,  $\Delta H - \Delta H' = -\text{EA}[(\text{H}_2\text{O})_6] \approx -0.4 \text{ eV}$ .<sup>13</sup> On this energetic ground, one can expect that the number of  $\text{H}_2\text{O}$  molecules ejected in the  $(\text{H}_2\text{O})_6\{e^-\}\text{NM} + h\nu$  process is larger at least by one than that in  $(\text{H}_2\text{O})_6^- + \text{NM}$ , as the energy required to eject a single  $\text{H}_2\text{O}$  molecule from a hydrated ion is estimated to be  $\approx 0.37 \text{ eV}$  on average for various kinds of anions.<sup>19</sup> It is found, however, in the present study that the photofragmentation of  $(\text{H}_2\text{O})_6\{e^-\}\text{NM}$  leads exclusively to the formation of  $\text{NM}^-\cdot(\text{H}_2\text{O})_3$  possibly because of the distinct stability of  $\text{NM}^-\cdot(\text{H}_2\text{O})_3$  against further ejection of  $\text{H}_2\text{O}$  molecules.

#### 4.4 Summary

We have investigated the reactions of argon-solvated water cluster anions,  $(\text{H}_2\text{O})_n^- \text{Ar}_m$ , with nitromethane ( $\text{CH}_3\text{NO}_2$ ) in a molecular beam containing  $(\text{H}_2\text{O})_6^- \text{Ar}_m$  and  $(\text{H}_2\text{O})_7^- \text{Ar}_m$  as dominant anionic reagents. The central experimental findings in the present study are summarized as follows:

- (1) The reactions yield product anions with the formula  $[\text{CH}_3\text{NO}_2\cdot(\text{H}_2\text{O})_k]^-$ . All the product anions with  $k = 0 - 5$  are identified as the hydrated valence anions of nitromethane,  $\text{CH}_3\text{NO}_2^-\cdot(\text{H}_2\text{O})_k$ , by photoelectron spectroscopy.
- (2) Photoelectron spectrum of  $[\text{CH}_3\text{NO}_2\cdot(\text{H}_2\text{O})_6]^-$  consists of two band components located at the electron binding energies of 0.65 and 3.54 eV, indicating the coexistence of two types of anionic forms in  $[\text{CH}_3\text{NO}_2\cdot(\text{H}_2\text{O})_6]^-$ . The high-energy band is ascribed to the hydrated valence anion,  $\text{CH}_3\text{NO}_2^-\cdot(\text{H}_2\text{O})_6$ . The low-energy band (VDE =  $0.65 \pm 0.02 \text{ eV}$ ) is almost identical to the  $(\text{H}_2\text{O})_6^-$  band in shape except for the spectral shift of  $\approx 0.17 \text{ eV}$  toward higher binding energies. This is a strong indication that the weakly electron-binding form of  $[\text{CH}_3\text{NO}_2\cdot(\text{H}_2\text{O})_6]^-$  possesses a dipole-bound nature with retaining the hydrogen-bond network of  $(\text{H}_2\text{O})_6^-$  as a structural motif.
- (3) Photoexcitation of the weakly electron-binding form of  $[\text{CH}_3\text{NO}_2\cdot(\text{H}_2\text{O})_6]^-$  at  $2.1 \mu\text{m}$  (0.58 eV) results in the appreciable depletion of the anion population:  $\approx 80\%$  of the depletion is due to photodetachment and the rest to fragmentation into the  $\text{CH}_3\text{NO}_2^-\cdot(\text{H}_2\text{O})_3 + 3\text{H}_2\text{O}$  channel.

From the above experimental findings together with several collateral experimental observations, we have drawn the following conclusions regarding the formation and properties of the weakly electron-binding form of  $[\text{CH}_3\text{NO}_2\cdot(\text{H}_2\text{O})_6]^-$ :

- (i) The weakly electron-binding species can be identified as a *dual dipole-bound* anion represented as  $(\text{H}_2\text{O})_6\{e^-\}\text{CH}_3\text{NO}_2$ . In the dual dipole-bound configuration, the  $(\text{H}_2\text{O})_6$  and  $\text{CH}_3\text{NO}_2$  moieties, retaining their neutral conformations, share the excess electron through weak

electron-dipole interactions.

- (ii) The dual dipole-bound anion is generated via the “Ar-mediated” process,  $\text{CH}_3\text{NO}_2 + (\text{H}_2\text{O})_6^- \text{Ar}_m \rightarrow (\text{H}_2\text{O})_6\{e^-\}\text{CH}_3\text{NO}_2 + m\text{Ar}$ , where the sequential evaporation of Ar atoms effectively quenches an otherwise unstable reaction intermediate formed halfway through the charge transfer reaction,  $\text{CH}_3\text{NO}_2 + (\text{H}_2\text{O})_n^- \rightarrow \text{CH}_3\text{NO}_2^-\cdot(\text{H}_2\text{O})_m + (n - m)\text{H}_2\text{O}$ .

Thus, by using an Ar-mediated approach, we have demonstrated the formation of a new type of anion, which corresponds to the intermediate species formed in the early stage of the charge transfer reaction between  $(\text{H}_2\text{O})_n^-$  and  $\text{CH}_3\text{NO}_2$ . The dual dipole-bound nature of the anion allows us to access optically to the continuum state composed of  $(\text{H}_2\text{O})_6$ ,  $\text{CH}_3\text{NO}_2$  neutrals and slow  $e^-$ , where they are spatially close to each other and, consequently, ready to play the second half of the charge transfer process. This means that we can photoinitiate the charge transfer reaction, which opens up new possibility for conducting transient spectroscopy of the  $\text{M} + (\text{H}_2\text{O})_n^-$  collision systems.

## References

- 1 Coe, J. V.; Lee, G. H.; Eaton, J. G.; Arnold, S. T.; Sarkas, H. W.; Bowen, K. H.; Ludewigt, C.; Haberland, H.; Worsnop, D. R. *J. Chem. Phys.* **1990**, *92*, 3980–3982.
- 2 Kim, J.; Becker, I.; Cheshnovsky, O.; Johnson, M. A. *Chem. Phys. Lett.* **1998**, *297*, 90–96.
- 3 Verlet, J.; Bragg, A. E.; Kammrath, A.; Cheshnovsky, O.; Neumark, D. M. *Science* **2005**, *307*, 93–96.
- 4 Hammer, N. I.; Shin, J.-W.; Headrick, J. M.; Diken, E. G.; Roscioli, J. R.; Weddle, G. H.; Johnson, M. A. *Science* **2004**, *306*, 675–679.
- 5 Hammer, N. I.; Roscioli, J. R.; Johnson, M. A. *J. Phys. Chem. A* **2005**, *109*, 7896–7901.
- 6 Hammer, N. I.; Roscioli, J. R.; Johnson, M. A.; Myshakin, E. M.; Jordan, K. D. *J. Phys. Chem. A* **2005**, *109*, 11526–11530.
- 7 Roscioli, J. R.; Hammer, N. I.; Johnson, M. A. *J. Phys. Chem. A* **2006**, *110*, 7517–7520.
- 8 Roscioli, J. R.; Johnson, M. A. *J. Chem. Phys.* **2007**, *126*, 024307
- 9 Roscioli, J. R.; Hammer, N. I.; Johnson, M. A.; Diri, K.; Jordan, K. D. *J. Chem. Phys.* **2008**, *128*, 104314.
- 10 Bragg, A. E.; Verlet, J.; Kammrath, A.; Cheshnovsky, O.; Neumark, D. M. *Science* **2004**, *306*, 669–671.
- 11 Bragg, A. E.; Verlet, J.; Kammrath, A.; Cheshnovsky, O.; Neumark, D. M. *J. Am. Chem. Soc.* **2005**, *127*, 15283–15295.
- 12 Paik, D. H.; Lee, I.-R.; Yang, D.-S.; Baskin, J. S.; Zewail, A. H. *Science* **2004**, *306*, 672–675.
- 13 Lee, H. M.; Suh, S. B.; Tarakeshwar, P.; Kim, K. S. *J. Chem. Phys.* **2005**, *122*, 044309.
- 14 Sommerfeld, T.; Gardner, S. D.; DeFusco, A.; Jordan, K. D. *J. Chem. Phys.* **2006**, *125*, 174301.
- 15 Herbert, J. M.; Head-Gordon, M. *J. Am. Chem. Soc.* **2006**, *128*, 13932–13939.
- 16 Tsurusawa, T.; Iwata, S. *Chem. Phys. Lett.* **2000**, *315*, 433–440.
- 17 Yagi, K.; Okano, Y.; Sato, T.; Kawashima, Y.; Tsuneda, T.; Hirao, K. *J. Phys. Chem. A*, **2008**, *112*, 9845–9853.
- 18 Posey, L. A.; Deluca, M. J.; Campagnola, P. J.; Johnson, M. A. *J. Phys. Chem.* **1989**, *93*, 1178–1181.
- 19 Arnold, S. T.; Morris, R. A.; Viggiano, A. A.; Johnson, M. A. *J. Phys. Chem.* **1996**, *100*, 2900–2906.
- 20 Balaj, O. P.; Siu, C.-K.; Balteanu, I.; Beyer, M. K.; Bondybey, V. E. *Int. J. Mass Spectrom.* **2004**, *238*, 65–74.
- 21 McCunn, L. R.; Headrick, J. M.; Johnson, M. A. *Phys. Chem. Chem. Phys.* **2008**, *10*, 3118–3123.
- 22 *CRC Handbook of Chemistry and Physics*, 74th ed., edited by Lide, D. R. (CRC press, 1993).

- 23 Desfrancois, C.; Abdoul-Carmine, H.; Khelifa, N.; Schermann, J. P. *Phys. Rev. Lett.* **1994**, *73*, 2436–2439.
- 24 Adams, C. L.; Schneider, H.; Ervin, K. M.; Weber, J. M. *J. Chem. Phys.* **2009**, *130*, 074307.
- 25 Compton, R. N.; Carman, H. S.; Desfrancois, C.; Abdoul-Carmine, H.; Schermann, J. P.; Hendricks, J. H.; Lyapustina, S. A.; Bowen, K. H., Jr. *J. Chem. Phys.* **1996**, *105*, 3472–3478.
- 26 Gutsev, G. L.; Bartlett, R. J. *J. Chem. Phys.* **1996**, *105*, 8785–8792.
- 27 Lecomte, F.; Carles, S.; Desfrancois, C.; Johnson, M. A. *J. Chem. Phys.* **2000**, *113*, 10973–10977.
- 28 Sommerfeld, T. *Phys. Chem. Chem. Phys.* **2002**, *4*, 2551–2516.
- 29 Stokes, S. T.; Bowen, K. H., Jr.; Sommerfeld, T.; Ard, S.; Mirsaleh-Kohan, N.; Steill, J. D.; Compton, R. N. *J. Chem. Phys.* **2008**, *129*, 064308.
- 30 Tsukuda, T.; Saeki, M.; Iwata, S.; Nagata, T. *J. Phys. Chem. A* **1997**, *101*, 5103–5110.
- 31 Nakanishi, R.; Muraoka, A.; Nagata, T. *Chem. Phys. Lett.* **2006**, *427*, 56–61.
- 32 Johnson, M. A.; Lineberger, M. A. in *Techniques of Chemistry*, edited by Farrar J. M.; Saunders W. H. (Wiley, New York, 1988), Vol. 20, p. 591.
- 33 Eppink, A. T. J. B.; Parker, D. H. *Rev. Sci. Instrum.* **1997**, *68*, 3477–3484.
- 34 Dribinski, V.; Ossadtchi, A.; Mandelstam, V. A.; Reisler, H. *Rev. Sci. Instrum.* **2002**, *73*, 2634–2642.
- 35 Travers, M. J.; Cowles, D. C.; Ellison, G. B. *Chem. Phys. Lett.* **1989**, *164*, 449–455.
- 36 Arnold, D. W.; Bradforth, S. E.; Kim, E. H.; Neumark, D. M. *J. Chem. Phys.* **1995**, *102*, 3510–3518.
- 37 Tsukuda, T.; Saeki, M.; Kimura, R.; Nagata, T. *J. Chem. Phys.* **1999**, *110*, 7846–7875.
- 38 Gutowski, M.; Hall, C.; Adamowicz, L.; Hendricks, J.; de Clercq, H.; Lyapustina, S.; Nilles, J.; Xu, S. J.; Bowen, K. H., Jr. *Phys. Rev. Lett.* **2002**, *88* (14), 143001.



## Chapter 5

# Photoelectron spectroscopy of acetone cluster anions, $[(\text{CH}_3)_2\text{CO}]_n^-$ ( $n = 2, 5 - 15$ )

### ABSTRACT

Photoelectron images of  $[(\text{CH}_3)_2\text{CO}]_n^-$  ( $n = 2, 5-15$ ) were recorded at 3.49 eV. Analysis of the images provided the vertical detachment energies (VDEs) and photoelectron angular distributions (PADs) of  $[(\text{CH}_3)_2\text{CO}]_n^-$ . The  $n$ -dependence of these quantities starts with  $\text{VDE} = 0.83 \pm 0.03$  eV and  $\beta \approx 0.3$  at  $n = 2$ , and it ends up with  $2.83 \pm 0.03$  eV and  $\approx 0.1$  at  $n = 15$ . These findings, in conjunction with ab initio results, indicate: (1) the formation of a specific anion structure at  $n = 2$ ; and (2) the presence of a solvent-stabilized  $(\text{CH}_3)_2\text{CO}^-$  valence anion in the larger analogues.

This chapter has been reproduced in part with permission from the following previously published article: Nakanishi, R.; Muraoka, A.; Nagata, T. *Chemical Physics Letters* 2006, 427, 56-61. DOI:10.1016/j.cplett.2006.06.061 Copyright 2006 Elsevier

## 5.1 Introduction

The anion of acetone ( $(\text{CH}_3)_2\text{CO} = \text{Acn}$ ) has long been a target of many experimental and theoretical investigations as a typical example of aliphatic ketyl radical anions in condensed phases. They are formed in the reaction of hydrated electrons with acetone, which acts as an efficient electron scavenger.<sup>1</sup> Electron spin resonance (ESR) spectroscopy in solution<sup>2</sup> and in rare gas matrices<sup>3</sup> have revealed that  $(\text{Acn})^-$  is pyramidal in shape at the  $\alpha$  carbon. A theoretical calculation has also predicted a pyramidal geometry as the most stable structure of  $(\text{Acn})^-$ , where the excess electron is accommodated in the  $\pi_{\text{CO}}^*$  antibonding orbital.<sup>4</sup> On the other hand, the valence state anion of acetone in the gas phase is unstable relative to autodetachment<sup>5</sup>;  $(\text{Acn})^-$  is formed only as a “dipole-bound” anion, where the excess electron is captured in the electrostatic field induced by the dipole moment of acetone (2.88 D).<sup>6</sup> Thus, the electron trapping mechanism of acetone is definitely phase-dependent.

This invokes a naive question regarding the electronic properties of acetone cluster anions,  $(\text{Acn})_n^-$ : whether a valence anion is formed in  $(\text{Acn})_n^-$  or whether  $(\text{Acn})_n^-$  contains a solvated electron surrounded by multi-dipoles, and whether or not these situations depend on the cluster size. There have been several experiments conducted in the same context for cluster systems other than  $(\text{Acn})_n^-$ ; coexistence of two forms of cluster anions, one involving valence anions and the other solvated electrons, is observed at certain sizes in pyridine<sup>7</sup>, acetonitrile<sup>8</sup>, and formamide<sup>9</sup> cluster anions.

In the present study, the electronic properties of  $(\text{Acn})_n^-$  with  $n = 2, 5 - 15$  are probed by photoelectron imaging spectroscopy. From the observed photoelectron images, we have determined the VDEs and the PADs as a function of the cluster size. The discussion on these experimental findings with the aid of ab initio calculations has provided information on the geometrical structures and electronic properties of  $(\text{Acn})_n^-$  prepared in our cluster beam.

## 5.2 Experimental

The experimental apparatus consists of a negative ion source, a collinear tandem time-of-flight (TOF) mass spectrometer and a photoelectron spectrometer. An electron-impact ionized free jet<sup>10</sup> was used to generate  $(\text{Acn})_n^-$  clusters. The sample gas was prepared by passing neat Ar through a reservoir containing acetone at 20 °C and expanded through a pulsed nozzle (General Valve 9-279-900) with a stagnation pressure of  $\approx 1$  atm. The free jet was then crossed with a 250-eV electron beam at the expansion region, which resulted in the production of secondary slow electrons. Neutral acetone clusters existing in the free jet captured the slow electrons to form  $(\text{Acn})_n^-$  clusters. The cluster anions thus produced were extracted into the TOF mass spectrometer by applying a



1.25-kV electric pulse. After mass selection by a pulsed beam deflector, the anions of interest were admitted into the photoelectron chamber and then intersected with the third harmonic (355 nm) of a Nd:YAG laser (Quanta-Ray GCR130). The laser fluence was kept below  $5 \text{ mJ pulse}^{-1} \text{ cm}^{-2}$ . The velocity and angular distributions of photoelectrons were measured by a velocity-map imaging (VMI) photoelectron spectrometer<sup>11</sup> having a 17-cm long electron flight tube shielded by  $\mu$ -metal. The photoelectrons were accelerated up to 640 eV perpendicular to both the ion and laser beams in a static electric field and then projected onto a 40-mm diameter dual microchannel plate (MCP) coupled to a P20 phosphor screen (Photek VID-240). The acceleration field was applied by three-electrode lens optimized for the velocity-map focusing condition.<sup>11</sup> In order to reduce a background noise, the MCP was gated with a 200-ns time window coincident with the photoelectron arrival. Photoelectron images on the phosphor screen were recorded by a CCD camera (Apogee AP7p, 512×512 pixels) and processed by a personal computer.

The photoelectron images presented in this chapter were acquired typically for 10,000 – 40,000 laser shots. The observed raw images were reconstructed into three-dimensional velocity distributions using the basis set expansion (BASEX) method developed by Reisler et al.<sup>12</sup> The measured electron kinetic energy ( $\epsilon_{\text{KE}}$ ) was calibrated against the known photoelectron band of  $\Gamma^-$ .<sup>13</sup> A spectral resolution of  $\approx 40 \text{ meV}$  was achieved at the photoelectron kinetic energy of 500 meV after the reconstruction procedure.

## 5.3 Results and discussion

### 5.3.1 Mass spectra

Figure 5.1 shows a typical mass spectrum of anions formed in the electron-impact ionized free jet. The smallest  $(\text{Acn})_n^-$  detected is the pentamer anion,  $(\text{Acn})_5^-$ . Smaller members,  $n < 5$ , were not observed via ionization of acetone/Ar gas mixture under various beam conditions. The onset of the size distribution was always observed at  $n = 5$ , although the overall mass distribution was found to depend on the stagnation pressure, the duration of the pulsed beam and the distance between the nozzle and the electron beam. However, the  $(\text{Acn})_2^-$  anion was accidentally observed, as shown in the inset of Fig. 5.1, in the course of preparing  $[(\text{Acn})_n(\text{H}_2\text{O})_m]^-$  anions under a completely different beam condition, where the concentration of acetone in the sample gas was cut down to  $< 3 \%$  and in the presence of a trace amount of water. Even in this beam condition,  $(\text{Acn})_n^-$  with  $n = 3$  and 4 were not detected in the spectrum. It is also notable that  $[(\text{Acn})_1(\text{H}_2\text{O})_4]^-$  was the smallest member observed in the  $[(\text{Acn})_1(\text{H}_2\text{O})_m]^-$  series. This is consistent with the recent observation by Bondybey et al., who detected  $(\text{Acn})^-(\text{H}_2\text{O})_4$  as the final product in the gas-phase reaction of  $(\text{H}_2\text{O})_n^-$  with acetone in their FT-ICR mass spectrometer.<sup>14</sup> We have carefully confirmed the mass assignments by

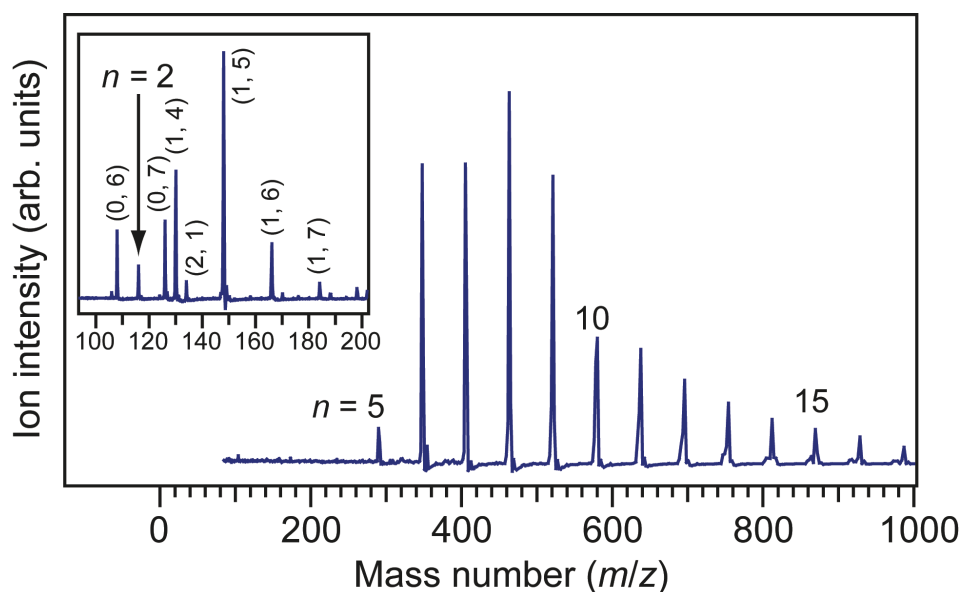


**Figure 5.1** Typical mass spectrum of  $(\text{Acn})_n^-$  produced in the electron-impact ionized jet of an acetone/Ar mixture. Also shown in the inset is the spectrum of  $[(\text{Acn})_n(\text{H}_2\text{O})_m]^-$ . The formula  $[(\text{Acn})_n(\text{H}_2\text{O})_m]^-$  is abbreviated as  $(n, m)$ .

replacing acetone ( $m/z = 58$ ) with acetone- $d_6$  ( $m/z = 64$ ) in the sample gas.

Considering the onset of the size distribution of  $(\text{Acn})_n^-$  observed at  $n = 5$ , together with the formation of  $(\text{Acn})^-(\text{H}_2\text{O})_4$  in the reaction between  $(\text{H}_2\text{O})_n^-$  and acetone,<sup>14</sup> we infer that at least four polar solvent molecules are necessary to stabilize an acetone monomer anion regardless of the type of solvent. In other words, one acetone molecule accommodates the excess electron and the remaining four molecules serve as solvents in  $(\text{Acn})_5^-$ .

The appearance of  $(\text{Acn})_2^-$  despite the absence of  $(\text{Acn})_n^-$  ( $n = 3, 4$ ) in the  $[(\text{Acn})_n(\text{H}_2\text{O})_m]^-$  spectrum indicates the formation of a specific structure for  $(\text{Acn})_2^-$ , where the excess electron is trapped in a different manner from that for the anions with  $n \geq 5$ . We will discuss this feature in conjunction with the results of photoelectron spectroscopy and ab initio calculations in later sections.

### 5.3.2 Photoelectron spectra

Figure 5.2(a) depicts the photoelectron images of  $(\text{Acn})_n^-$  ( $n = 2, 5 - 15$ ) reconstructed by the BASEX method. The images have common features: a bright spot at the center of the image and a ring with a larger radius. The spot corresponds to slow electrons characteristic of autodetachment

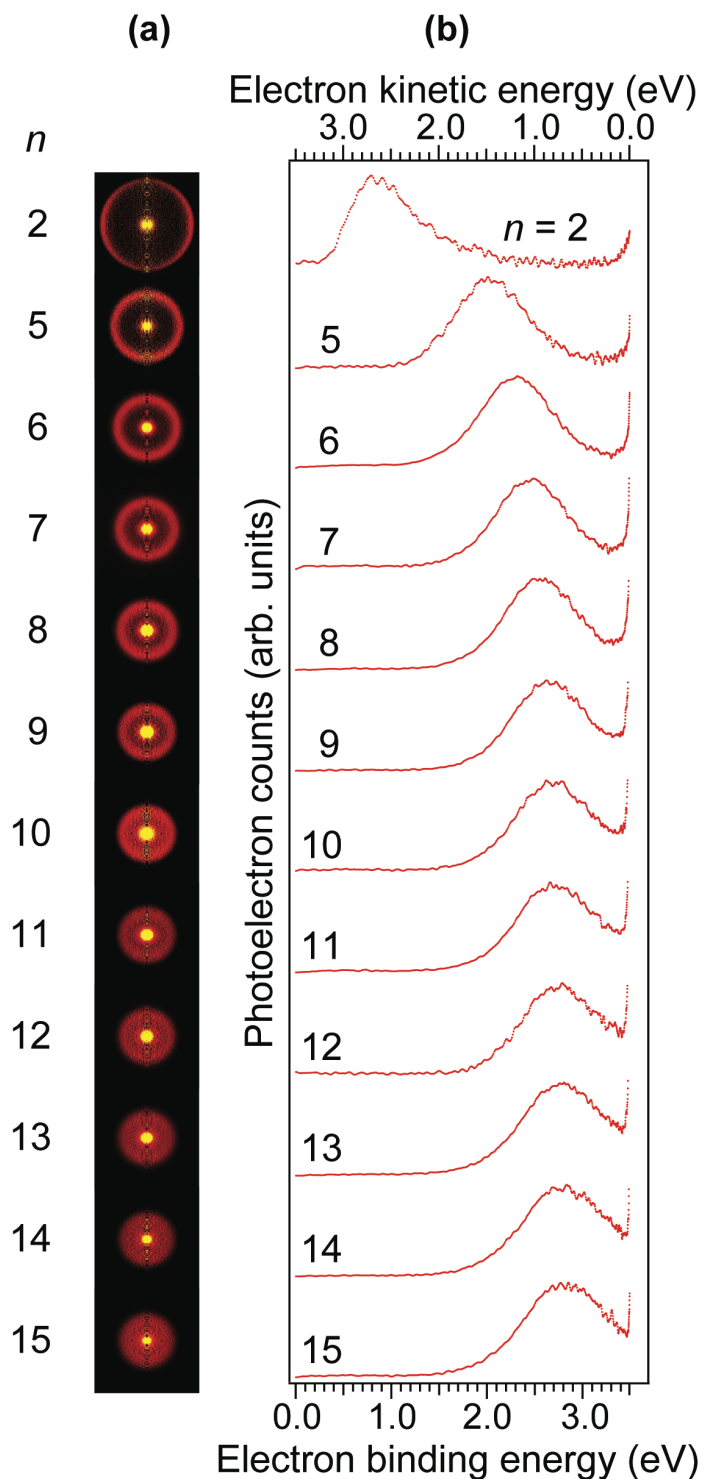


**Figure 5.2** (a) Reconstructed photoelectron images and (b) corresponding photoelectron spectra of  $(\text{Acn})_n^-$  ( $n = 2, 5 - 15$ ) measured at 3.49 eV. The laser polarization vector lies vertical in the figure plane. All the images are displayed in an arbitrary but uniform velocity scale.

from the excited states of anions.<sup>15</sup> The ring corresponds to electrons with higher  $\epsilon_{KE}$  ejected by direct photodetachment, with which we are concerned in the present study. The radius of the ring decreases gradually with the cluster size, indicating that the velocity of the photoelectron decreases with the size due to the increasing photodetachment threshold energy.

In Fig. 5.2(b) are shown the conventional photoelectron spectra deduced from the images by integration over the angular variable; the photoelectron counts are plotted against the electron binding energy,  $\epsilon_{BE}$ , defined as  $\epsilon_{BE} = h\nu - \epsilon_{KE}$ , where  $h\nu$  is the photon energy. Each spectrum consists of a structureless broad band along with a sharp rise in the  $\epsilon_{BE} > 3.3\text{eV}$  region. The position of the broad band shifts toward higher energies as the cluster size is increased, whereas the sharp rise does not change their positions with the cluster size. The  $n$ -independent behavior of the sharp rise gives a strong indication that the signal arises from autodetachment, but a more detailed discussion is outside of our scope in the present study.

The electron binding energy at the maximum of each photoelectron band corresponds to the VDE of the cluster anion. The VDE takes a value of  $0.83 \pm 0.03$  eV at  $n = 2$ , increases significantly at  $n = 5$  ( $2.05 \pm 0.03$  eV) and then gradually increases up to  $2.83 \pm 0.03$  eV at  $n = 15$ . They are plotted against the cluster size in Fig. 5.3(a), and the exact values are listed in Table 2.1. These VDE values lie in the range expected either for valence anions or for those stabilized by solvation. As for the anions with  $5 \leq n \leq 15$ , the observed VDE increment ( $0.02 - 0.26$  eV) with each additional acetone molecule is ascribable to the stabilization of the ground-state anion by ion-molecule interactions. Hence, we conclude that an identical anionic core is formed in  $(\text{Acn})_n^-$  with  $5 \leq n \leq 15$ . As for the  $n = 2$  anion, a different type of anion formation operates; see Sec. 5.3.4.

### 5.3.3 Photoelectron angular distributions

The angular distributions are also deducible from the photoelectron images shown in Fig. 5.2(a). In general, the PADs are expressed as

$$I(\theta) \propto 1 + \beta P_2(\cos \theta), \quad (1)$$

where  $\beta$  represents the anisotropy parameter,  $\theta$  the angle between the photoelectron velocity vector and the laser polarization vector, and  $P_2(\cos\theta)$  the second-order Legendre polynomial. An analysis of the images has revealed that  $\beta$  depends slightly on  $\epsilon_{KE}$ . The  $\bar{\beta}$  values listed in Table 1 are those determined from the photoelectron images by averaging  $\beta$  over  $\epsilon_{KE}$  in the photoelectron band. It is apparent that  $\bar{\beta}$  is almost independent of the cluster size in the range of  $5 \leq n \leq 15$  with a value of  $\approx 0.1$ . On the other hand,  $\bar{\beta}$  is determined to be  $-0.32$  for  $n = 2$ . We also found that  $\beta$  in the  $\epsilon_{BE} > 3.3$  eV region is essentially zero for all the spectra, which reinforces the above argument on the autodetachment. Although PAD is closely related to the symmetry properties of the orbital from

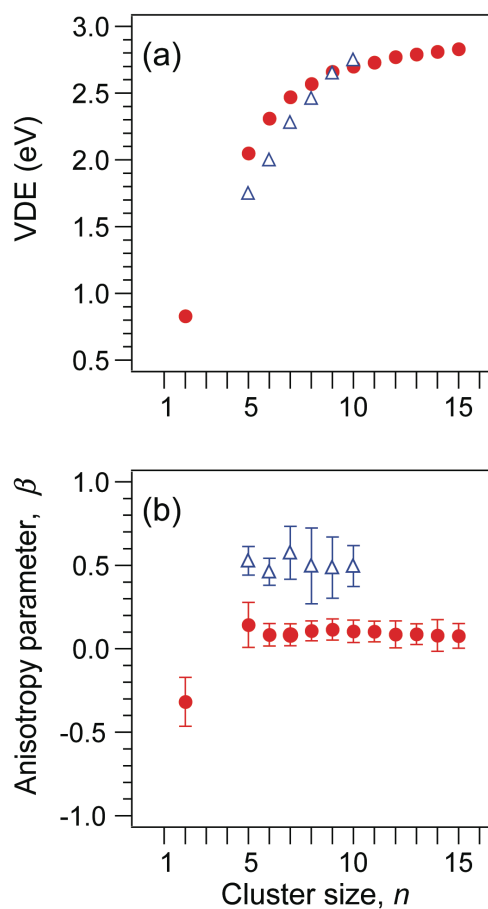


**Figure 5.3** (a)VDE and (b)  $\bar{\beta}$  as a function of the cluster size. Solid symbols are the data points for  $(\text{Acn})_n^-$ , while open symbols for  $(\text{Acn})^-(\text{H}_2\text{O})_{n-1}$ .

**Table 5.1** VDEs and averaged anisotropy parameter,  $\bar{\beta}$ , of  $(\text{Acn})_n^-$ .

Cluster Size, $n$	VDE (eV) <sup>a</sup>	$\bar{\beta}$ <sup>b</sup>
2	0.83	-0.32
5	2.05	0.14
6	2.31	0.08
7	2.47	0.08
8	2.57	0.11
9	2.66	0.12
10	2.70	0.11
11	2.73	0.10
12	2.77	0.09
13	2.79	0.09
14	2.81	0.08
15	2.83	0.08

<sup>a</sup> Uncertainty assessed to each VDE value is  $\pm 0.03$  eV.

<sup>b</sup> Determined by averaging  $\beta$  over  $\epsilon_{\text{BE}}$  within the photoelectron band (see text).

which electron ejection takes place, a quantitative interpretation of the resultant  $\beta$  value is rather complicated, especially for polyatomic molecular systems.<sup>16</sup> Here, we infer from the present PAD results that the electronic properties of the  $n = 2$  anion differ evidently from those of  $(\text{Acn})_n^-$  with  $5 \leq n \leq 15$  at the molecular-orbital level.

The following discussion lead us to conclude that the ion core in  $(\text{Acn})_n^-$  with  $5 \leq n \leq 15$  is the valence anion of acetone monomer,  $(\text{Acn})^-$ . Recently, Mabbs et al. investigated the solvent effect on the PADs in the photodetachment of monosolvated iodide cluster anions, such as  $\Gamma^- \cdot \text{Ar}$ ,  $\Gamma^- \cdot \text{H}_2\text{O}$ ,  $\Gamma^- \cdot \text{CH}_3\text{CN}$  and  $\Gamma^- \cdot \text{CH}_3\text{I}$ .<sup>17</sup> As for  $\Gamma^- \cdot \text{Ar}$ ,  $\Gamma^- \cdot \text{H}_2\text{O}$  and  $\Gamma^- \cdot \text{CH}_3\text{CN}$ , they found a reasonable agreement between the experimental observations and theoretical predictions by using variants of the Cooper-Zare central-potential model for the photodetachment of atomic anions,<sup>18, 19</sup> where the electron-dipole interactions between the ejected electron and the residual neutral are semiquantitatively taken into account.<sup>20</sup> In the  $\Gamma^- \cdot \text{CH}_3\text{I}$  case, however, an anomalous lack of photodetachment anisotropy was observed. They eventually attributed the nearly isotropic PAD in the  $\Gamma^- \cdot \text{CH}_3\text{I}$  photodetachment to the electron scattering by the solvent, because the kinetic energy of the ejected electrons from  $\Gamma^- \cdot \text{CH}_3\text{I}$  in their experiment lies in the region of  $\approx 1$  eV, where a shape resonance exists in the  $\text{CH}_3\text{I} + e$  scattering process.<sup>21</sup>

By applying their argument extendedly to a “multisolvated” molecular anion, we infer that photodetachment anisotropy can be diminished significantly in the presence of acetone molecules around the anionic core, because the  $\text{Acn} + e$  scattering process shows a negative-ion resonance starting at  $\approx 0.7$  eV with a maximum at  $\approx 1.2$  eV.<sup>5</sup> Also inferred admittedly from the intrinsic nature of negative-ion resonance is that the electron scattering by solvent molecules simply reduces the magnitude of photodetachment anisotropy but hardly changes the sign of the  $\beta$  value: the scattered electrons eventually lose the memory of their incident directions due to the formation of a temporary negative-ion state in the course of resonance scattering. Hence, we conclude from the  $\bar{\beta}$  values plotted in Fig. 5.3(b) that *the anionic core in  $(\text{Acn})_n^-$  intrinsically exhibits PAD with a positive value of  $\beta$ , which is reduced to  $\approx 0.1$  by the solvation.*

For identification of the anionic core in  $(\text{Acn})_n^-$ , we have measured the photoelectron spectra of  $(\text{Acn})^-(\text{H}_2\text{O})_{n-1}$  ( $n = 5 - 10$ ), in which the valence anion of acetone monomer is formed as the ion core stabilized by  $(n-1)\text{H}_2\text{O}$  solvent molecules. Because no evidence for a negative-ion resonance is observed in the  $\text{H}_2\text{O} + e$  scattering process below 6 eV,<sup>22</sup> a less-diminishing photodetachment anisotropy is expected for  $(\text{Acn})^-(\text{H}_2\text{O})_{n-1}$ . The measurement has revealed that the  $(\text{Acn})_n^-$  and  $(\text{Acn})^-(\text{H}_2\text{O})_{n-1}$  spectra show a nearly identical spectral profile, except for the notable difference in spectral positions due to their different VDEs. As shown in the  $\bar{\beta}$  values for  $(\text{Acn})^-(\text{H}_2\text{O})_{n-1}$  and  $(\text{Acn})_n^-$  compared in Fig. 5.3, the former  $\bar{\beta}$  values are systematically larger than the latter, which agrees with our expectations. In view of the close similarity in their spectral profiles and the

expected behavior in the solvent dependence of  $\bar{\beta}$ , we conclude that  $(\text{Acn})^-$  plays a significant role as the anionic core in  $(\text{Acn})_n^-$  with  $5 \leq n \leq 15$ . It then follows that  $(\text{Acn})_2^-$ , whose PAD is characterized by a *negative*  $\beta$  value, takes on a specific form of anion rather than an  $(\text{Acn})^- \cdot (\text{Acn})$  ion-molecule complex.

### 5.3.4 Structures of $(\text{Acn})_n^-$

Ab initio calculations by Fourré et al. predict the radical anion of acetone has a pyramidal structure, where the C=O bond is bent out of the plane containing three C atoms by  $37.3^\circ$ .<sup>4</sup> According to their MP2/6-311G\*\* calculation, the anionic state is located 2.0 eV above the neutral ground state. The excess electron mainly occupies the  $\pi_{\text{CO}}^*$  orbital and is predominantly localized on the C atom of the carbonyl group. In the present study, we first traced their calculations with a higher level of theory: we performed the geometry optimization at the MP2/6-311+G\*\* level, and then calculated the total energy at the CCSD(T)/6-311+G\*\* level with the geometry optimized at the MP2 calculations. The geometry of the monomer anion that we have obtained (Fig. 5.4(a)) is almost identical with that given by Fourré et al. The anionic state is located 1.3 eV above the neutral ground state. The VDE, evaluated by subtracting the total energy of the anion from that of the neutral having the equilibrium geometry of the anion, is  $-0.59$  eV, indicating that the monomer anion of acetone is unstable against autodetachment. These ab initio results are consistent with our inference that  $(\text{Acn})_n^-$  ( $n \geq 5$ ) species are formed via the stabilization of an otherwise unstable  $(\text{Acn})^-$  by solvation, which is derived from the observed onset of the cluster distributions at  $n = 5$ .

We have also carried out ab initio calculations for the dimer anion,  $(\text{Acn})_2^-$  employing the same level of theory. Fig. 5.4(b) depicts the optimized structure of  $(\text{Acn})_2^-$  and its singly-occupied molecular orbital (SOMO), which accommodates the excess electron. The most stable structure of the dimer anion is of  $C_{2h}$  symmetry, with its framework composed of two constituents having a pyramidal structure nearly identical with that of the monomer anion. As readily seen in Fig. 5.4(b), the SOMO is constructed by the in-phase superposition of two  $\pi_{\text{CO}}^*$  orbitals of the monomer, indicating that the excess electron is shared equally by the two constituents. The stabilization energy of the dimer anion is calculated to be 0.89 eV with reference to  $(\text{Acn})^- + \text{Acn}$ , and  $-0.72$  eV to  $(\text{Acn})_2 + e^-$  at the CCSD(T)/6-311+G\*\*//MP2/6-311+G\*\* level. The calculations also provide a VDE value of 0.44 eV for  $(\text{Acn})_2^-$ . Based on these results, we conclude that  $(\text{Acn})_2^-$  is stable against autodetachment, whereas it is slightly higher in energy than  $(\text{Acn})_2 + e^-$ .

As mentioned above, the VDE is determined experimentally to be  $0.83 \pm 0.03$  eV for  $(\text{Acn})_2^-$ . By considering that ab initio calculations often give a lower estimate for VDE than those determined experimentally,<sup>23</sup> it can be inferred that the calculated VDE value of 0.44 eV is in fair agreement with

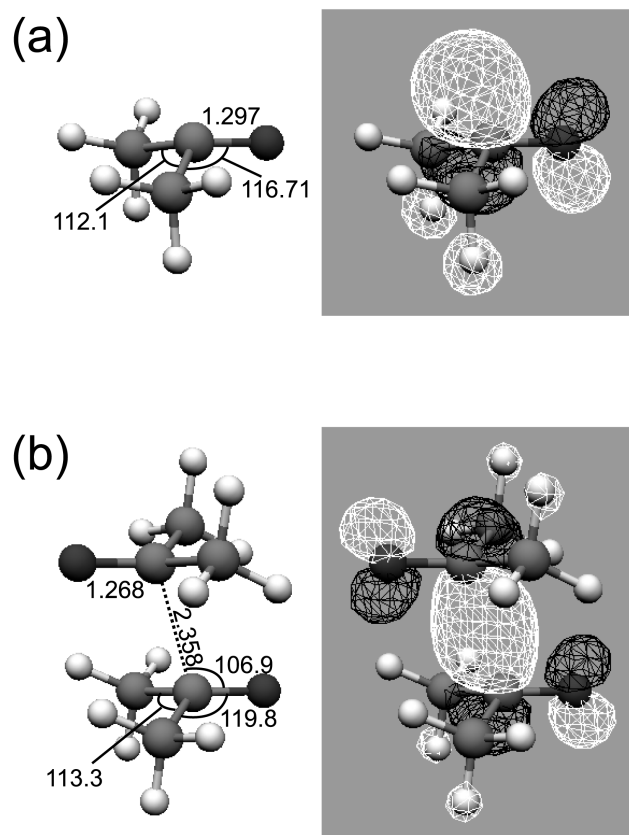


**Figure 5.4** Geometries of (a)  $(\text{Acn})^-$  and (b)  $(\text{Acn})_2^-$  optimized at the MP2/6-311+G\*\* level. Bond lengths and bond angles are given in Å and degrees. The profiles of the SOMOs are also shown on the right-hand side.

the experimental value. The energy calculations also suggest that the formation of  $(\text{Acn})_2^-$  is energetically rather unfavorable, which is consonant with the absence of  $n = 2$  in the  $(\text{Acn})_n^-$  spectrum. These arguments, in conjunction with the discussion in Sec. 5.3.3, lead us to conclude that the dimer anion, formed accidentally in our  $[(\text{Acn})_n(\text{H}_2\text{O})_m]^-$  beam, retains the structure shown in Fig. 5.4(b).

### 5.3.5 Qualitative evaluation of $\beta$ values

The observed PADs carry useful information on the symmetry properties of the SOMO. The averaged anisotropy parameter,  $\bar{\beta}$ , takes a negative value distinctively for  $n = 2$ , and slightly positive values for  $5 \leq n \leq 15$ . Recently, Sanov et al. proposed a qualitative approach for describing PADs in the photodetachment process of molecular anions and their clusters.<sup>24</sup> Their approach follows the



recipe developed by Reed et al. for dealing with the threshold photodetachment of molecular anions.<sup>25</sup> The electrons are ejected from SOMO upon photodetachment so as to satisfy the requirement,  $\langle \psi_e | \mu | \psi_{\text{SOMO}} \rangle \neq 0$ , where  $\psi_e$  and  $\psi_{\text{SOMO}}$  represent wave functions of the photoelectron and the pertinent SOMO, respectively, and  $\mu$  is the electric dipole moment of the system. The requirement for a nonzero transition moment tells us about the symmetry of  $\psi_e$ , which is then expanded in terms of single-center AO functions. When the expansion is subsequently restricted to partial waves with  $l \leq 1$ ,  $\psi_e$  can be approximated by s ( $l = 0$ ) and/or p ( $l = 1$ ) waves referred to the molecular frame (s&p model). By considering “principal” molecular orientations with respect to the laser polarization axis, qualitative information on PADs in the laboratory frame can be deduced from the symmetry properties of  $\psi_e$ .<sup>24</sup>

We have applied this s&p model to our system and found that the model predicts nonnegative  $\beta$  values ( $\beta \approx 0$  or  $\beta > 0$ ) for both the monomer and dimer anions, being in conflict with the experimental observation. This discrepancy arises primarily from the intrinsic weakness of the model in which only the s and p partial waves are included<sup>24</sup>; hence, it does not impair our primary conclusions that the formation of  $(\text{Acn})_2^-$  occurs with a specific anion structure shown in Fig. 5.4(b) and that the valence anion of acetone monomer serves as an ion core in the larger  $(\text{Acn})_n^-$  with  $5 \leq n \leq 15$ .

## References

- 1 Allan, J.T.; Scholes, G. *Nature* **1960**, *187*, 218–220.
- 2 Davies, A.G.; Neville, A.G. *J. Chem. Soc. Perkin Trans.* **1992**, *2* 163–169.
- 3 Köppe, R.; Kasai, P. H. *J. Phys. Chem.* **1994**, *98*, 12904–12910.
- 4 Fourré, I.; Silvi, B.; Chaquin, P.; Sevin, A. *J. Comp. Chem.* **1999**, *20*, 897–910.
- 5 Naff, W. T.; Compton, R. N.; Cooper, C. D. *J Chem Phys* **1972**, *57*, 1303–1307.
- 6 Desfrancois, C.; Abdoul-Carime, H.; Khelifa, N.; Schermann, J. P. *Phys. Rev. Lett.* **1994**, *73*, 2436.
- 7 Han, S. Y.; Kim, J. H.; Song, J. K.; Kim, S. K. *J Chem Phys* **1998**, *109*, 9656–9659.
- 8 Mitsui, M.; Ando, N.; Kokubo, S.; Nakajima, A.; Kaya, K. *Phys. Rev. Lett.* **2003**, *91*, 153002.
- 9 Maeyama, T.; Negishi, Y.; Tsukuda, T.; Yagi, I.; Mikami, N. *Phys. Chem. Chem. Phys.* **2006**, *8*, 827–833.
- 10 Johnson, M. A.; Lineberger, W. in: Farrar, J.M.; Saunders W.H. (Eds.), *Techniques in Chemistry*, Vol. 20, Wiley, New York, 1988, p. 591.
- 11 Eppink, A. T. J. B.; Parker, D. H. *Rev. Sci. Instrum.* **1997**, *68*, 3477–3484.
- 12 Dribinski, V.; Ossadtchi, A.; Mandelstam, V. A.; Reisler, H. *Rev. Sci. Instrum.* **2002**, *73*, 2634–2642.
- 13 Arnold, D.W.; Bradforth, S.E.; Kim, E.H.; Neumark, D.M. *J. Chem. Phys.* **1995**, *102* 3493–3509.
- 14 Balaj, O. P.; Siu, C.-K.; Balteanu, I.; Beyer, M. K.; Bondybey, V. E. *Int. J. Mass Spectrom.* **2004**, *238*, 65–74.
- 15 Surber, E.; Sanov, A. *J. Chem. Phys.* **2003**, *118*, 9192.
- 16 Reid, K. L. *Annu. Rev. Phys. Chem.* **2003**, *54*, 397–424.
- 17 Mabbs, R.; Surber, E.; Sanov, A. *J. Chem. Phys.* **2005**, *122*, 054308.
- 18 Cooper, J.; Zare, R.N. *J. Chem. Phys.* **1968**, *48*, 942–943.
- 19 Cooper, J.; Zare, R.N. *J. Chem. Phys.* **1968**, *49*, 4252.
- 20 O'Malley, T. F. *Phys. Rev.* **1965**, *137*, A1668.
- 21 Benitez, A.; Moore, J. H.; Tossell, J. A. *J. Chem. Phys.* **1988**, *88*, 6691–6698.
- 22 Sanche, L.; Schulz, G.J. *J. Chem. Phys.* **1973**, *58*, 479–493.
- 23 Saeki, M.; Tsukuda, T.; Iwata, S.; Nagata, T. *J. Chem. Phys.* **1999**, *111* 6333–6344.
- 24 Surber, E.; Mabbs, R.; Sanov, A. *J. Phys. Chem. A* **2003**, *107*, 8215–8224.
- 25 Reed, K. J.; Zimmerman, A. H.; Andersen, H. C.; Brauman, J. I. *J Chem Phys* **1976**, *64*, 1368–1375.

# Chapter 6

## Photodissociation of gas-phase $I_3^-$ : Comprehensive understanding of nonadiabatic dissociation dynamics

### ABSTRACT

Photodissociation of the gas-phase tri-iodide anion,  $I_3^-$ , was investigated using photofragment time of flight TOF mass spectrometry combined with the core extraction method. An analysis of the TOF profiles provided the kinetic energy and angular distributions of photofragment ions and photoneutrals, from which the photoproduct branching fractions were determined in the excitation energy range of 3.26–4.27 eV. The measurement has revealed that (1) in the entire energy range investigated, three-body dissociation occurs preferentially as the “charge-asymmetric” process  $\Gamma(^1S) + I(^2P_{3/2}) + I(^2P_{3/2})$  with the yield of 30%–40%, where the excess charge is localized on the end atoms of the dissociating  $I_3^-$ , and that (2) two-body dissociation via the  $^3\Pi_u(0_u^+) \leftarrow ^1\Sigma_g^+(0_g^+)$  excitation proceeds as  $\Gamma(^1S) + I_2(X^1\Sigma_g^+) / I_2(A^3\Pi_{1u})$  or  $I(^2P_{3/2}) + I_2^-(X^2\Sigma_u^+)$  with the yield of 60%, while that via the  $^1\Sigma_u^+(0_u^+) \leftarrow ^1\Sigma_g^+(0_g^+)$  excitation alternatively as  $I^*(^2P_{1/2}) + I_2^-(X^2\Sigma_u^+)$  or  $\Gamma(^1S) + I_2(B^3\Pi_u)$  with the yield of 60%. *Ab initio* calculations including spin-orbit configuration interactions were also performed to gain precise information on the potential energy surfaces relevant to the  $I_3^-$  photodissociation. The calculations have shown the presence of conical intersections and avoided crossings located along the symmetric stretch coordinate near the ground-state equilibrium geometry of  $I_3^-$ , which play key roles for the two-body and the three-body product branching. The nonadiabatic nature of the  $I_3^-$  photodissociation dynamics is discussed by combining the experimental findings and the *ab initio* results.

This chapter has been reproduced in part with permission from the following previously published article: Nakanishi, R.; Saitou, N.; Ohno, T.; Kowashi, S.; Yabushita, S.; Nagata, T. *Journal of Chemical Physics* 2007, 126, 204311. DOI: 10.1063/1.2736691 Copyright 2007 American Institute of Physics

\* *Only the abstract is provided in UTokyo Repository at the request of one of the coauthors.*  
(博士論文の共著者の意向により第 6 章は ABSTRACT 以外除外)

# Acknowledgments

I would like to express my foremost thanks to Prof. Takashi Nagata for his patience, support, and encouragement throughout my time in his group. Without his guidance and tutorage, the work presented in this dissertation could not have been accomplished.

My gratitude also goes to all the members that I have worked with in the Nagata group. I enjoyed every moment I spent with them and appreciate their assistance. Especially, I want to thank Prof. Yoshiya Inokuchi and Dr. Azusa Muraoka for their stimulating discussions.

Some part of the theoretical work in this dissertation was aided by collaborators from other research group. I am indebted to Prof. Kazuo Takatsuka for allowing us to use his high performance computer facilities for ab initio calculations of acetone cluster anions. Prof. Takeshi Sato and Prof. Kiyoshi Yagi are acknowledged for calculations on the complex anions of water cluster with a benzene molecule. I must also thank Prof. Satoshi Yabushita for calculations of potential energy surfaces of tri-iodide anion and valuable discussions on its photodissociation dynamics.

I would also like to thank Prof. Tatsuya Tsukuda and Prof. Fumitaka Mafuné for their generous and continuous encouragement.

And last, but certainly not least, I am very grateful to my family for their constant support throughout the years.

Ryuzo Nakanishi